NASA TECHNICAL NOTE

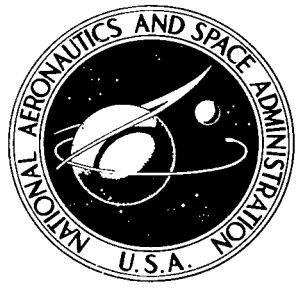

NASA TN D-6440

DYNAMIC STABILITY DERIVATIVES OF A JET TRANSPORT CONFIGURATION WITH HIGH THRUST-WEIGHT RATIO AND AN EXTERNALLY BLOWN JET FLAP

by Sue B. Grafton, Lysle P. Parlett, and Charles C. Smith, Jr.

Langley Research Center
Hampton, Va. 23365

NATIONAL AERONAUTICS AND SPACE ADMINISTRATION • WASHINGTON, D. C. • SEPTEMBER 1971

1. Report No.	2. Government Accession No.	3. Recipient's Catalog No.
NASA TN D-6440		

4. Title and Subtitle
DYNAMIC STABILITY DERIVATIVES OF A JET TRANSPORT CONFIGURATION WITH HIGH THRUST-WEIGHT RATIO AND AN EXTERNALLY BLOWN JET FLAP

5. Report Date
September 1971

6. Performing Organization Code

7. Author(s)
Sue B. Grafton, Lysle P. Parlett, and Charles C. Smith, Jr.

8. Performing Organization Report No.
L-7870

10. Work Unit No.
760-72-01-02

9. Performing Organization Name and Address
NASA Langley Research Center
Hampton, Va. 23365

11. Contract or Grant No.

13. Type of Report and Period Covered
Technical Note

12. Sponsoring Agency Name and Address
National Aeronautics and Space Administration
Washington, D.C. 20546

14. Sponsoring Agency Code

15. Supplementary Notes

16. Abstract

The investigation was conducted to determine the dynamic stability derivatives of an externally blown jet-flap transport configuration having clustered inboard pod-mounted engines and full-span triple-slotted flaps. The results showed that the model had positive damping in pitch, roll, and yaw up to the stall angle of attack. The application of power resulted in an increase in pitch damping at high angles of attack and a moderate increase in yaw damping for the higher flap deflections but had no consistent effects on roll damping. For a given level of total engine thrust, the damping derivatives were generally not affected by frequency or by having one engine inoperative.

17. Key Words (Suggested by Author(s))	18. Distribution Statement
Dynamic stability Jet flap High thrust-weight ratio	Unclassified – Unlimited

19. Security Classif. (of this report)	20. Security Classif. (of this page)	21. No. of Pages	22. Price*
Unclassified	Unclassified	81	$3.00

*For sale by the National Technical Information Service, Springfield, Virginia 22151

DYNAMIC STABILITY DERIVATIVES OF A JET TRANSPORT CONFIGURATION WITH HIGH THRUST-WEIGHT RATIO AND AN EXTERNALLY BLOWN JET FLAP

By Sue B. Grafton, Lysle P. Parlett, and Charles C. Smith, Jr.
Langley Research Center

SUMMARY

A wind-tunnel investigation was conducted in the Langley full-scale tunnel to determine the dynamic stability derivatives of an externally blown jet-flap transport configuration having clustered inboard pod-mounted engines and full-span triple-slotted flaps. The investigation was made at a Reynolds number of 0.35×10^6 based on the mean aerodynamic chord of the model. The results showed that the model had positive damping in pitch, roll, and yaw up to the stall angle of attack. The application of power resulted in an increase in pitch damping at high angles of attack mainly because the tail damping was higher. Power also caused moderate increases in yaw damping for the higher flap deflections, but the effects on roll damping were inconsistent. The effects of frequency on the damping derivatives were generally relatively small. For a given level of total engine thrust, the damping derivatives were not appreciably affected by having one engine inoperative.

INTRODUCTION

The present investigation was conducted to provide some fundamental information on the dynamic stability derivatives of a jet transport configuration with high thrust-weight ratio and an externally blown jet flap. Previous static stability and performance studies (refs. 1 and 2) have shown that the application of this concept to high-thrust-weight-ratio turbofan aircraft was effective for producing the high lift required for short take-off and landing operation. Research was continued with full-span triple-slotted flaps, leading-edge boundary-layer control, and clustered engine arrangement as a means of improving the aerodynamic efficiency of such a configuration. (See ref. 3.) Because of the promising results achieved in the static stability and performance studies, a program has been initiated to evaluate the dynamic stability, flight characteristics, handling qualities, and general piloting techniques of this configuration. The research is to be conducted with a fixed-base simulator requiring aerodynamic inputs in the form of static

and dynamic stability derivatives. As part of the overall program, the present investigation was undertaken to measure the dynamic stability derivatives of the jet transport configuration with a high thrust-weight ratio and an externally blown jet flap. Results of a similar investigation for a lower range of thrust-weight ratios are presented in reference 4.

The model used in the investigation was powered by four simulated high-bypass-ratio turbofan engines mounted in a clustered arrangement relatively close inboard and was equipped with full-span triple-slotted trailing-edge flaps and a fixed leading-edge flap. The model was also equipped with a leading-edge blowing system for use in some tests. The dynamic stability derivatives were determined in pitching, rolling, and yawing forced-oscillation tests at different frequencies, thrust conditions, and flap deflection angles for an angle-of-attack range from -5° to 35°. Additional tests were made to determine the dynamic stability for the model with the vertical tail off and for the model with various engine-out conditions. In order to aid in the interpretation of the dynamic force test data, the static longitudinal and lateral stability characteristics of the model were also determined and are presented.

SYMBOLS

The dynamic longitudinal and lateral-directional data and the static lateral data are referred to the body-axis system; the static longitudinal data are referred to the stability-axis system. (See fig. 1.) The origin of the axes was located to correspond to the center-of-gravity position (0.40 mean aerodynamic chord) shown in figure 2(a).

Measurements and calculations were made in the U.S. Customary Units. They are presented herein in the International System of Units (SI) with the equivalent values in the U.S. Customary Units given parenthetically. Factors relating the two systems are given in reference 5.

b wing span, meters (feet)

C_D drag coefficient, $\frac{F_D}{q_\infty S}$

C_L lift coefficient, $\frac{F_L}{q_\infty S}$

$C_{l_\beta} = \frac{\partial C_l}{\partial \beta}$, per degree or per radian

C_m pitching-moment coefficient, $\frac{M_Y}{q_\infty S \bar{c}}$

$C_{n_\beta} = \frac{\partial C_n}{\partial \beta}$, per degree or per radian

$C_{Y_\beta} = \frac{\partial C_Y}{\partial \beta}$, per degree or per radian

C_μ engine gross-thrust coefficient, $T/q_\infty S$

$C_{\mu,le}$ wing-semispan leading-edge blowing jet momentum coefficient, $R/q_\infty S$

c local chord, meters (feet)

$\bar{c}$ mean aerodynamic chord, meters (feet)

F_A axial force, newtons (pounds)

F_D drag force, newtons (pounds)

F_L lift force, newtons (pounds)

F_N normal force, newtons (pounds)

F_X force along X-axis, newtons (pounds)

F_Y force along Y-axis, newtons (pounds)

f frequency of oscillation, hertz (cycles per second)

i_t horizontal-tail incidence angle, degrees

k reduced-frequency parameter, $\omega b/2V$ or $\omega \bar{c}/2V$

M_X rolling moment, meter-newtons (foot-pounds)

M_Y pitching moment, meter-newtons (foot-pounds)

M_Z yawing moment, meter-newtons (foot-pounds)

p rolling angular velocity, radians/second

q pitching angular velocity, radians/second

q_∞	free-stream dynamic pressure, $\rho V^2/2$, newtons/meter^2 (pounds/foot^2)
R	resultant force, newtons (pounds)
r	yawing angular velocity, radians/second
S	wing surface area, meters^2 (feet^2)
T	total installed engine thrust, newtons (pounds)
V	free-stream velocity, meters/second (feet/second)
X, Y, Z	body reference axes
X_S, Y_S, Z_S	stability reference axes
x,y	flap coordinates, meters (feet)
α	angle of attack, degrees or radians
$\dot{\alpha}$	rate of change of angle of attack, radians/second
β	angle of sideslip, degrees or radians
$\dot{\beta}$	rate of change of angle of sideslip, radians/second
δ_e	elevator deflection angle, positive when trailing edge is down, degrees
δ_f	deflection of rear element of trailing-edge flap (same as δ_{f3} in fig. 2(b)), positive when trailing edge is down, degrees
$\delta_{f,le}$	leading-edge flap deflection, positive when leading edge is down, degrees
ρ	air density, kilograms/meter^3 (slugs/foot^3)
ϕ	angle of roll, degrees or radians
ω	angular velocity, $2\pi f$, radians/second

$$C_N = \frac{F_N}{q_\infty S} \qquad C_A = \frac{F_A}{q_\infty S} \qquad C_Y = \frac{F_Y}{q_\infty S}$$

$$C_{N_q} = \frac{\partial C_N}{\partial \frac{q\bar{c}}{2V}} \qquad C_{A_q} = \frac{\partial C_A}{\partial \frac{q\bar{c}}{2V}} \qquad C_{m_q} = \frac{\partial C_m}{\partial \frac{q\bar{c}}{2V}}$$

$$C_{N_{\dot{\alpha}}} = \frac{\partial C_N}{\partial \frac{\dot{\alpha}\bar{c}}{2V}} \qquad C_{A_{\dot{\alpha}}} = \frac{\partial C_A}{\partial \frac{\dot{\alpha}\bar{c}}{2V}} \qquad C_{m_{\dot{\alpha}}} = \frac{\partial C_m}{\partial \frac{\dot{\alpha}\bar{c}}{2V}}$$

$$C_l = \frac{M_X}{q_\infty Sb} \qquad C_n = \frac{M_Z}{q_\infty Sb}$$

$$C_{l_p} = \frac{\partial C_l}{\partial \frac{pb}{2V}} \qquad C_{n_p} = \frac{\partial C_n}{\partial \frac{pb}{2V}} \qquad C_{Y_p} = \frac{\partial C_Y}{\partial \frac{pb}{2V}}$$

$$C_{l_r} = \frac{\partial C_l}{\partial \frac{rb}{2V}} \qquad C_{n_r} = \frac{\partial C_n}{\partial \frac{rb}{2V}} \qquad C_{Y_r} = \frac{\partial C_Y}{\partial \frac{rb}{2V}}$$

$$C_{l_{\dot{\beta}}} = \frac{\partial C_l}{\partial \frac{\dot{\beta}b}{2V}} \qquad C_{n_{\dot{\beta}}} = \frac{\partial C_n}{\partial \frac{\dot{\beta}b}{2V}} \qquad C_{Y_{\dot{\beta}}} = \frac{\partial C_Y}{\partial \frac{\dot{\beta}b}{2V}}$$

Subscripts:

L	left wing
R	right wing

APPARATUS AND MODEL

The tests were made in the 9.1- by 18.3-meter (30- by 60-ft) open-throat test section of the Langley full-scale tunnel with the model mounted about 3.05 meters (10 ft) above the ground board. The model was so small in proportion to the tunnel test section that no wind-tunnel corrections were needed.

The investigation was conducted on the four-engine, high-wing jet-transport model illustrated by the three-view drawing of figure 2(a). Dimensional characteristics of the model are given in table I. The wing had a leading-edge sweep angle of 28.3° and incorporated the leading-edge flaps and triple-slotted trailing-edge flaps shown in figures 2(b) and 2(c). Coordinates for the three elements of the trailing-edge flaps are given in table II. The full-span trailing-edge flaps were divided into three spanwise segments on each wing semispan as indicated in figure 2(a). All three trailing-edge segments were deflected as a unit (a full-semispan flap), except where otherwise specified.

The leading edge of the wing was also equipped with a blowing system for boundary-layer control (fig. 2(d)). Compressed air forced through a tube inserted in the wing leading edge exhausted through many small holes into the leading-edge plenum chamber and from there through the leading-edge slot.

To facilitate model configuration changes and to insure accurate flap deflection angles, the wing of the model was designed with removable trailing edges. Such removable trailing edges were provided for the clean (flaps up) configuration and for several different flap-deflected configurations with fixed gaps, overlaps, and deflection angles. Figure 2(b) shows the principal flap systems used: one, designated the "take-off flap," had deflections of $17^{\circ}/0.5^{\circ}/35^{\circ}$ and the others, designated the "landing flaps," had deflections of $25^{\circ}/10^{\circ}/50^{\circ}$ or $25^{\circ}/10^{\circ}/70^{\circ}$. In addition, the landing flaps were constructed so that the rear flap element could be deflected differentially and locked into position for lateral trim in the engine-out tests. In the remainder of the text and in all the data figures, only the deflection of the rear flap element is used for identification purposes.

The model engines (pod mounted) represented high-bypass-ratio turbofans and were installed at -3° incidence (with reference to X-axis) so that the jet exhaust impinged directly on the trailing-edge flap system. The engine turbines were driven by compressed air and turned fans which produced the desired thrust. This model is described in detail in reference 3.

A photograph of the model mounted for dynamic forced-oscillation tests in the full-scale tunnel is presented in figure 3. All the static and dynamic force tests were made with a single strut or sting-support system and with an internal strain-gage balance. Sketches of the forced-oscillation test equipment are presented in figure 4, and the equipment is described in reference 6.

TESTS AND PROCEDURES

In preparation for the tests, the gross thrust of each engine was measured as a function of engine rotational speed in the static condition. The tests were then performed by setting the engine rotational speed to give the desired thrust and holding this speed constant through the range of angle of attack. The jet momentum of the leading-edge boundary-layer control system was evaluated by measuring the force produced by the jets in the wind-off condition.

Dynamic force tests were made to determine the longitudinal and lateral-directional oscillatory stability derivatives of all model configurations with power off and with power on for values of C_{μ} of 1.74 and 3.48. These force tests were made over an angle-of-attack range from -5° to 35° for $\delta_f = 35^{\circ}$, 50°, and 70°. A few tests were also made with the clean configuration. The longitudinal stability derivatives were measured for an

amplitude of $\pm 5.75^{\circ}$ and the lateral-directional stability derivatives, for an amplitude of $\pm 5.00^{\circ}$. All derivatives were measured for frequencies of 0.5 or 1.0 hertz (cps) corresponding to values of reduced-frequency parameter k of 0.0367 and 0.0734, respectively, for the pitching test and of 0.2442 and 0.4884, respectively, for both the rolling and yawing tests. The tail incidence angle was set at 0° and the elevator deflection angles was set at -50° for all the tail-on tests, with the exception of those with the clean configuration. Additional dynamic force tests were made for the model with $C_{\mu,le} = 0.024$ and for the model with the vertical tail removed. In order to aid in interpretation of the dynamic data, static force tests were also conducted to obtain the static longitudinal and lateral-directional stability characteristics of the model.

The investigation was conducted at a dynamic pressure of 144 newtons/meter^2 (3.0 lb/ft^2) which corresponds to a Reynolds number of 0.35×10^6 based on the mean aerodynamic chord of the model.

RESULTS AND DISCUSSION

Aerodynamic Characteristics

Longitudinal.- The static longitudinal aerodynamic characteristics of the model are presented in figures 5 and 6. In general, these data show that the stall angle of attack and the maximum lift coefficient increased with an increase in gross-thrust coefficient and that the effects of power were more pronounced at the higher flap deflections. A maximum lift coefficient of almost 9.0 (untrimmed) was achieved with a flap deflection of 70° and a thrust coefficient of 3.48. The addition of the horizontal tail generally resulted in static longitudinal stability up to the stall angle of attack for all thrust conditions. Additional static longitudinal data and a more detailed discussion of the static longitudinal stability characteristics of the subject configuration are presented in reference 3.

Lateral-directional.- The static lateral-directional stability derivatives are presented in figures 7 and 8. These data show that for all tail-on configurations the model had positive directional stability $\left(+C_{n_\beta}\right)$ and positive effective dihedral $\left(-C_{l_\beta}\right)$ up to the stall angle of attack. The directional stability is virtually unaffected by change in angle of attack; effective dihedral, however, increased with an increase in angle of attack up to the stall. For all tail-on configurations, the application of thrust resulted in notable increases in directional stability throughout the test angle-of-attack range. At angles of attack near the power-off stall angle, thrust also produced increments of effective dihedral (fig. 8). Additional static lateral-directional stability data for the subject configuration are presented in reference 3.

Dynamic Stability Derivatives

Pitching.- The variations of the oscillatory pitching derivatives with angle of attack are presented in figures 9 to 15. The data for the clean configuration (fig. 9) show that the model had very small values of pitch damping with the tail off and that the addition of the tail resulted in relatively large values of pitch damping that remained essentially constant with angle of attack. The data of figures 10 to 14 show that the pitch damping for the flap-down configuration was much higher than that for the clean configuration, mainly because the tail damping was much higher. As the angle of attack was increased, however, the tail damping contribution decreased and, in the power-off condition, resulted in the model becoming undamped in some configurations. The addition of power is seen to minimize or eliminate the loss in tail damping as angle of attack increases; thus, the power-on model had relatively high values of pitch damping over the test angle-of-attack range.

A comparison of the data of figures 11(a) and 11(b), 12(a) and 12(b), and 14(a) and 14(b) shows that changes in oscillation frequency between 0.5 and 1.0 hertz (cps) had no appreciable effect on the pitch damping derivatives in the normal operating angle-of-attack range. Also, a comparison of data of figures 11(a) and 11(c), 12(a) and 12(c), and 14(a) and 14(c) indicates that leading-edge blowing $\left(C_{\mu,le}\right)$ had relatively little effect on the oscillatory pitching derivatives. Comparison of the engine-out data, presented in figure 15, with the data for symmetrical engine operation shows that the oscillatory pitching derivatives were not significantly affected when either the left inboard or left outboard engine was not operating or when the rear elements of the trailing-edge flaps were deflected differentially to provide roll trim for the engine-out configuration.

Rolling.- The variations of the oscillatory rolling derivatives with angle of attack are presented in figures 16 to 21. These data show that the model had positive damping in roll $-\left(C_{l_p} + C_{l_{\dot{\beta}}} \sin \alpha\right)$ for all angles of attack below the stall angle. The damping in roll decreased as the model approached the stall angle of attack and the model became undamped at angles of attack above the stall for some of the flap-deflected configurations with power. The dynamic rolling derivatives show no consistent changes with respect to an increase in power or flap deflection angle. The clean configuration (fig. 16) had only about one-half the damping in roll at the lower angles of attack as the flap-deflected configurations. (This result was expected since the damping in roll is dependent upon the lift-curve slope and a comparison of the data of figures 5 and 6 reveals that the lift-curve slope of the clean configuration was only about one-half that for the flap-down configuration. The lift-curve slopes, for the power-off configurations, increase with an increase in flap deflection because of an enlargement of effective wing area – that is, as the trailing-edge flaps are deflected downward, they move rearward. Wing area is further increased by extending the leading-edge flap.) The addition of the tail or the variation

of frequency generally had only a relatively small effect on the roll damping for any of the configurations tested; this indicated that no unusual sidewash effects were present. A comparison of the data of figures 19(a) and 19(b) and 20(a) and 20(b) shows that the rolling oscillatory derivatives were not changed significantly by leading-edge blowing for boundary-layer control. Also, the data of figures 20 and 21 indicate that the derivatives were not appreciably affected by the left inboard or left outboard engine not operating or by differential deflection of the trailing-edge flaps for roll trim for the engine-out configuration.

Yawing.- The variations of the oscillatory yawing derivatives with angle of attack are presented in figures 22 to 28. The data show that the model with tail off had relatively small values of yaw damping except when $\delta_f = 70^o$. The addition of the vertical tail provided a relatively large increment of yaw damping that resulted in the model having positive damping in yaw $-\left(C_{n_r} - C_{n_{\dot{\beta}}} \cos \alpha\right)$ over the test angle-of-attack range. The value of yaw damping remained essentially constant with angle of attack and was generally unaffected by changes in power and frequency except for the 70^o flap-down configuration for which increases in power produced some increase in yaw damping. The derivatives for rolling moment due to yawing generally were unaffected by changes in power and frequency. A comparison of the data of figures 23(a) and 23(b) and 27(a) and 27(c) indicates that leading-edge blowing had a relatively small effect on the yaw damping derivatives. Also, comparison of the engine-out data presented in figure 28 with symmetrical power conditions of figure 27 shows that the oscillatory yawing derivatives were relatively unaffected by either the left inboard or left outboard engine not operating or by differential deflection of the trailing-edge flaps for roll trim for the engine-out configuration.

SUMMARY OF RESULTS

The results of an investigation to determine the dynamic stability derivatives of an externally-blown jet-flap jet transport configuration may be summarized as follows:

1. The model had positive damping in pitch, roll, and yaw up to the stall angle of attack.

2. The addition of power in the externally blown jet-flap system resulted in appreciable increases in pitch damping at high angles of attack, mainly because the tail damping was higher. Power caused moderate increases in yaw damping for the higher flap deflections but had no consistent effects on roll damping.

3. The effects of frequency on the damping derivatives were generally relatively small for all model configurations.

4. The damping derivatives were not appreciably affected by having one engine inoperative for a given level of total engine thrust.

Langley Research Center,
National Aeronautics and Space Administration,
Hampton, Va., July 26, 1971.

REFERENCES

1. Parlett, Lysle P.; Freeman, Delma C., Jr.; and Smith, Charles C., Jr.: Wind-Tunnel Investigation of a Jet Transport Airplane Configuration With High Thrust-Weight Ratio and an External-Flow Jet Flap. NASA TN D-6058, 1970.

2. Freeman, Delma C., Jr.; Parlett, Lysle P.; and Henderson, Robert L.: Wind-Tunnel Investigation of a Jet Transport Airplane Configuration With an External-Flow Jet Flap and Inboard Pod-Mounted Engines. NASA TN D-7004, 1970.

3. Parlett, Lysle P.; Greer, H. Douglas; Henderson, Robert L.; and Carter, C. Robert: Wind-Tunnel Investigation of an External-Flow Jet-Flap Transport Configuration Having Full-Span Triple-Slotted Flaps. NASA TN D-6391, 1971.

4. Freeman, Delma C., Jr.; Grafton, Sue B.; and D'Amato, Richard: Static and Dynamic Stability Derivatives of a Model of a Jet Transport Equipped With External-Flow Jet-Augmented Flaps. NASA TN D-5408, 1969.

5. Mechtly, E. A.: The International System of Units – Physical Constants and Conversion Factors (Revised). NASA SP-7012, 1969.

6. Chambers, Joseph R.; and Grafton, Sue B.: Static and Dynamic Longitudinal Stability Derivatives of a Powered 1/9-Scale Model of a Tilt-Wing V/STOL Transport. NASA TN D-3591, 1966.

TABLE I.- DIMENSIONS OF MODEL

Wing:	
Area, m^2 (ft^2)	0.783 (8.43)
Span (to theoretical tip), cm (in.)	238.02 (93.71)
Aspect ratio	7.23
Mean aerodynamic chord, cm (in.)	35.79 (14.09)
Location of quarter-chord of mean aerodynamic chord, referenced to nose of model, cm (in.)	103.53 (40.76)
Spanwise station of mean aerodynamic chord, cm (in.)	50.32 (19.81)
Root chord, cm (in.)	49.50 (19.49)
Tip chord (theoretical tip), cm (in.)	16.62 (6.54)
Sweep of quarter-chord line, deg	27.50
Dihedral of quarter-chord line, deg	-3.50
Incidence of mean aerodynamic chord, deg	4.50
Incidence of root chord, deg	6.00
Geometric twist:	
Root, deg	0.0
Tip, deg	-3.5
Vertical tail:	
Area, m^2 (ft^2)	0.155 (1.67)
Span, cm (in.)	50.80 (20.00)
Aspect ratio	1.66
Sweep angles:	
Leading edge, deg	38
Trailing edge, deg	31
Root chord, cm (in.)	35.56 (14.00)
Tip chord, cm (in.)	25.78 (10.15)
Horizontal tail:	
Area, m^2 (ft^2)	0.268 (2.88)
Span, cm (in.)	118.77 (46.76)
Mean aerodynamic chord, cm (in.)	24.18 (9.52)
Incidence	Variable
Dihedral, deg	-5.0
Engines:	
Spanwise location of inboard engines, cm (in.)	26.59 (10.47)
Spanwise location of outboard engines, cm (in.)	36.75 (14.47)
Incidence of all engine center lines relative to X-axis, deg	-3.00
Moment reference:	
Longitudinal location, referenced to nose of model, cm (in.)	108.81 (42.84)
Vertical location, referenced to top of fuselage at wing, cm (in.)	12.49 (4.92)
Control-surface dimensions:	
Rudder:	
Span, cm (in.)	40.6 (16.0)
Chord, upper end, parallel to X-axis, cm (in.)	10.92 (4.30)
Chord, lower end, perpendicular to hinge line, cm (in.)	15.2 (6.0)
Hinge-line location, percent chord	57
Sweep of hinge line, deg	34
Elevator:	
Span, cm (in.)	43.99 (17.31)
Chord, outboard, cm (in.)	4.21 (1.66)
Chord, inboard, cm (in.)	8.40 (3.31)
Hinge-line location, percent chord	73
Sweep of hinge line, deg	16.5

TABLE II.- FLAP COORDINATES

[Percent of local wing chord]

First element

x	y_{upper}	y_{lower}
0.00	1.67	1.67
1.39	4.33	.11
2.78	5.67	.00
4.17	6.44	↓
5.56	6.83	
6.44	6.83	
8.33	6.67	
9.72	6.28	
11.11	5.94	
12.50	5.56	
13.61	5.11	
15.28	4.61	1.50
16.67	4.06	2.39
18.06	3.61	3.00
19.17	3.22	3.17

Second element

x	y_{upper}	y_{lower}
0.00	0.94	0.94
.94	2.39	.11
1.78	2.67	.00
2.78	2.94	.17
3.72	3.06	.39
4.61	2.94	.56
5.56	2.83	.72
6.50	2.61	.94
7.06	2.39	.94
7.39	2.22	.94
8.33	1.78	.72
9.28	1.27	.56
10.17	.72	.28
11.00	.11	.00

Third element

x	y_{upper}	y_{lower}
0.00	0.72	0.72
.72	2.50	.11
1.83	3.17	.06
2.78	3.44	.00
3.72	3.50	↓
4.44	3.50	
5.56	3.50	
7.39	3.33	
9.28	3.06	
11.11	2.78	.06
12.94	2.39	.11
14.83	2.11	.17
16.67	1.83	.17
18.50	1.56	.17
20.39	1.22	.17
22.22	.83	.11
24.06	.56	.06
24.94	.28	.00

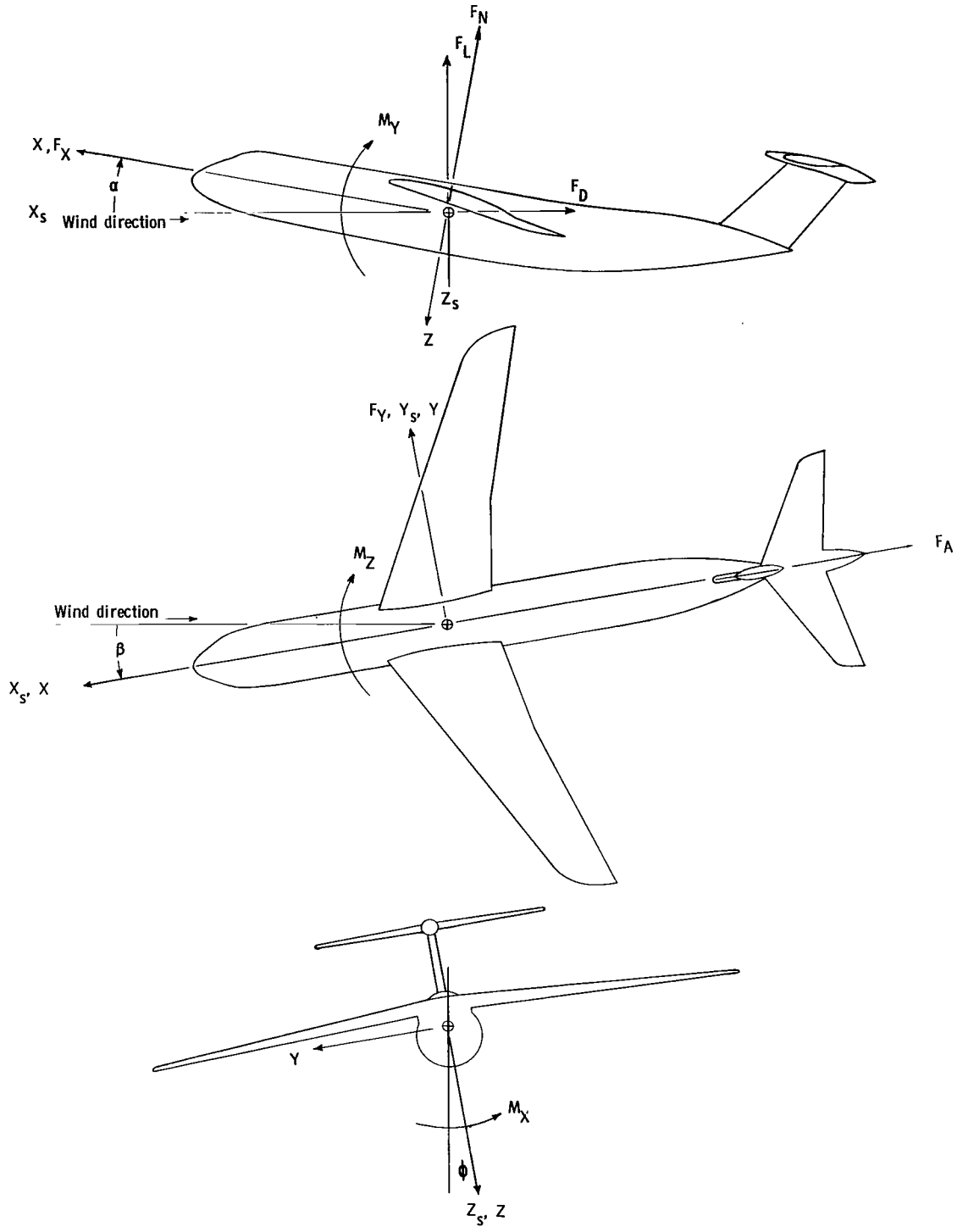

Figure 1.- Axis systems used in presentation of data. Arrows indicate positive direction of moments, axes, forces, and angles.

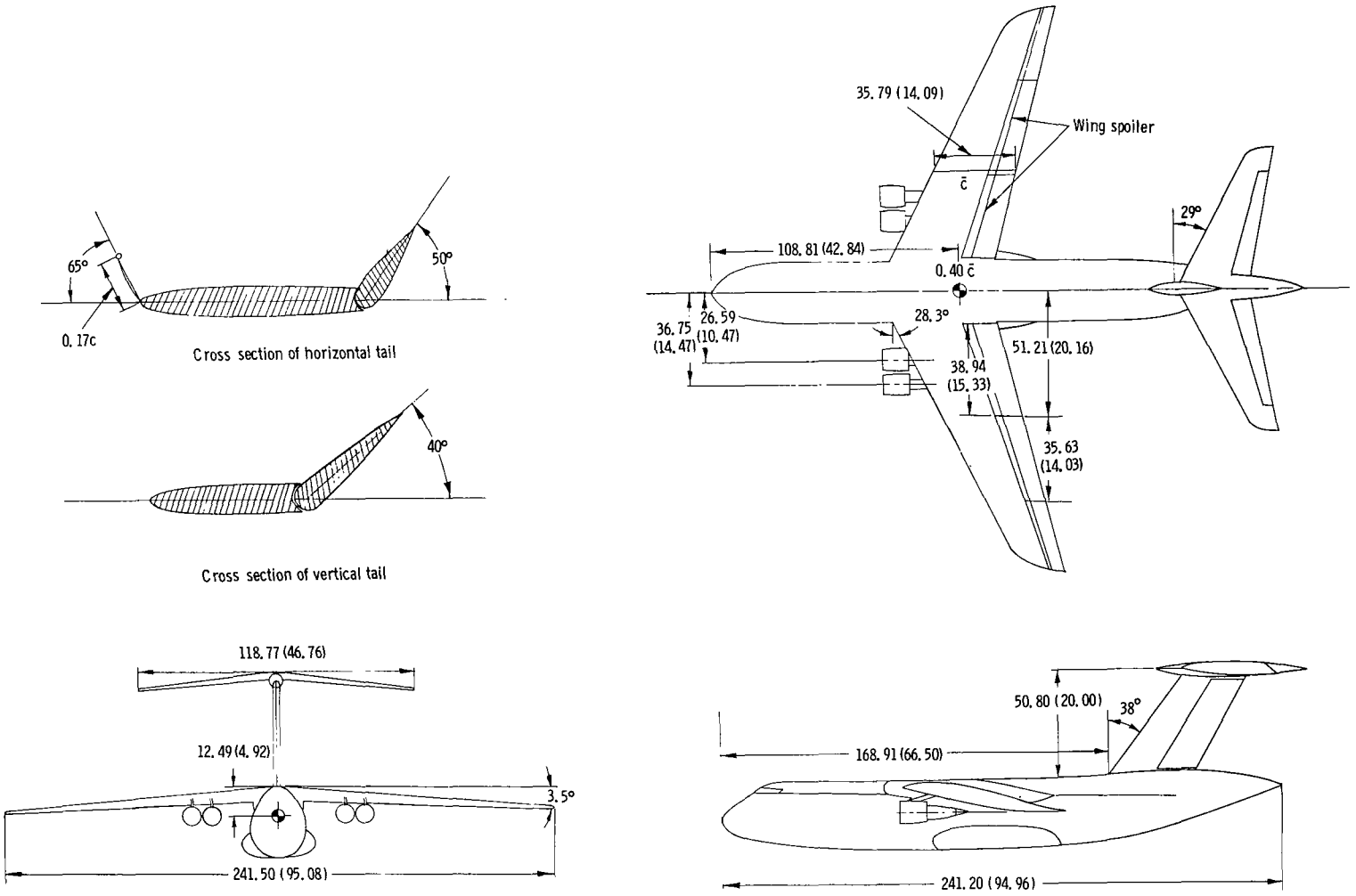

(a) Three-view drawing of complete model.

Figure 2.- Model used in investigation. All linear dimensions are in centimeters (inches).

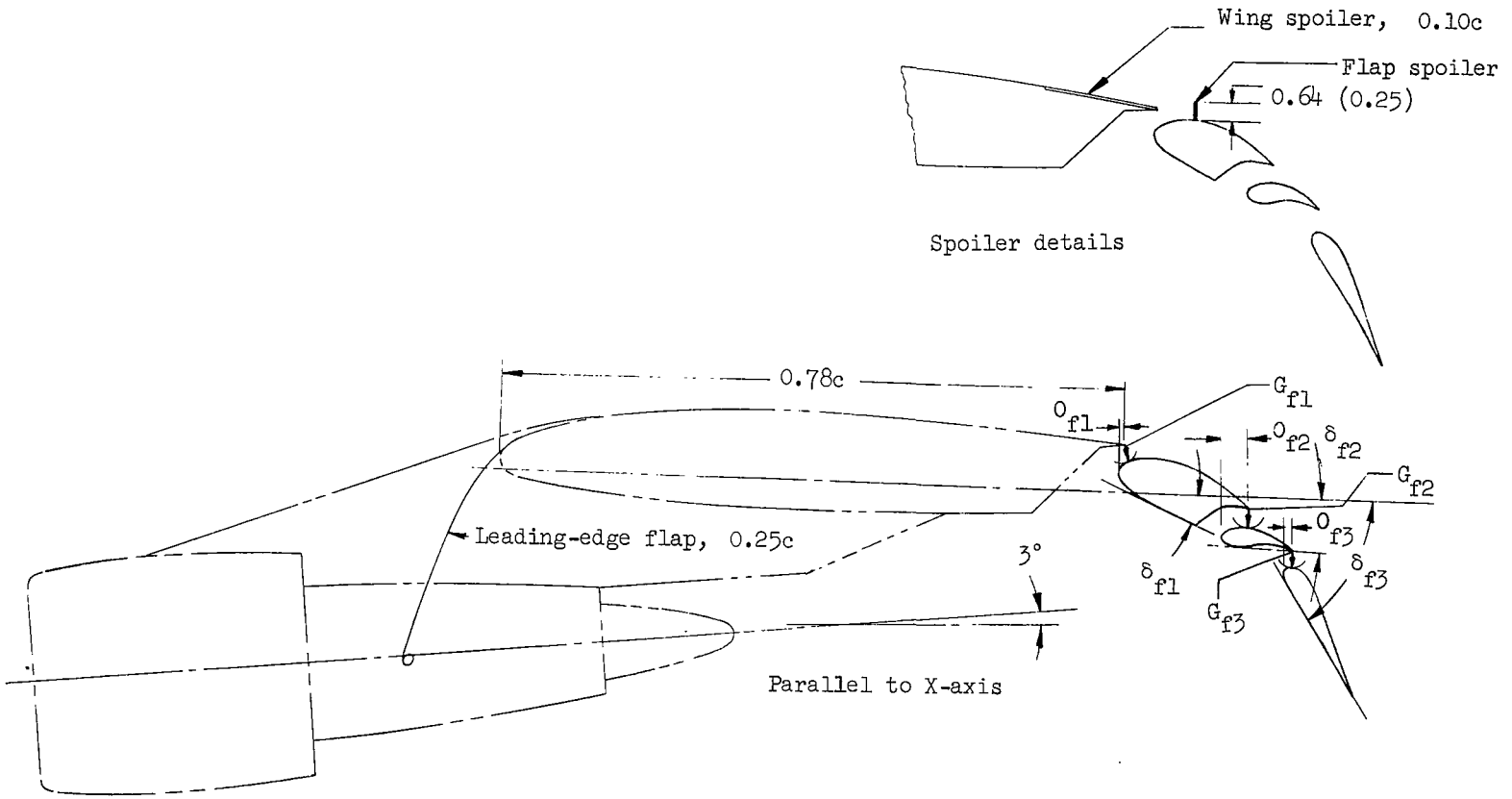

	δ_{f1}, deg	δ_{f2}, deg	δ_{f3}, deg	Flap element 1 overlap, O_{f1}, percent c	Flap element 1 gap, G_{f1}, percent c	Flap element 2 overlap, O_{f2}, percent c	Flap element 2 gap, G_{f2}, percent c	Flap element 3 overlap, O_{f3}, percent c	Flap element 3 gap, G_{f3}, percent c
Takeoff	17	0.5	35	1.47	1.61	3.15	1.61	1.52	1.61
Landing	25	10.0	50	1.47	1.61	3.98	1.61	1.39	1.61
Landing	25	10.0	70	1.47	1.61	3.98	1.61	1.39	1.61

(b) Details of flap assembly and engine-pylon. See table II for flap coordinates in terms of local wing chord.

Figure 2.- Continued.

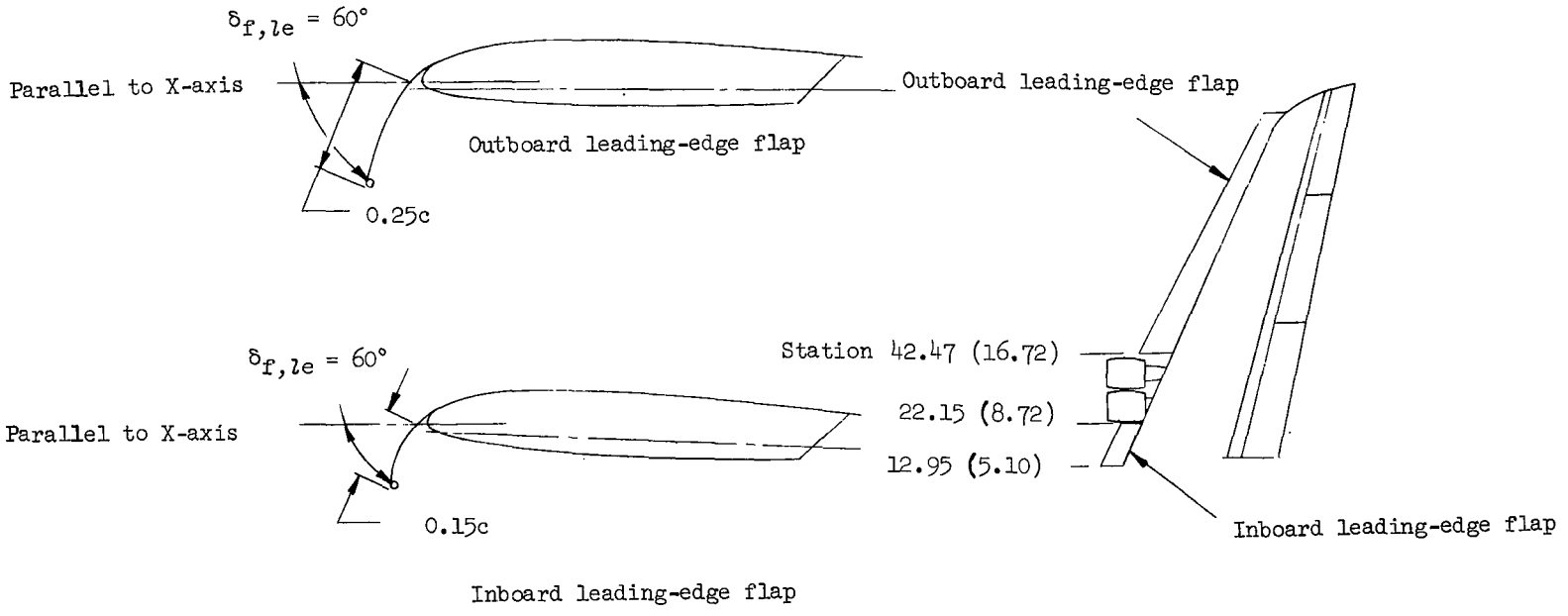

(c) Details of leading-edge flap.

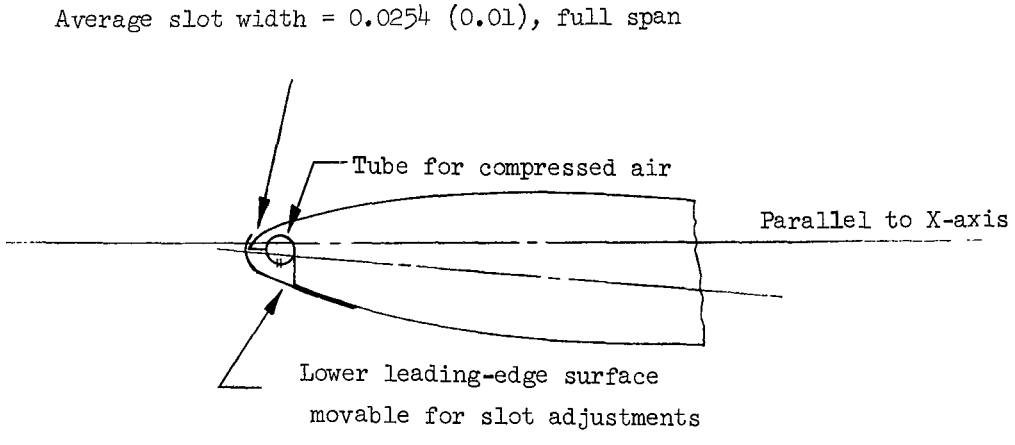

(d) Leading-edge boundary-layer control system used in some tests.

Figure 2.- Concluded.

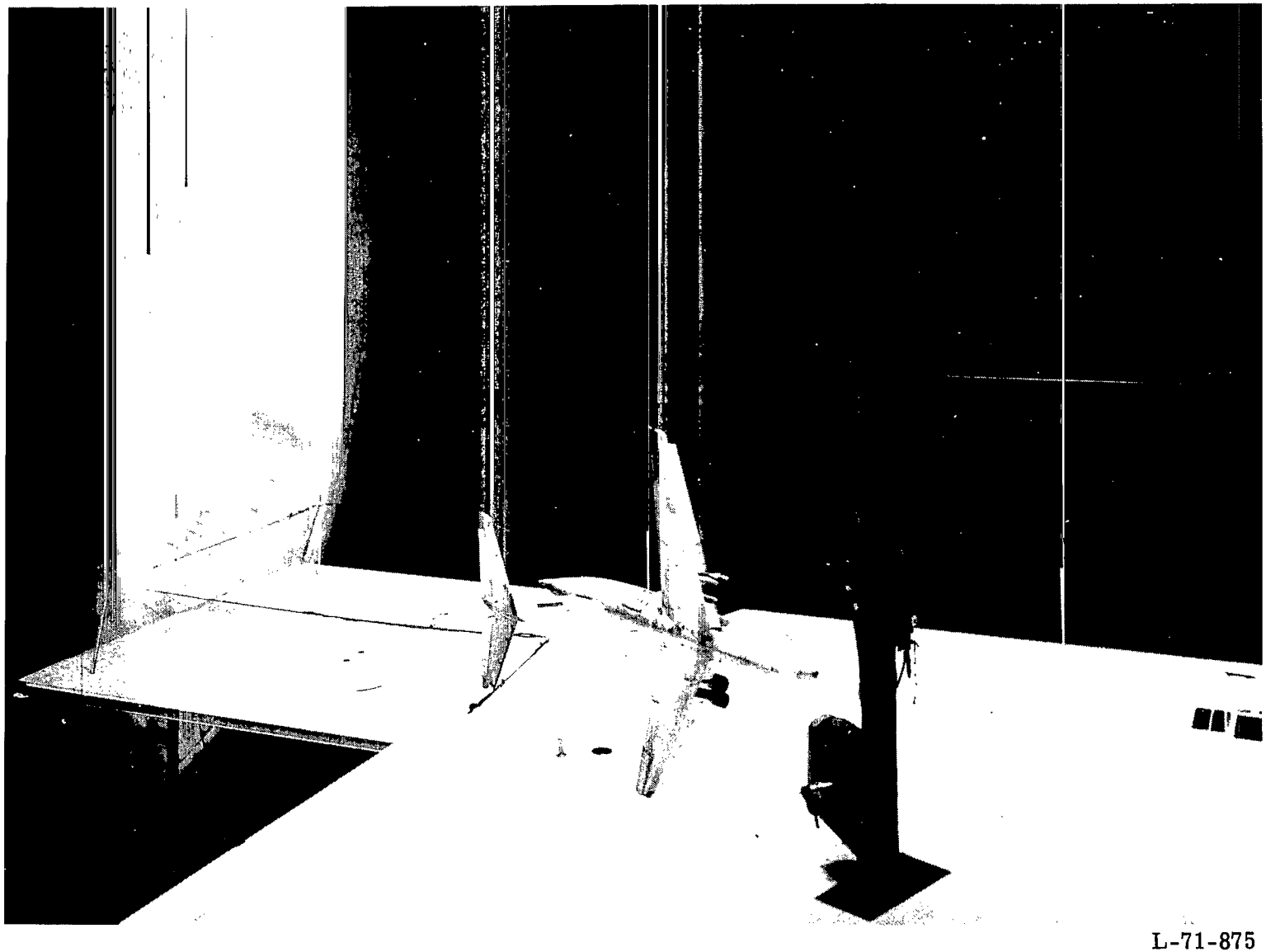

L-71-875

Figure 3.- Model mounted for dynamic force tests in the Langley full-scale tunnel.

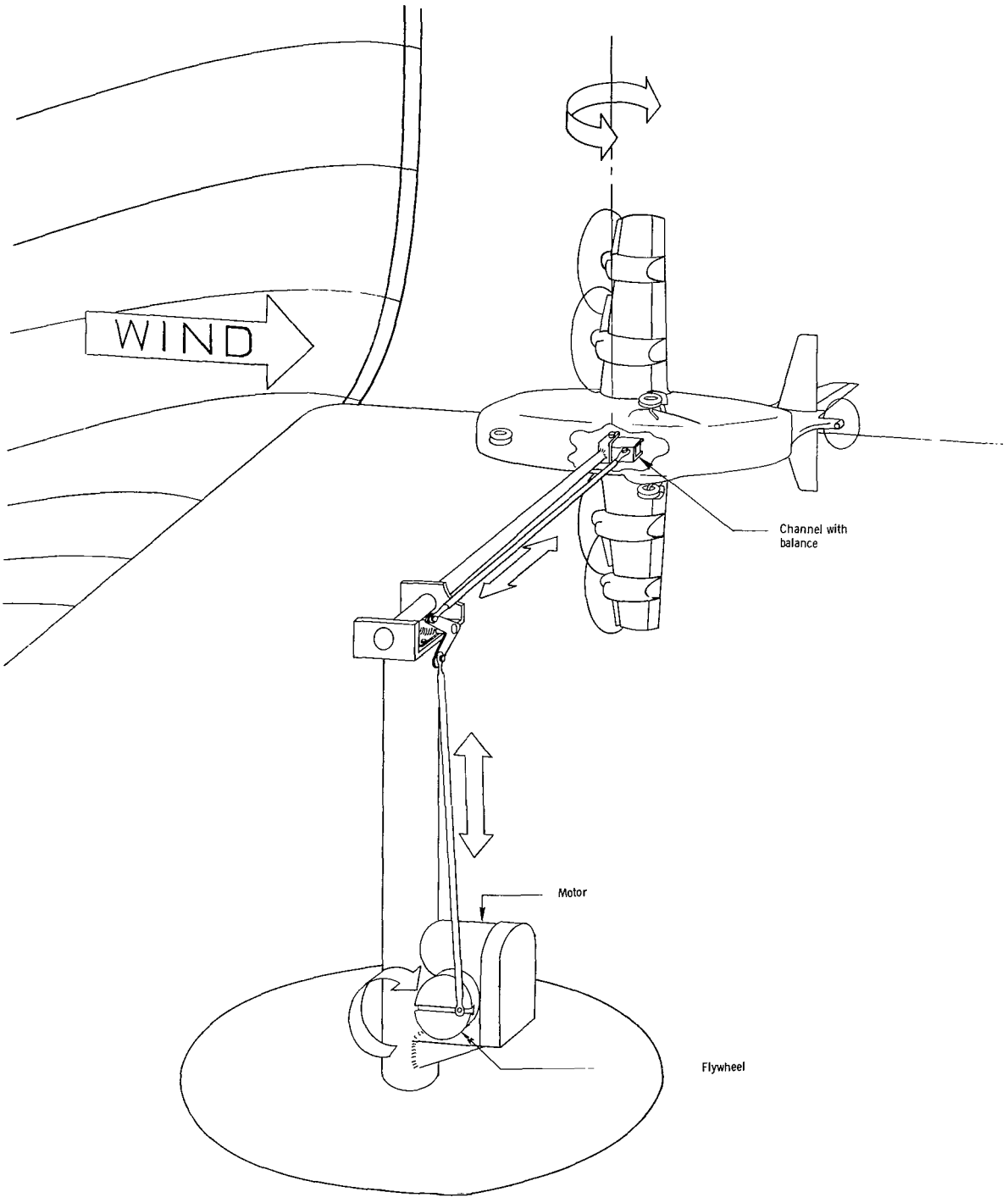

(a) Pitching setup.

Figure 4.- Sketches of forced-oscillation test setups.

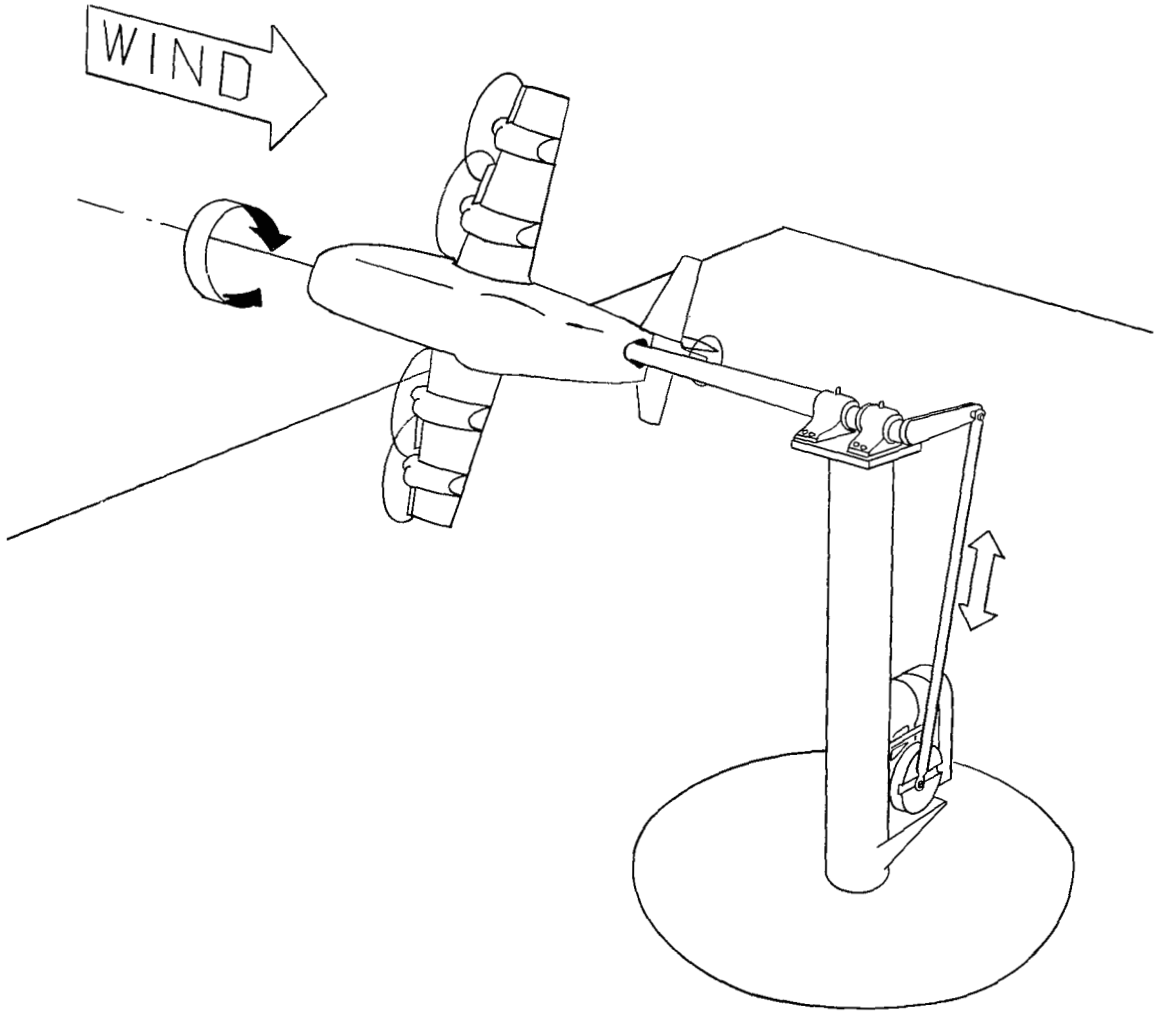

(b) Rolling setup.

Figure 4.- Continued.

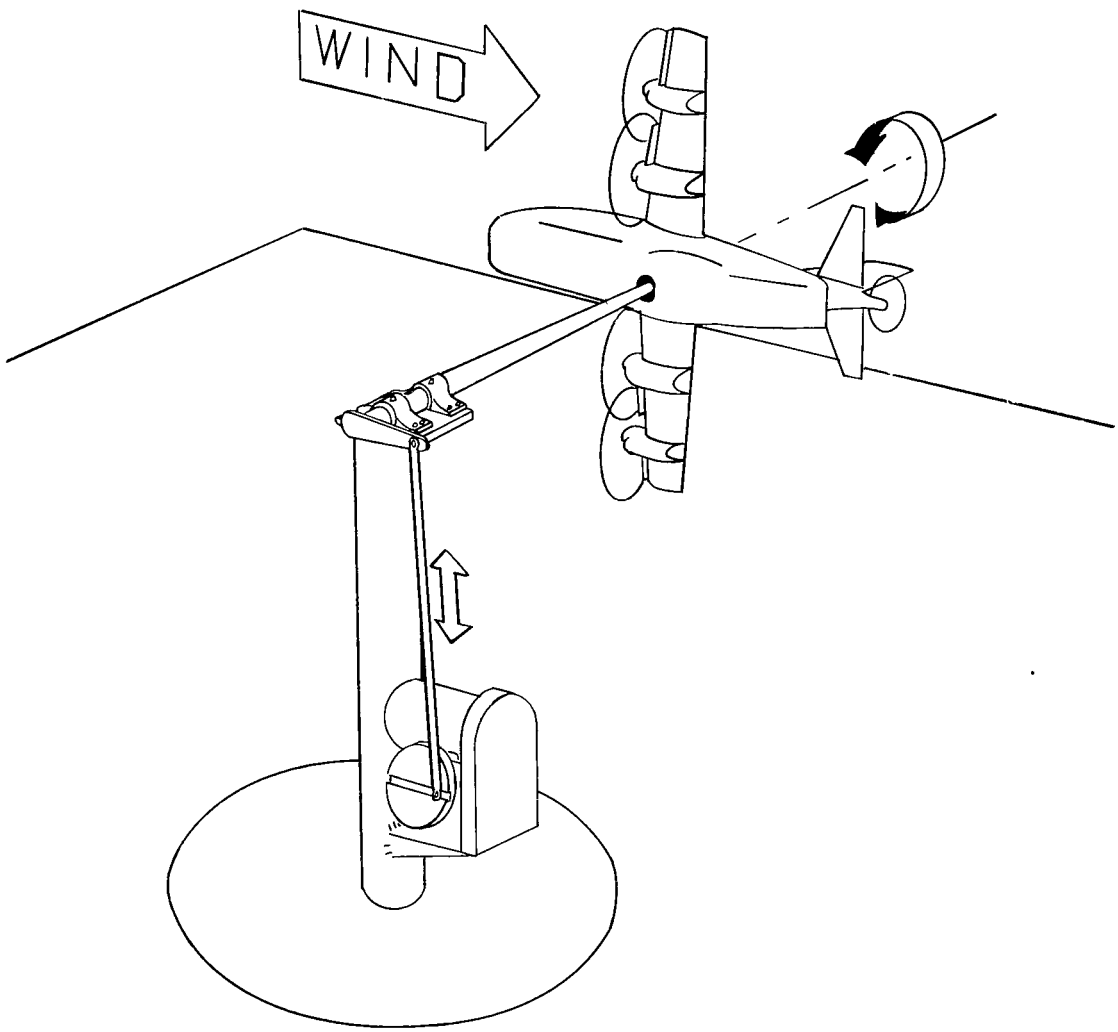

(c) Yawing setup.

Figure 4.- Concluded.

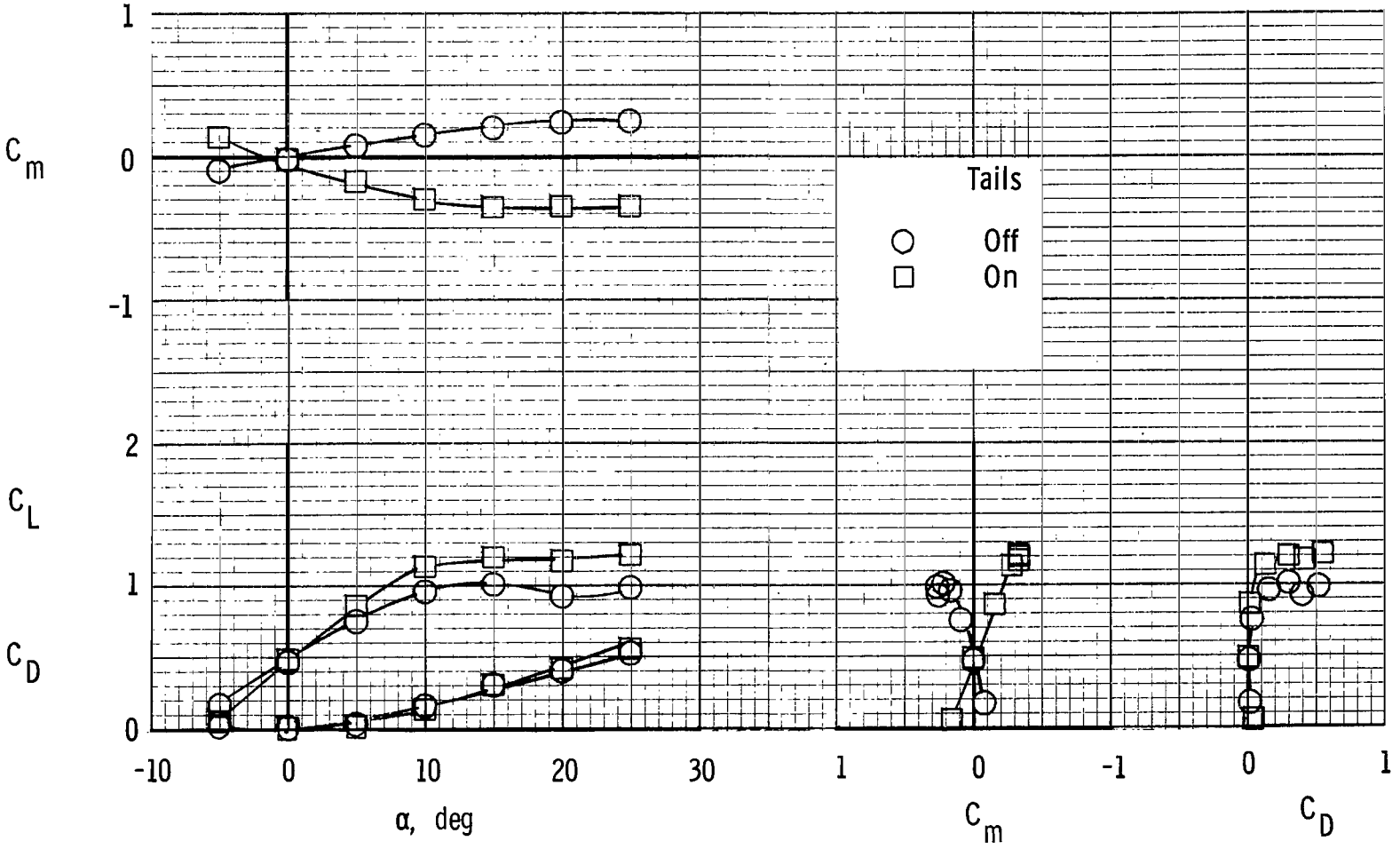

Figure 5.- Static longitudinal aerodynamic characteristics of the clean configuration.
$\delta_f = 0^o$; $i_t = 0^o$; $\delta_e = 0^o$; $C_\mu = 0$.

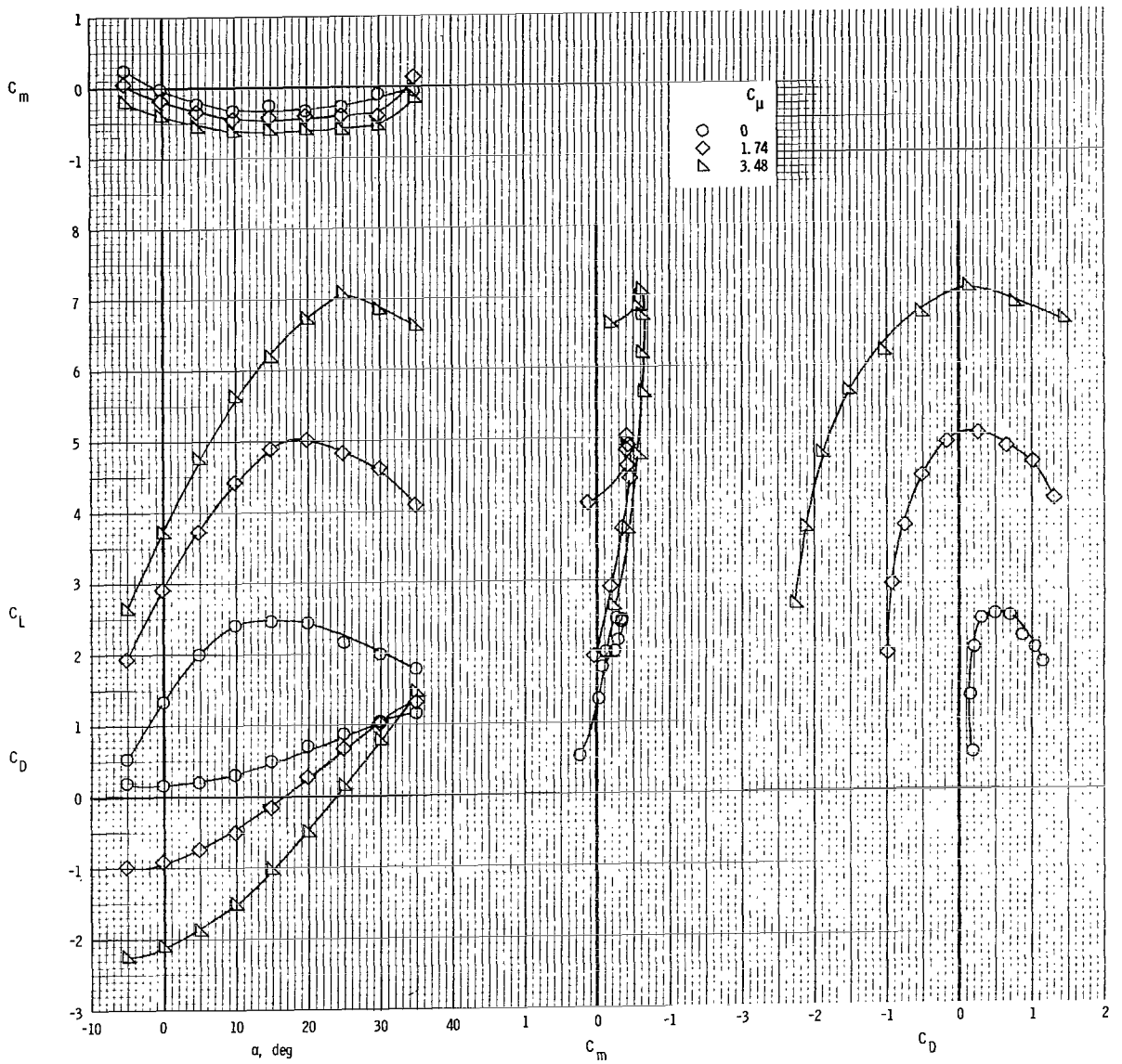

(a) $\delta_f = 35^o$; tails on; $i_t = 0^o$; $\delta_e = -50^o$.

Figure 6.- Static longitudinal aerodynamic characteristics of model for various engine gross-thrust coefficients. $C_{\mu,le} = 0$.

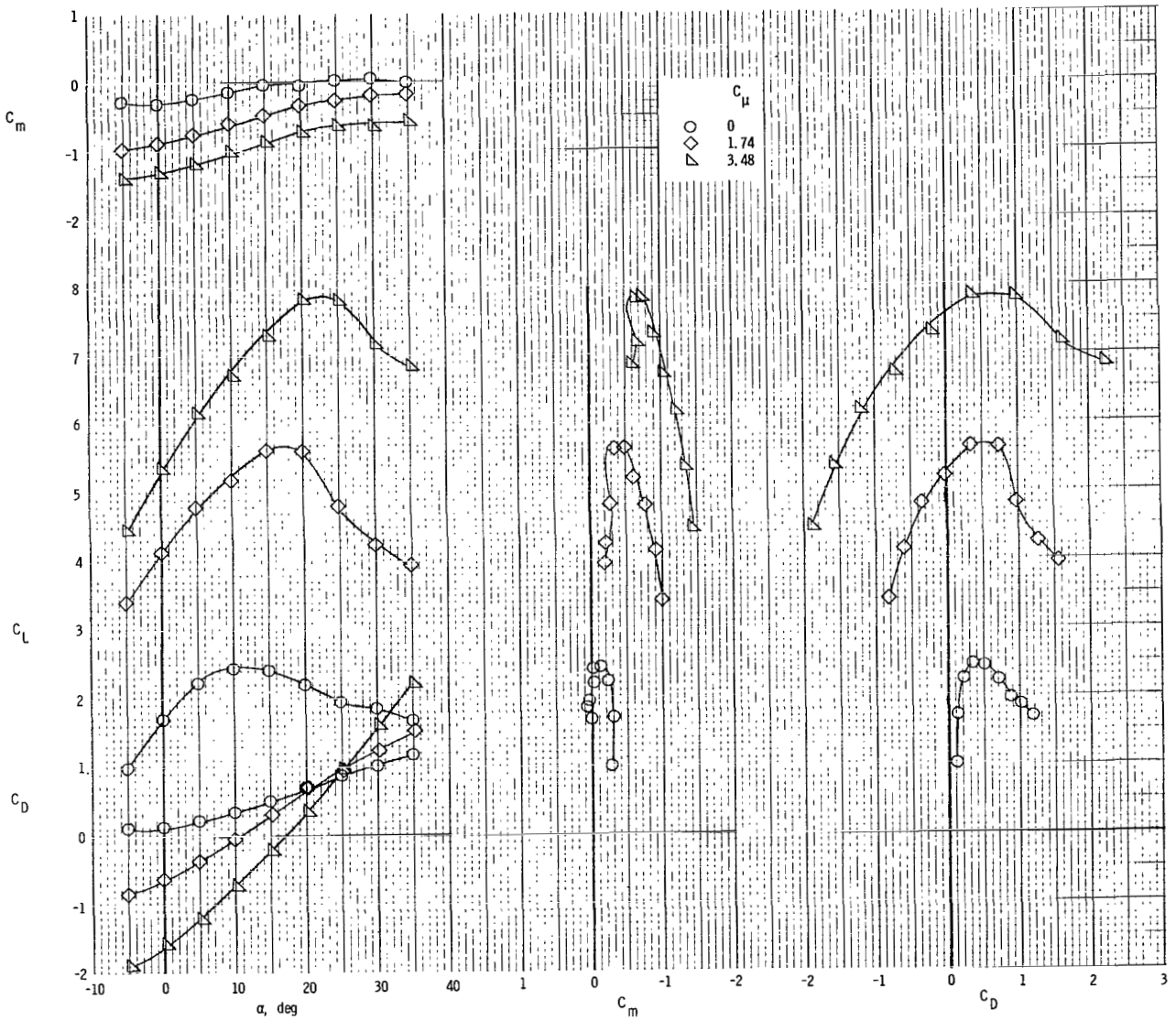

(b) $\delta_f = 50^o$; tails off.

Figure 6.- Continued.

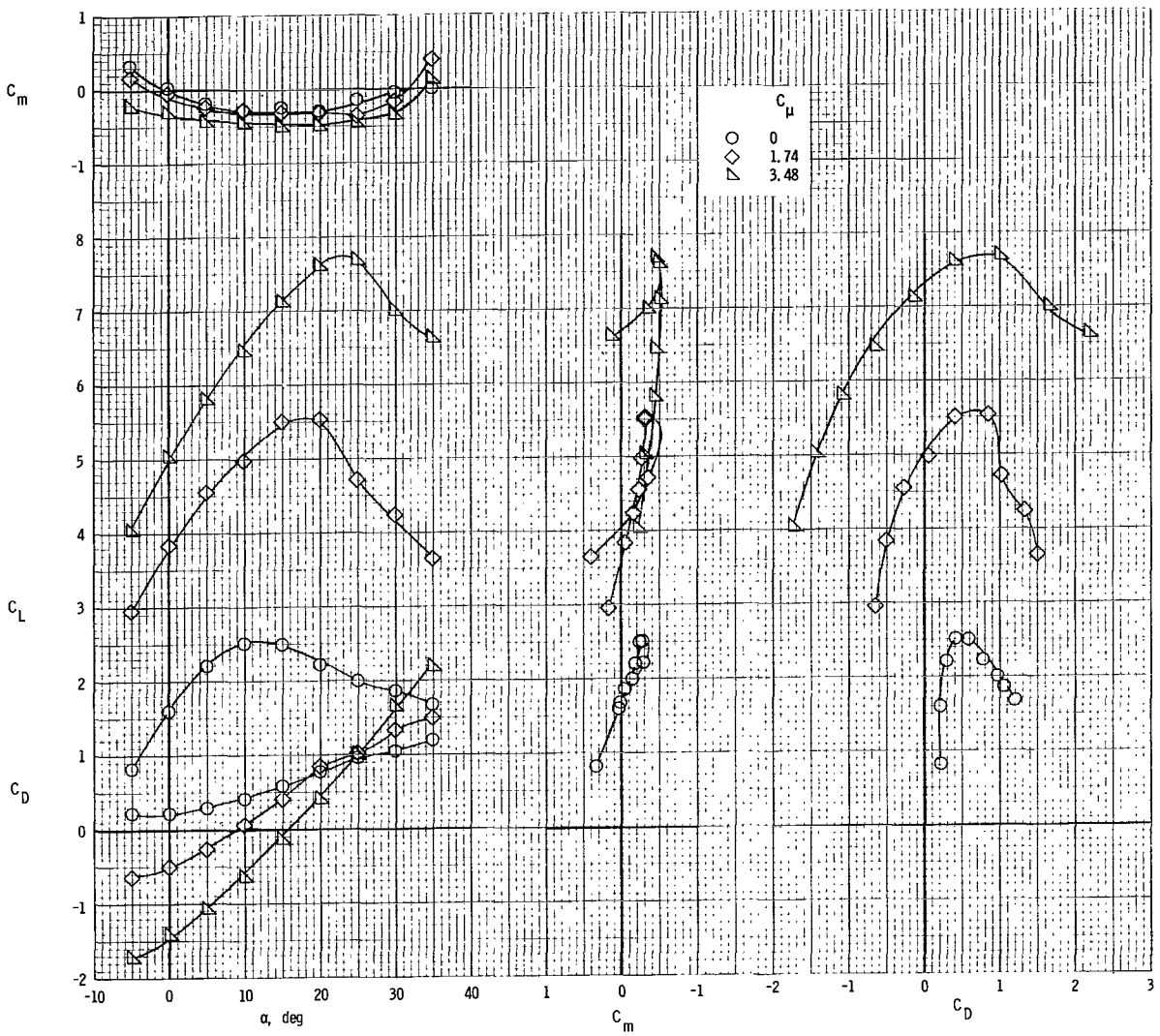

(c) $\delta_f = 50^o$; tails on; $i_t = 0^o$; $\delta_e = -50^o$.

Figure 6.- Continued.

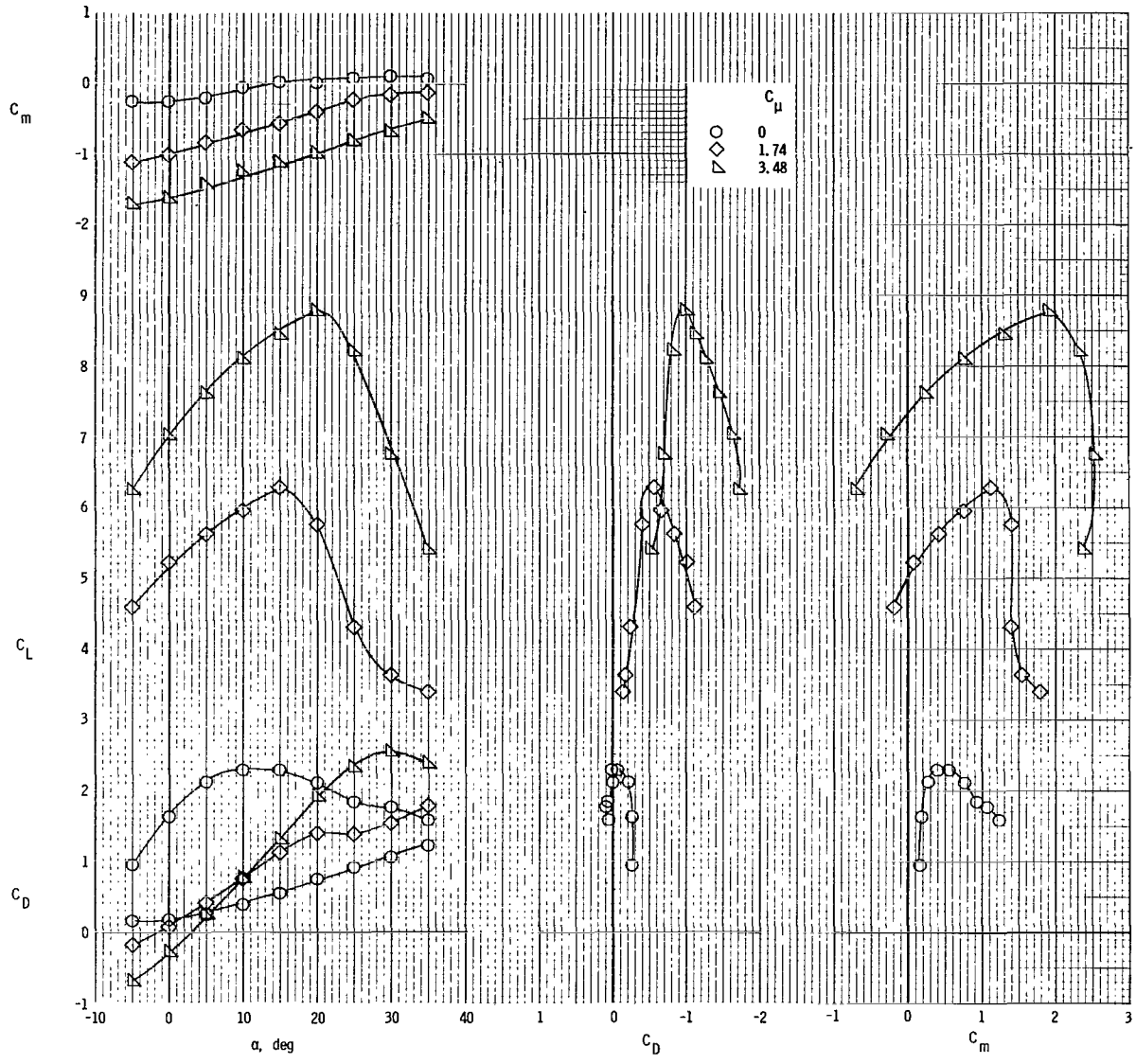

(d) $\delta_f = 70^o$; tails off.

Figure 6.- Continued.

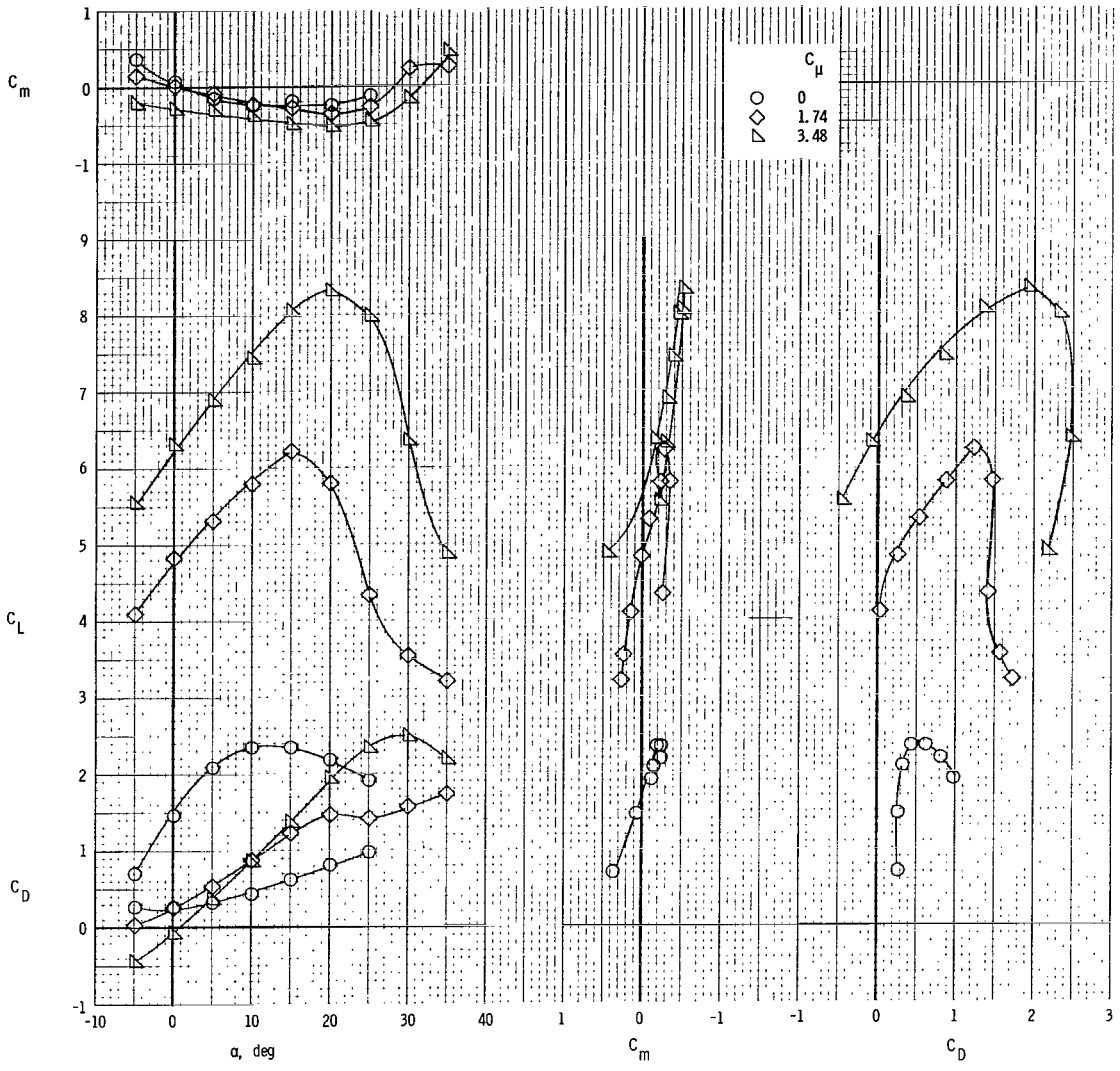

(e) $\delta_f = 70^o$; tails on; $i_t = 0^o$; $\delta_e = -50^o$.

Figure 6.- Concluded.

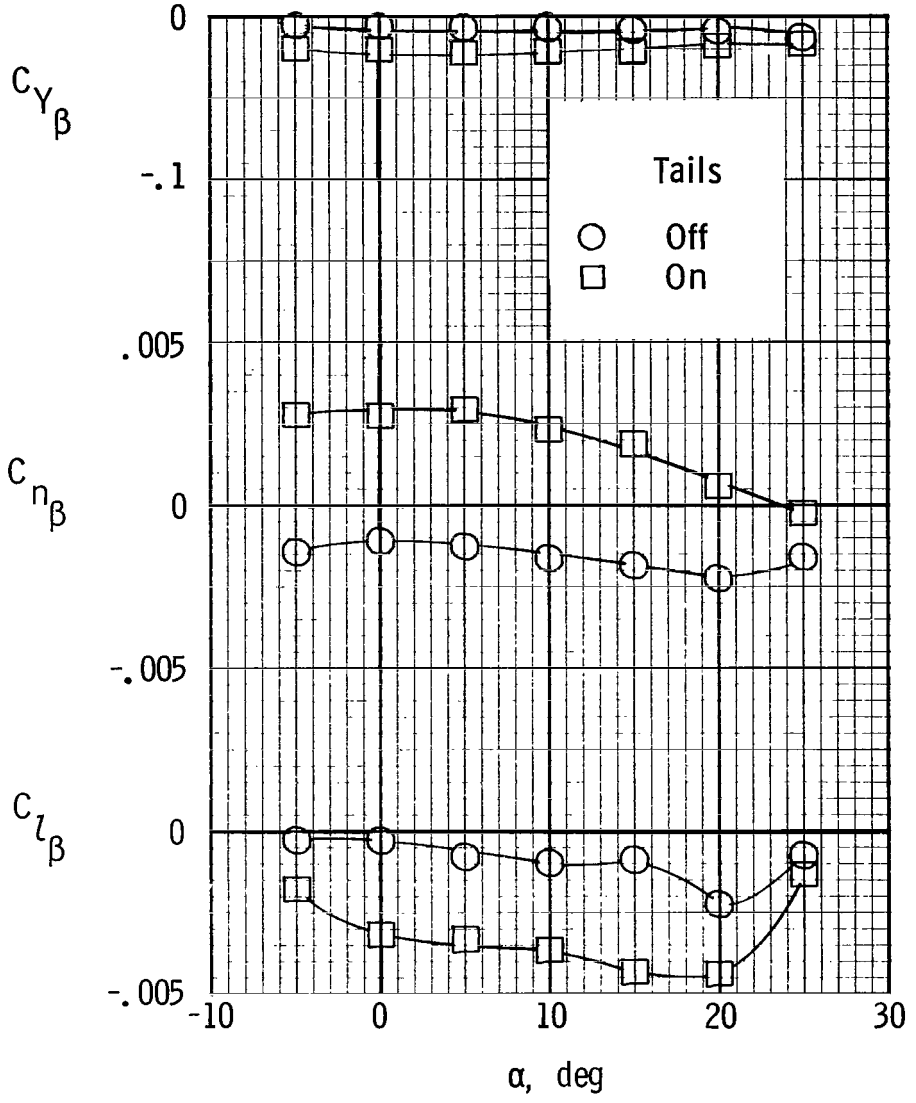

Figure 7.- Static lateral-directional stability derivatives of the clean configuration. $\delta_f = 0^o$; $i_t = 0^o$; $\delta_e = 0^o$; $C_\mu = 0$.

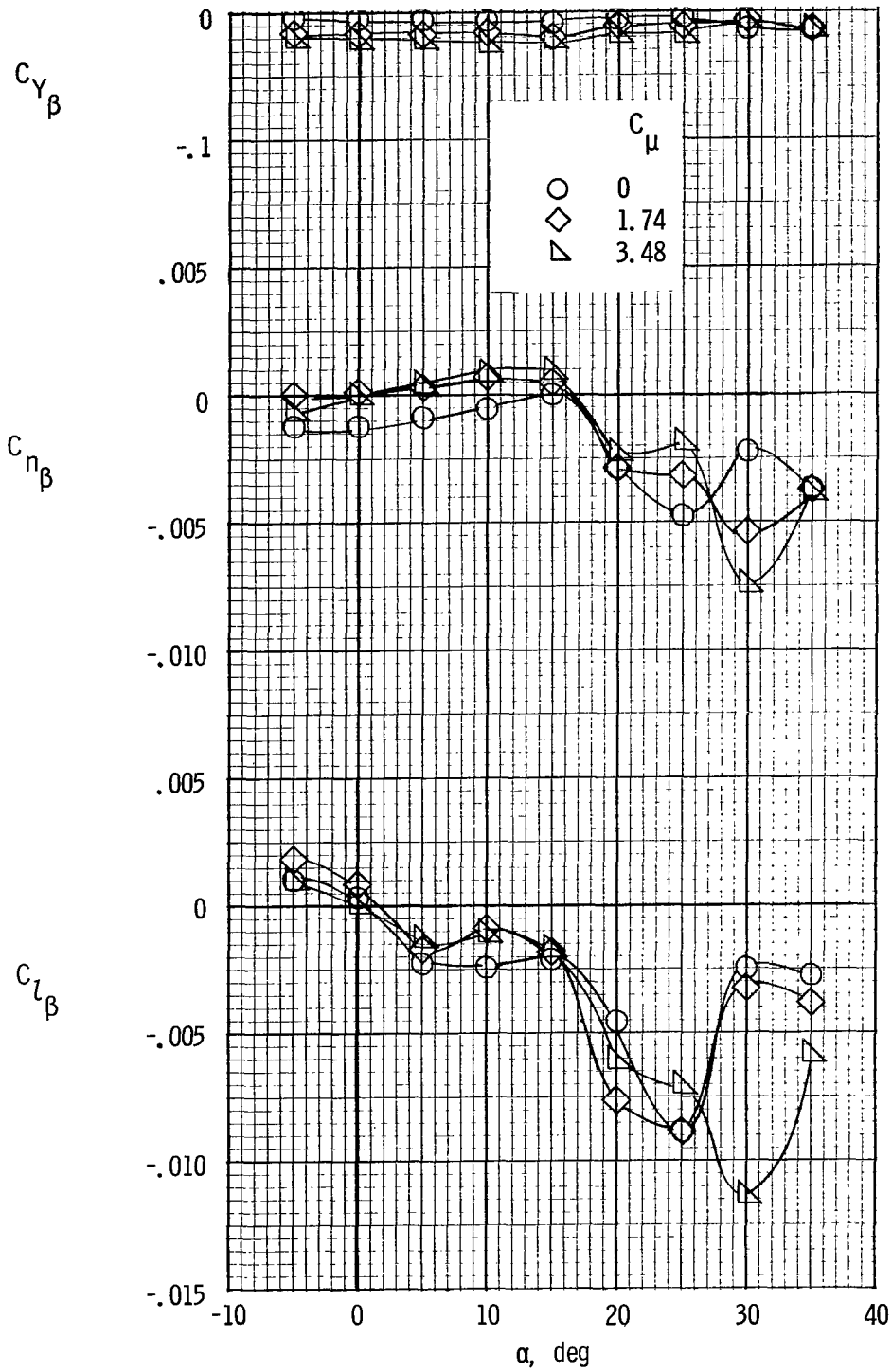

(a) $\delta_f = 35^o$; tails off.

Figure 8.- Static lateral-directional stability derivatives of model for various engine gross-thrust coefficients. $C_{\mu,le} = 0$.

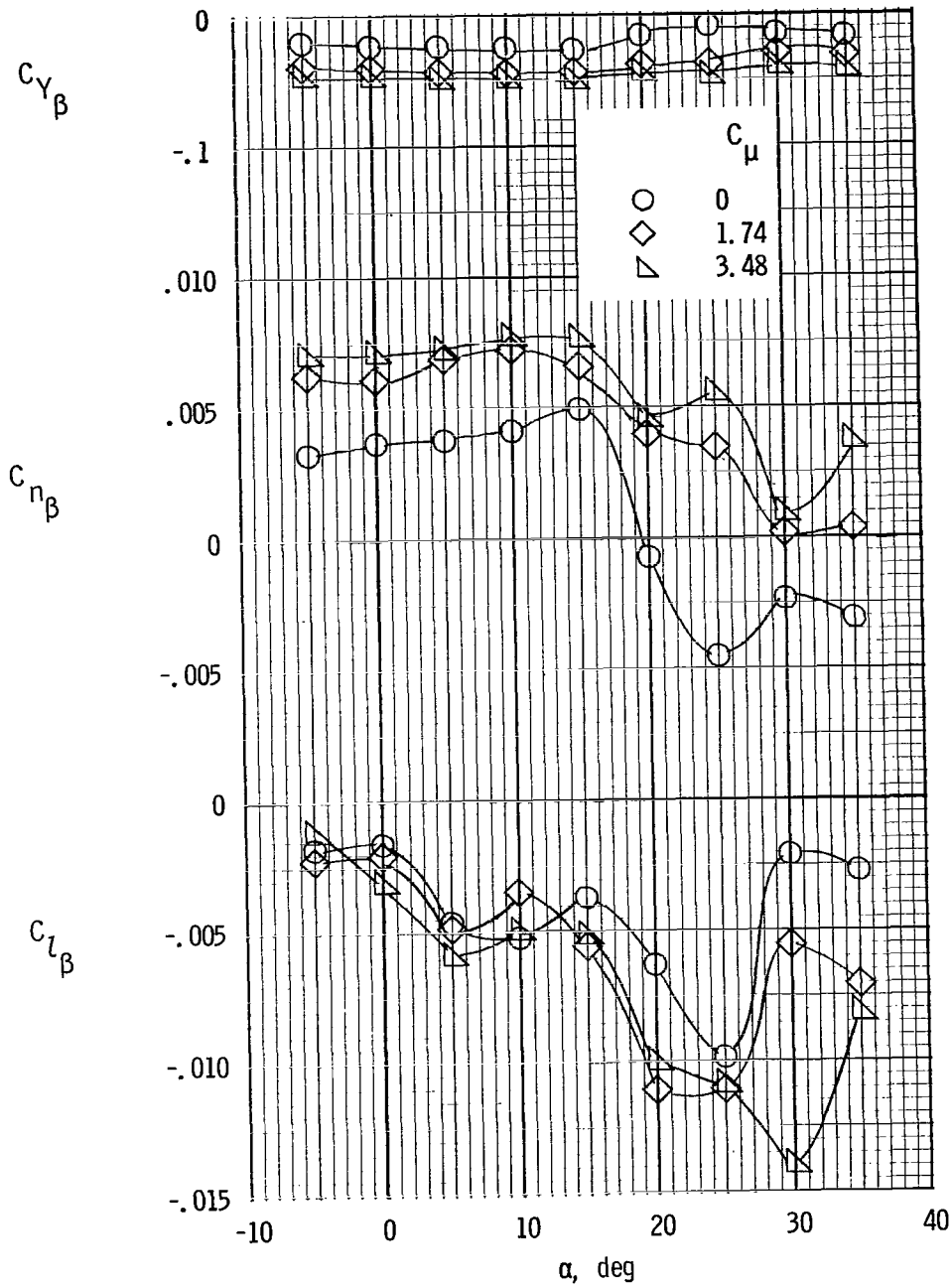

(b) $\delta_f = 35^o$; tails on; $i_t = 0^o$; $\delta_e = -50^o$.

Figure 8.- Continued.

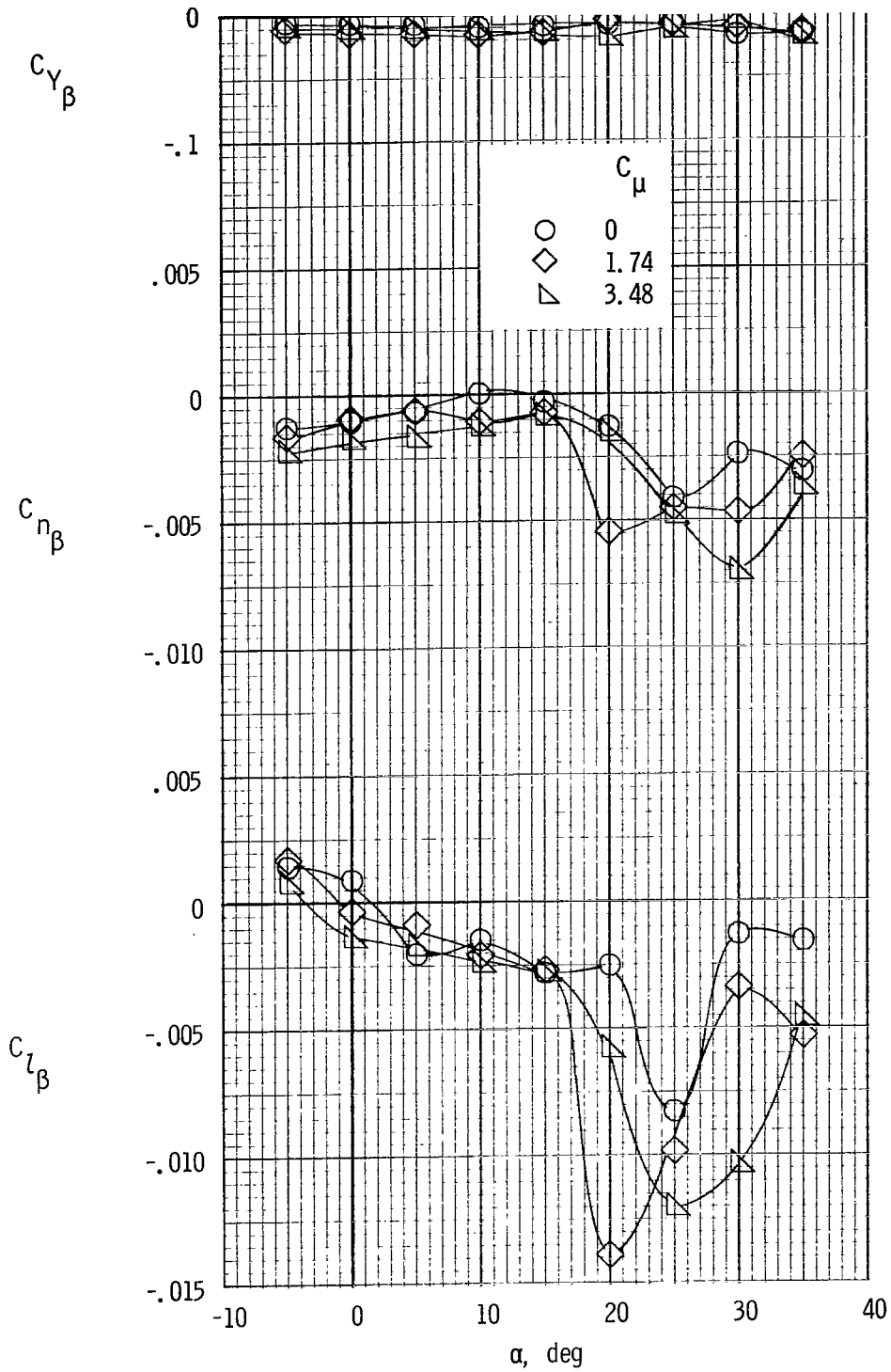

(c) $\delta_f = 50^o$; tails off.

Figure 8.- Continued.

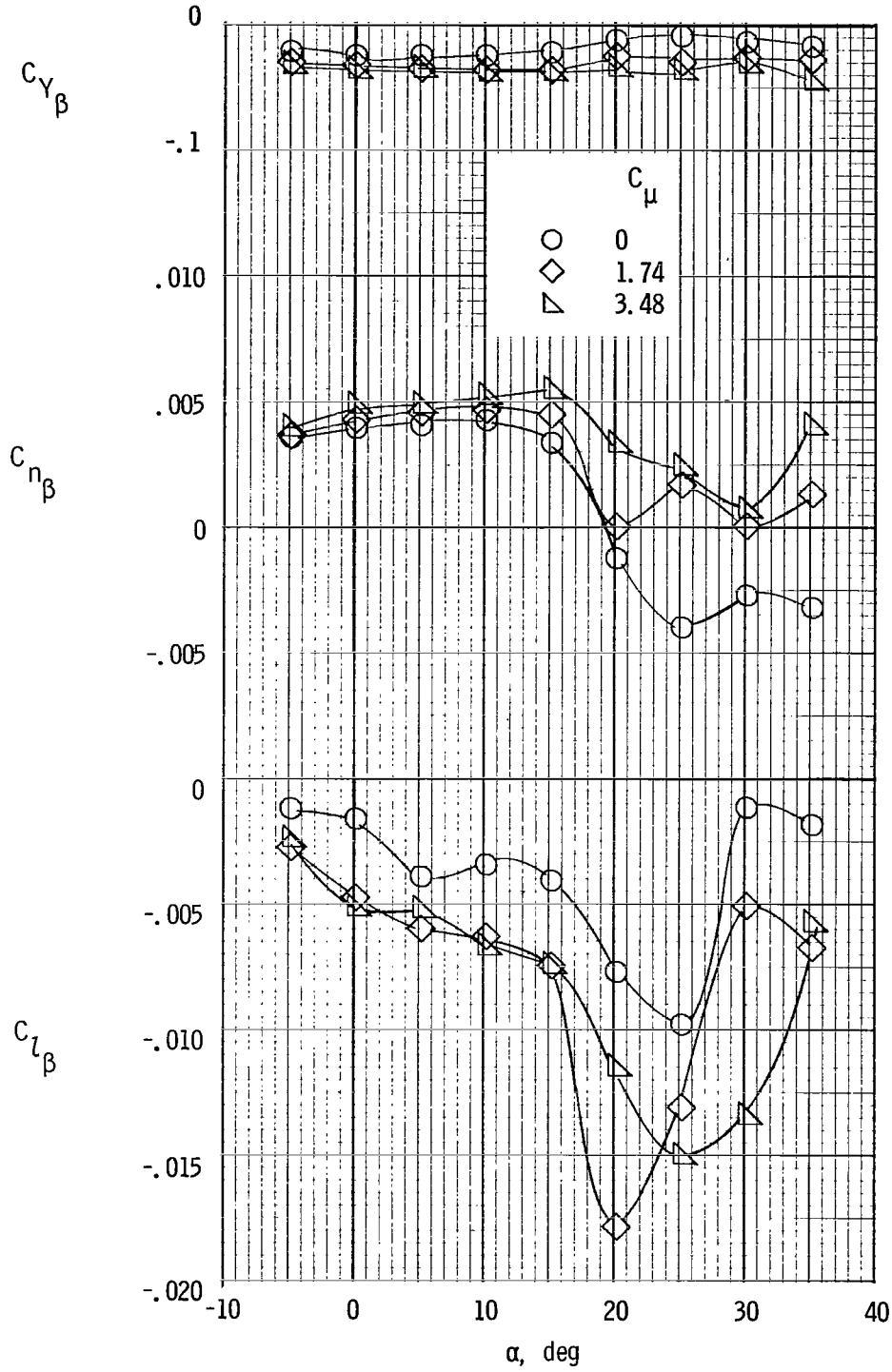

(d) $\delta_f = 50^o$; tails on; $i_t = 0^o$; $\delta_e = -50^o$.

Figure 8.- Continued.

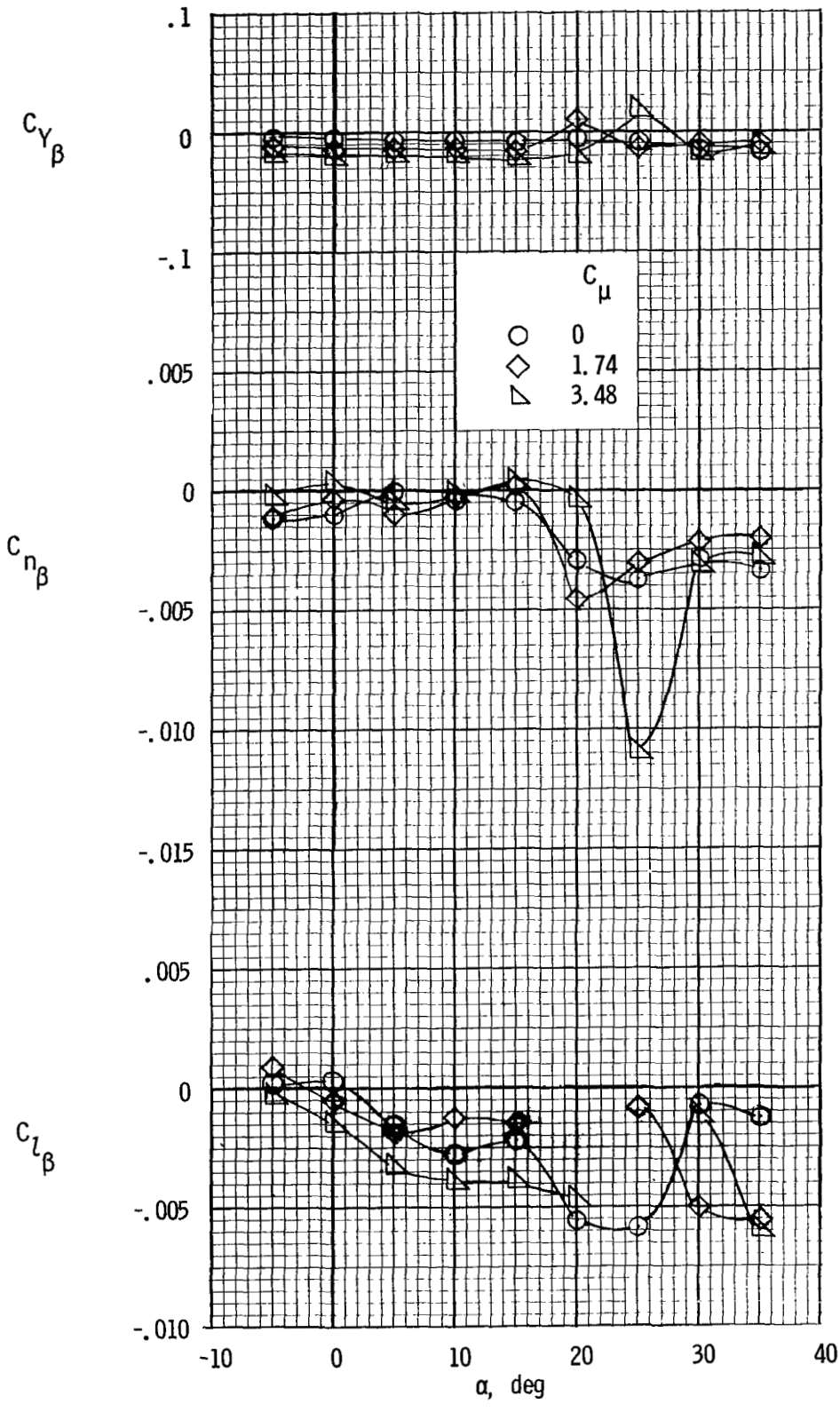

(e) $\delta_f = 70^o$; tails off.

Figure 8.- Continued.

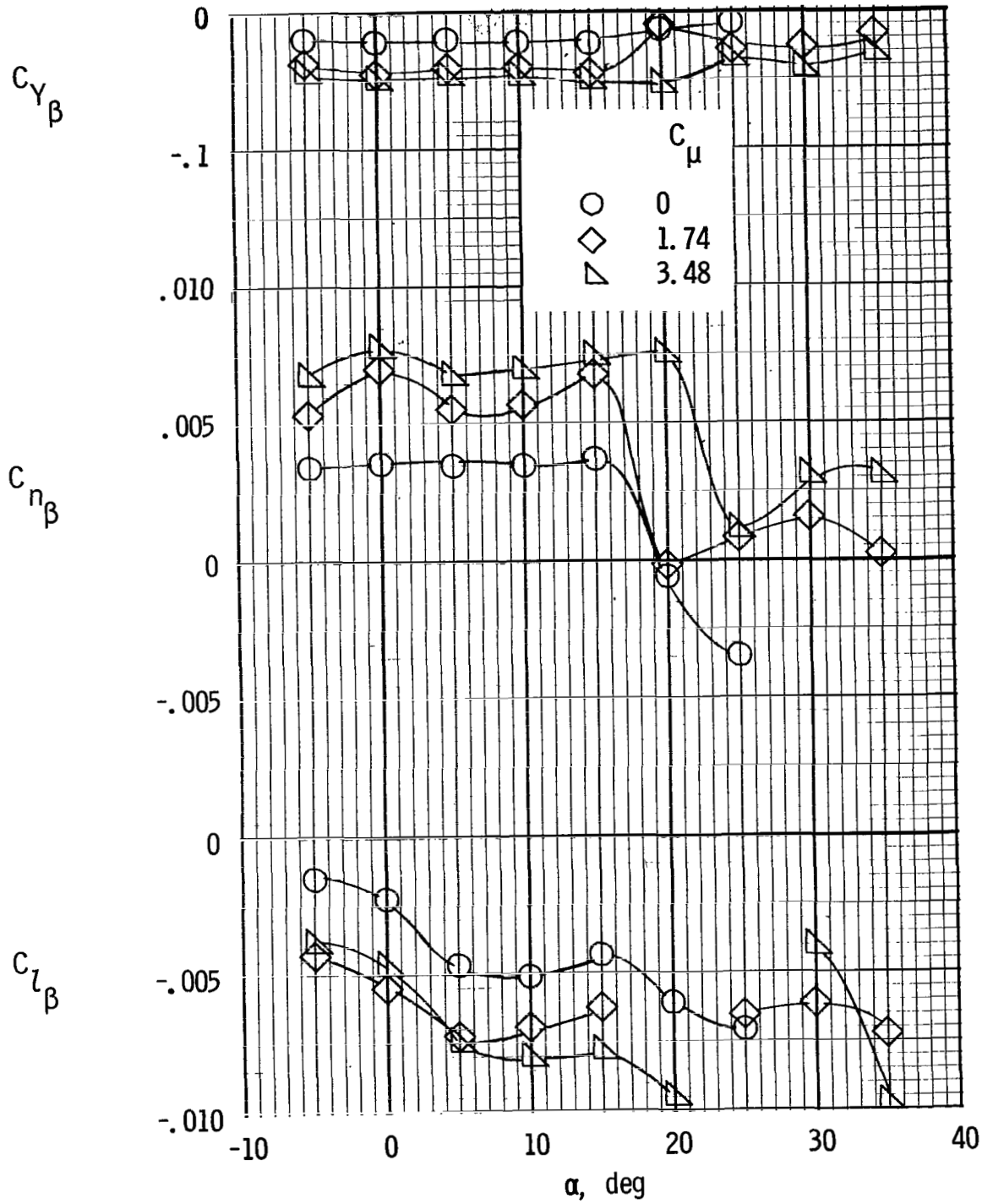

(f) $\delta_f = 70^o$; tails on; $i_t = 0^o$; $\delta_e = -50^o$.

Figure 8.- Concluded.

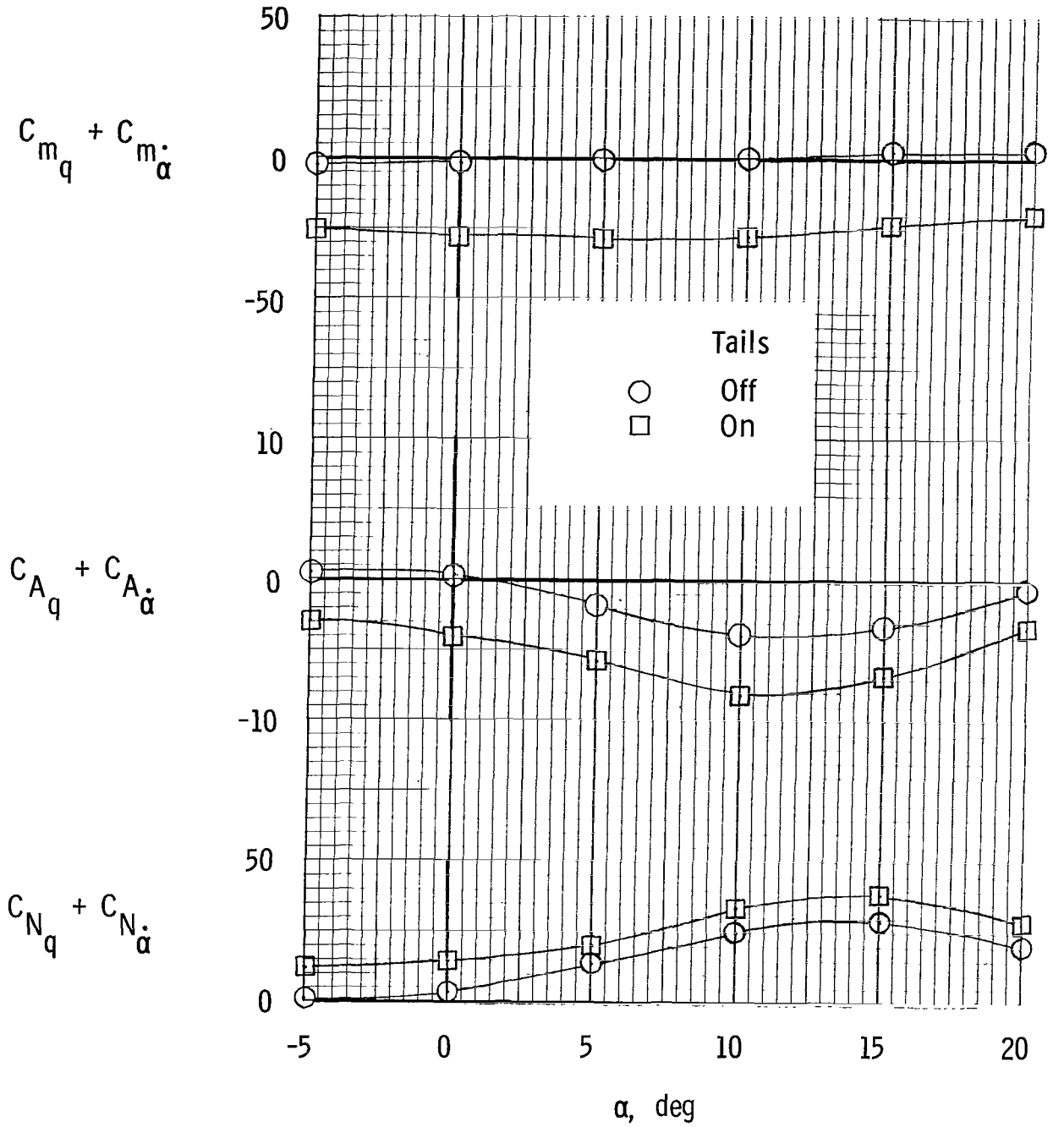

Figure 9.- Oscillatory pitching derivatives for clean configuration. $\delta_f = 0^o$; $i_t = 0^o$; $\delta_e = 0^o$; $k = 0.0734$; $C_\mu = 0$.

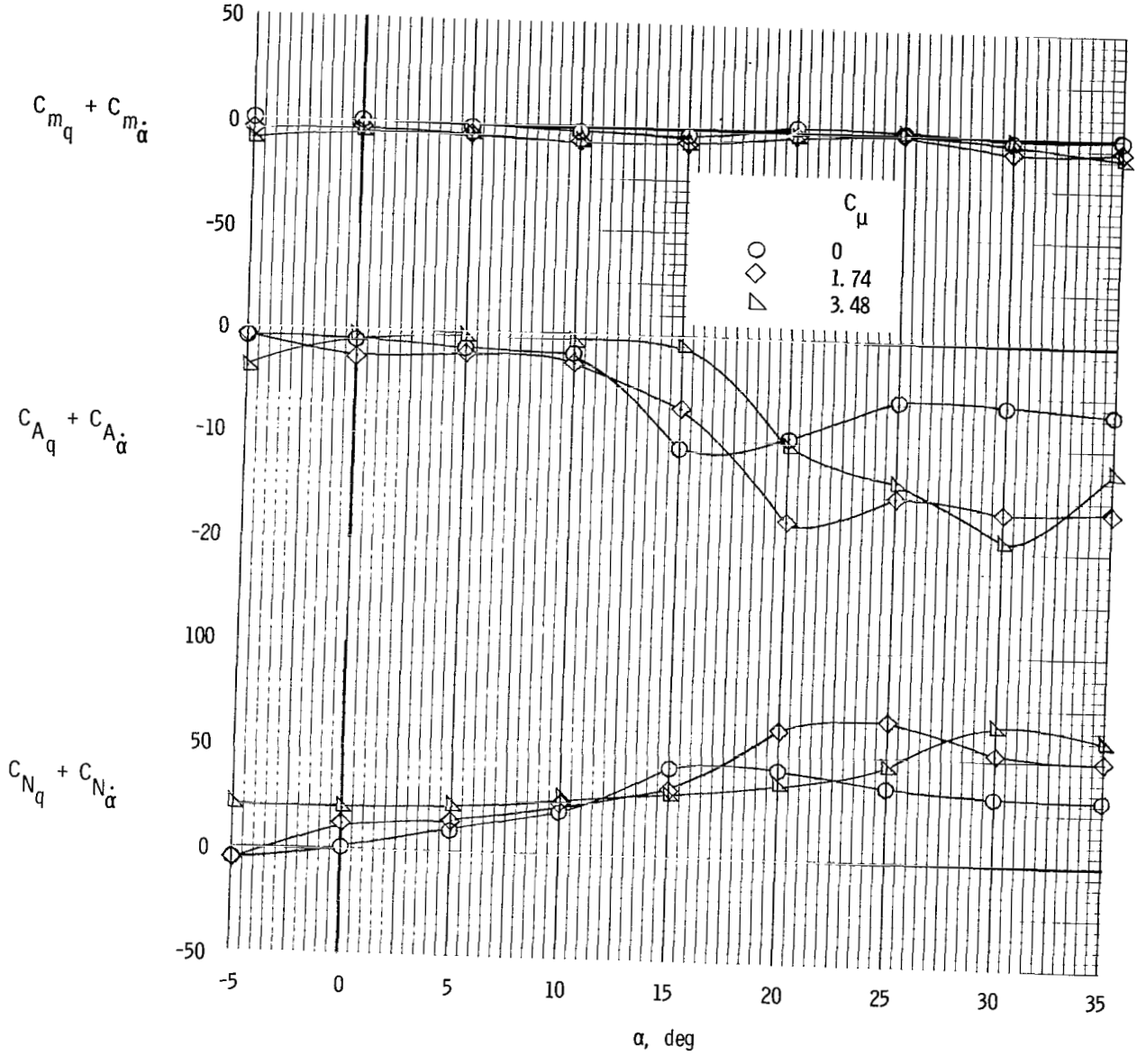

(a) $C_{\mu,le} = 0.$

Figure 10.- Oscillatory pitching derivatives of model with tails off and $\delta_f = 35^o$. k = 0.0734.

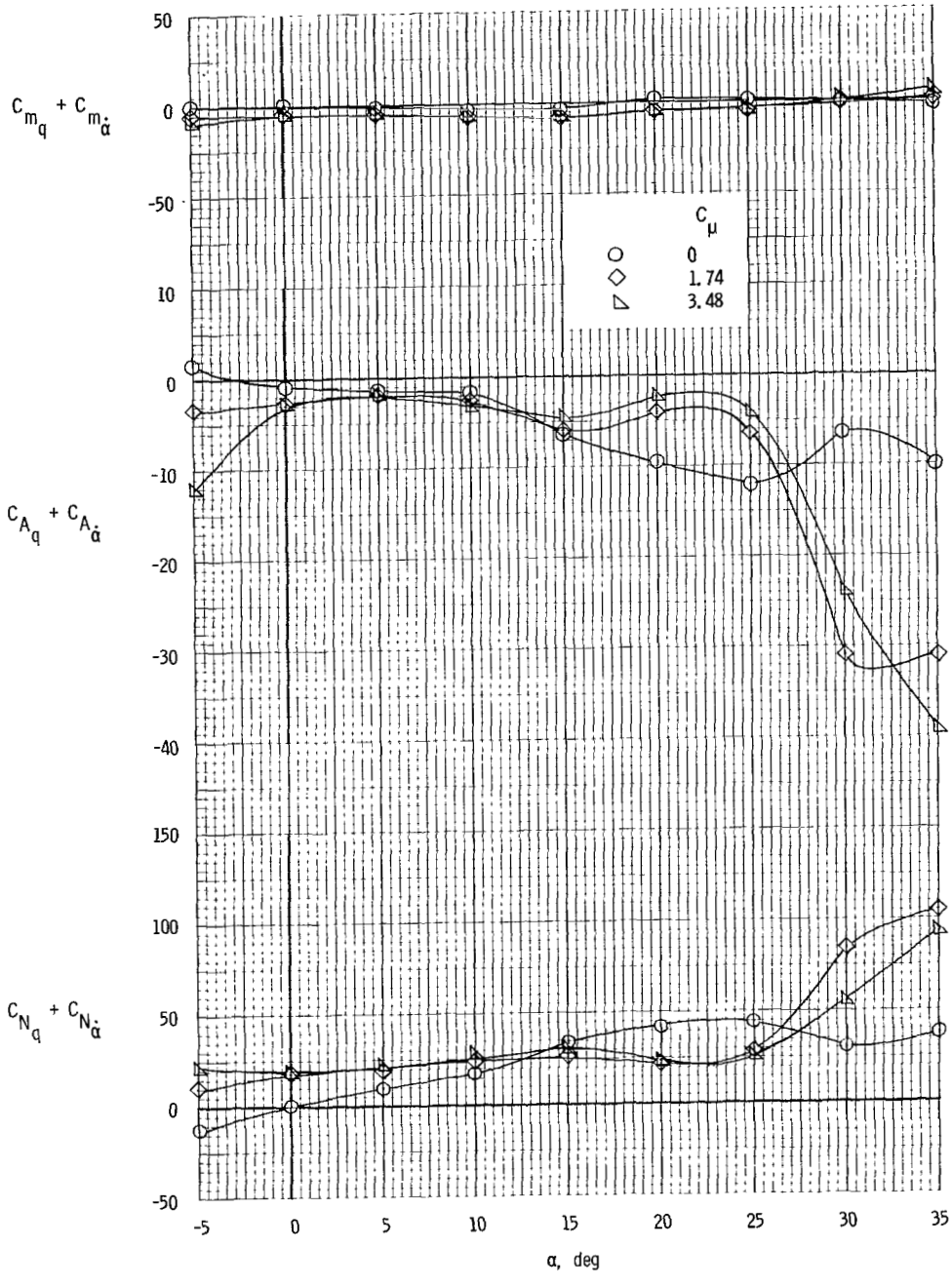

(b) $C_{\mu,le} = 0.024$.

Figure 10.- Concluded.

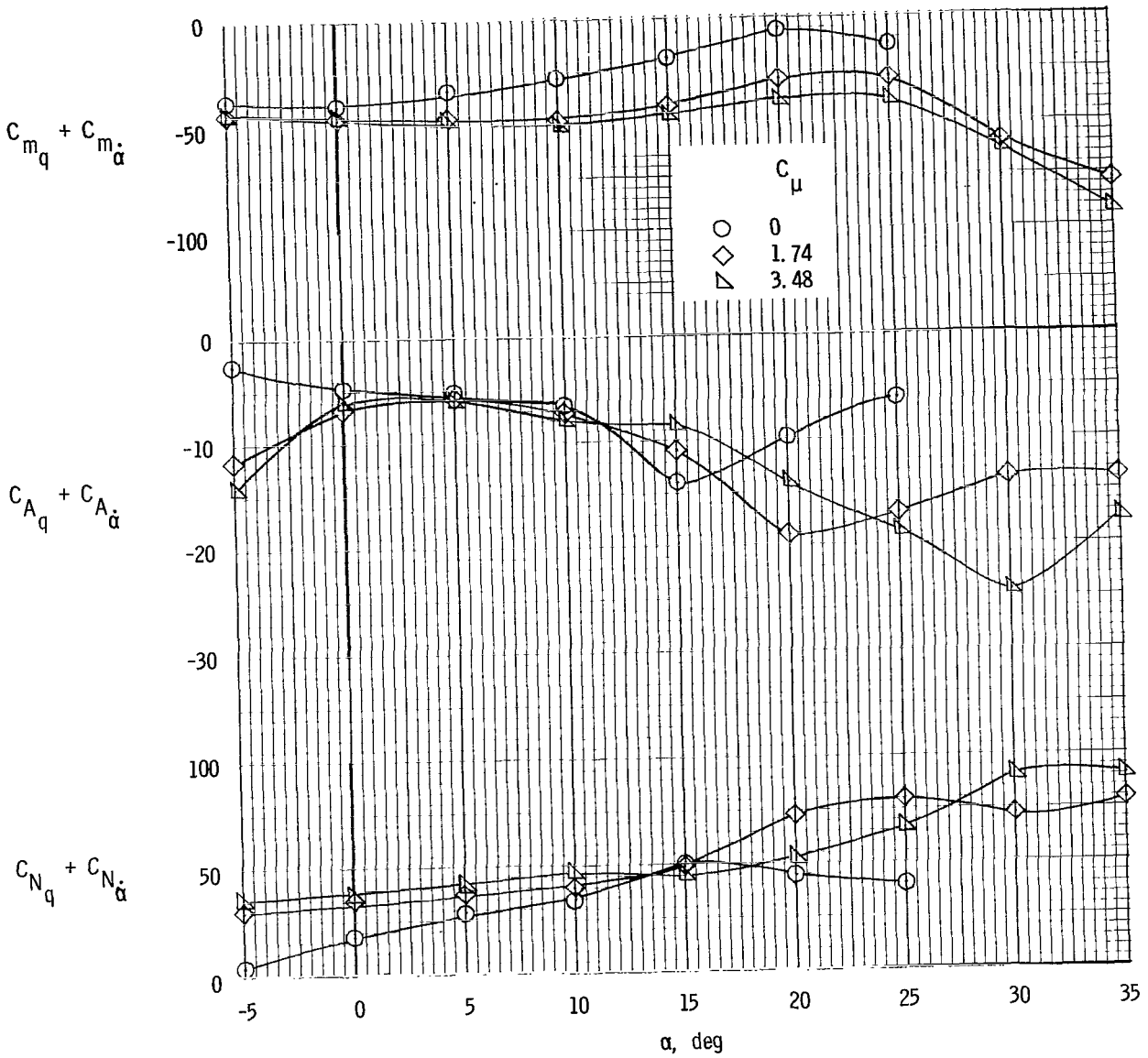

(a) k = 0.0734; $C_{\mu,le} = 0.$

Figure 11.- Oscillatory pitching derivatives of model with tails on and $\delta_f = 35^o$. $i_t = 0^o$; $\delta_e = -50^o$.

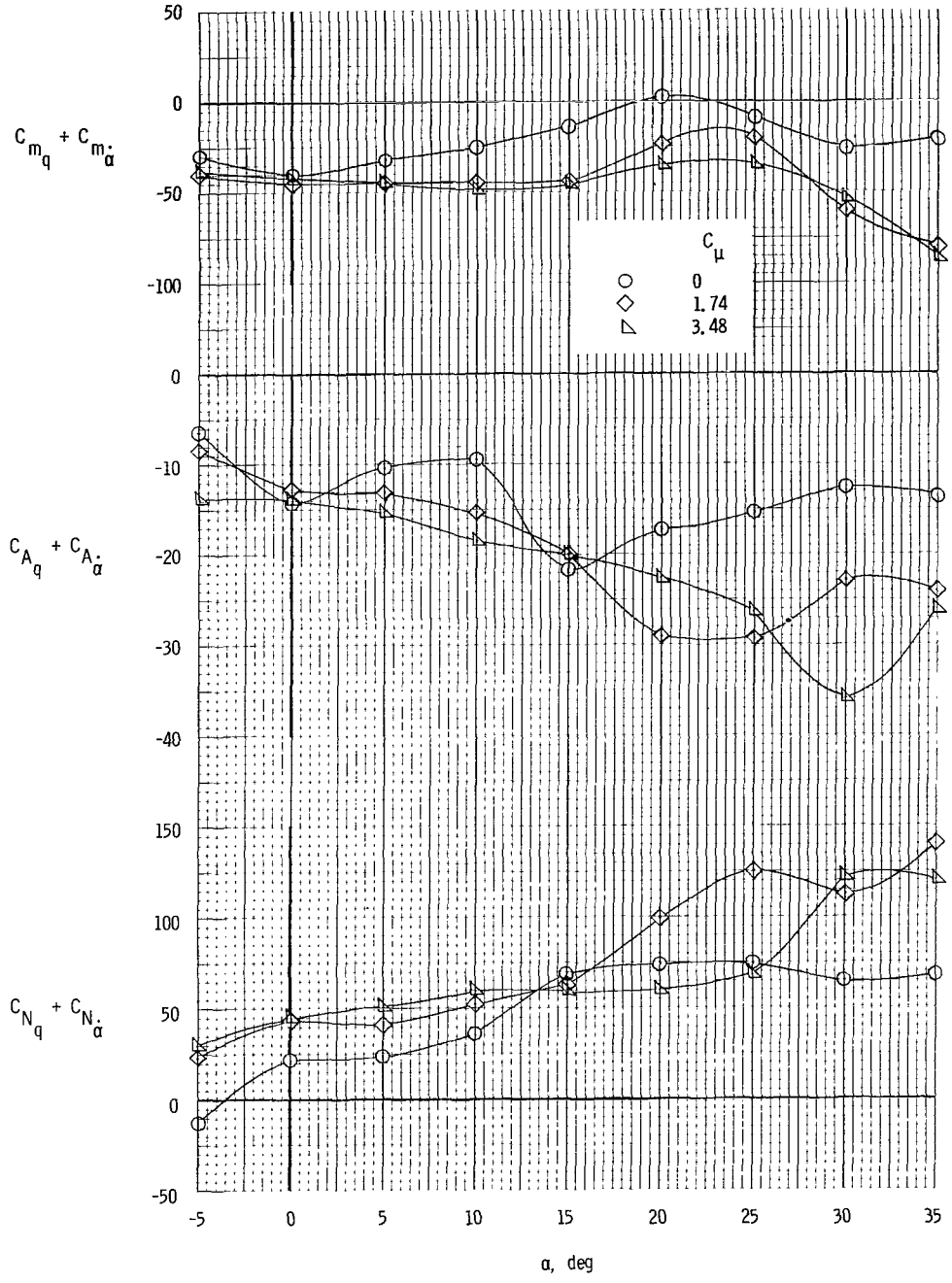

(b) k = 0.0367; $C_{\mu,le} = 0.$

Figure 11.- Continued.

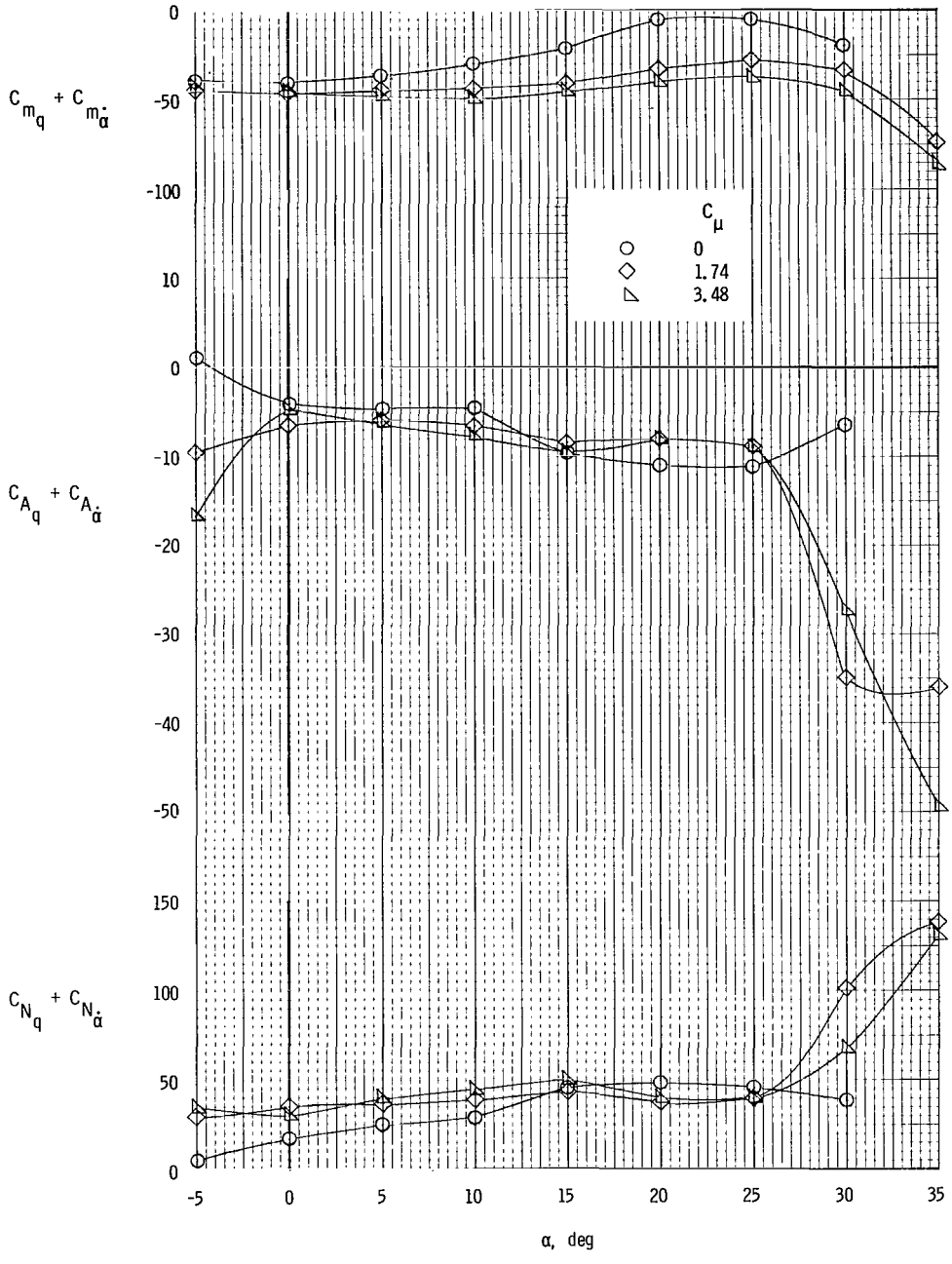

(c) k = 0.0734; $C_{\mu,le}$ = 0.024.

Figure 11.- Concluded.

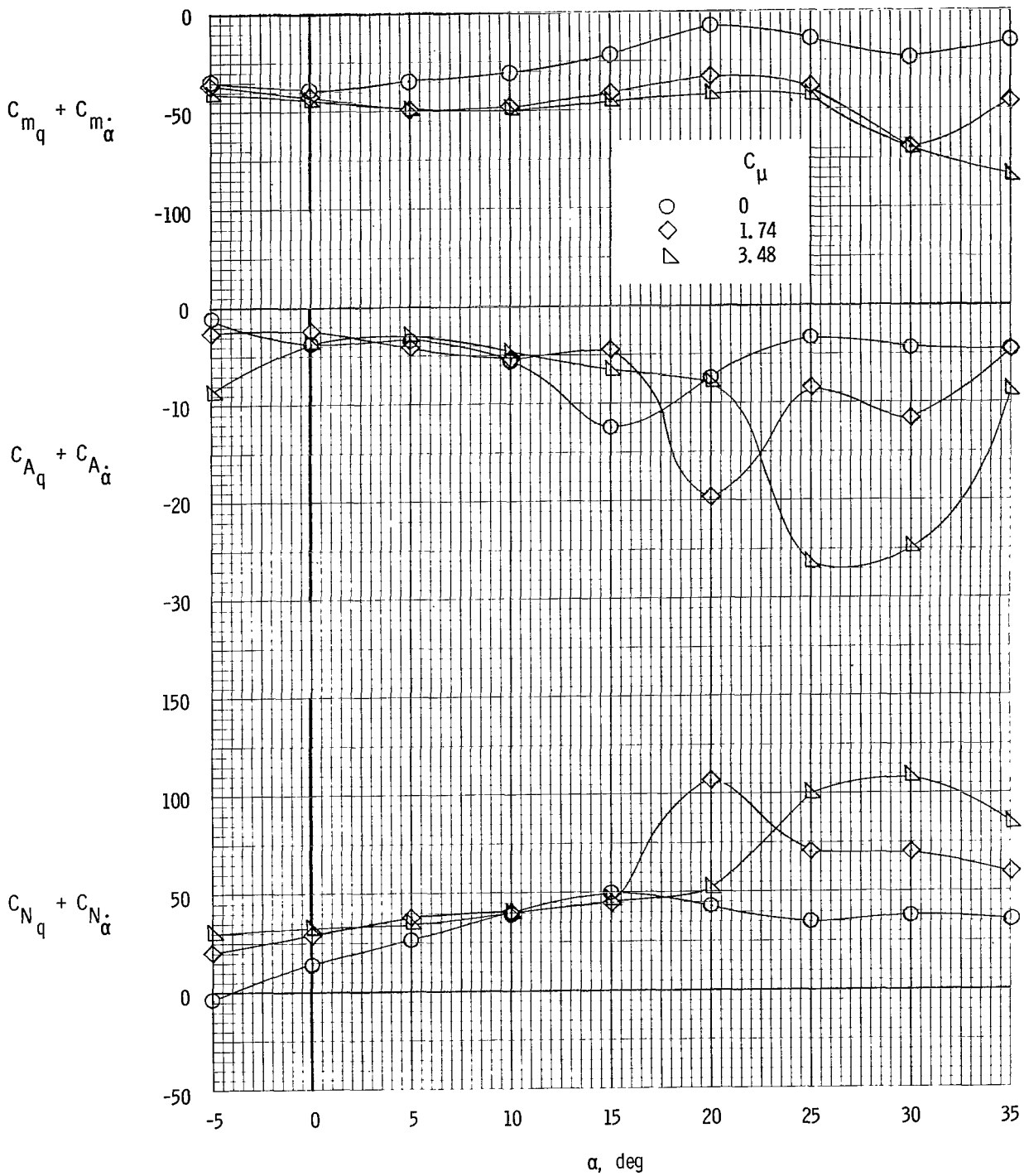

(a) k = 0.0734; $C_{\mu,le} = 0$.

Figure 12.- Oscillatory pitching derivatives of model with tails on and $\delta_f = 50^o$. $i_t = 0^o$; $\delta_e = -50^o$.

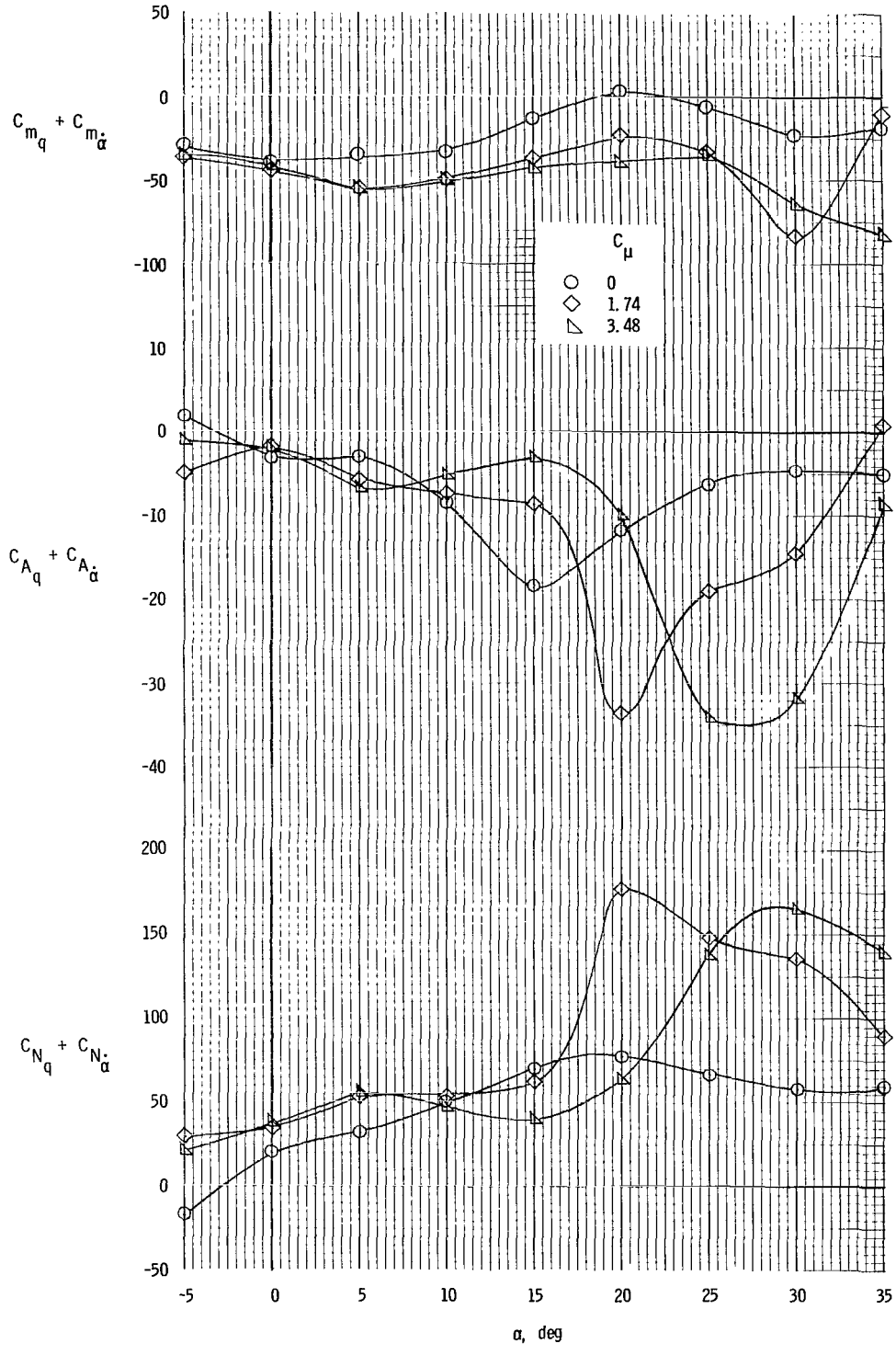

(b) k = 0.0367; $C_{\mu,le} = 0$.

Figure 12.- Continued.

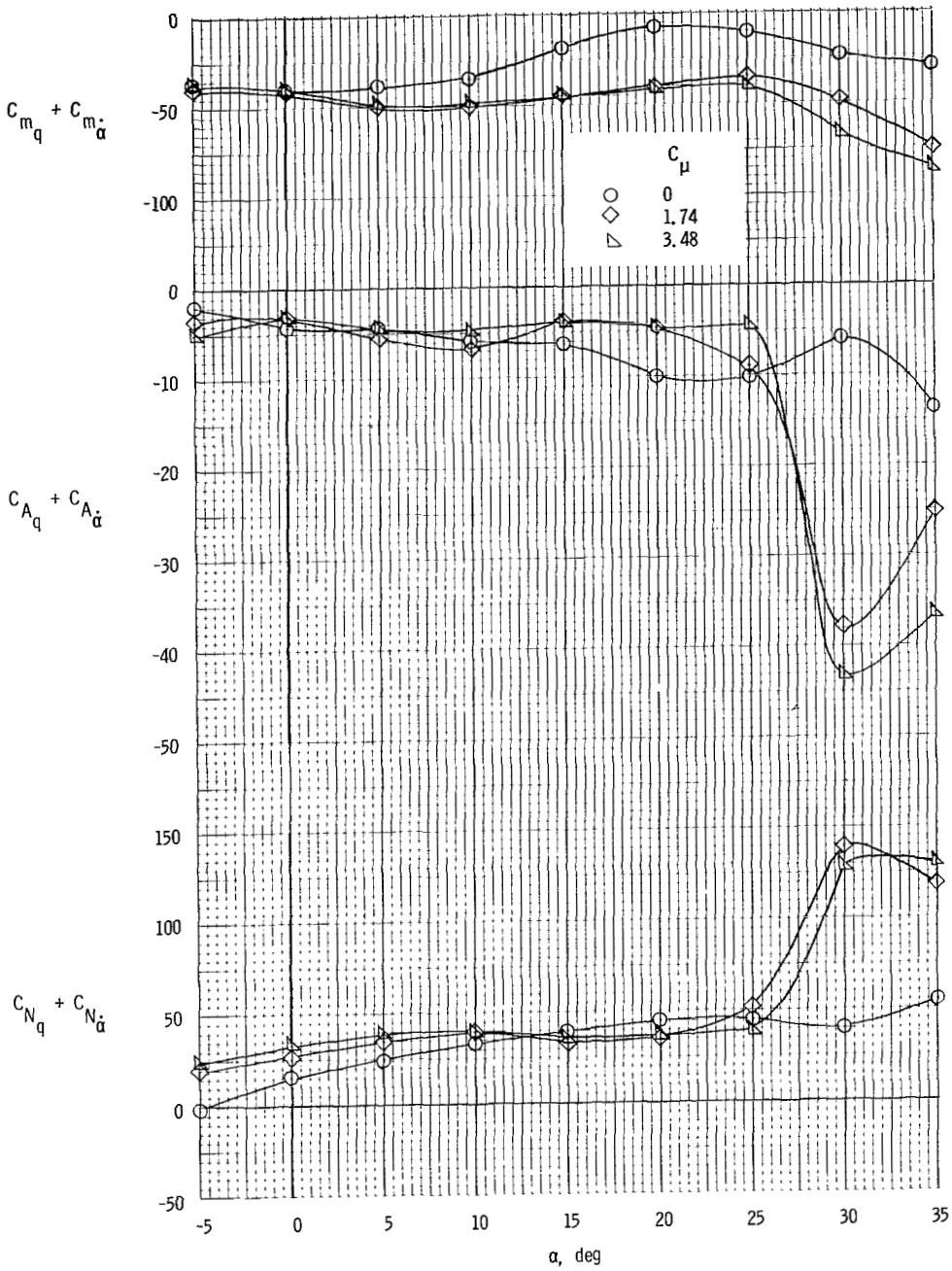

(c) k = 0.0734; $C_{\mu,le} = 0.024$.

Figure 12.- Concluded.

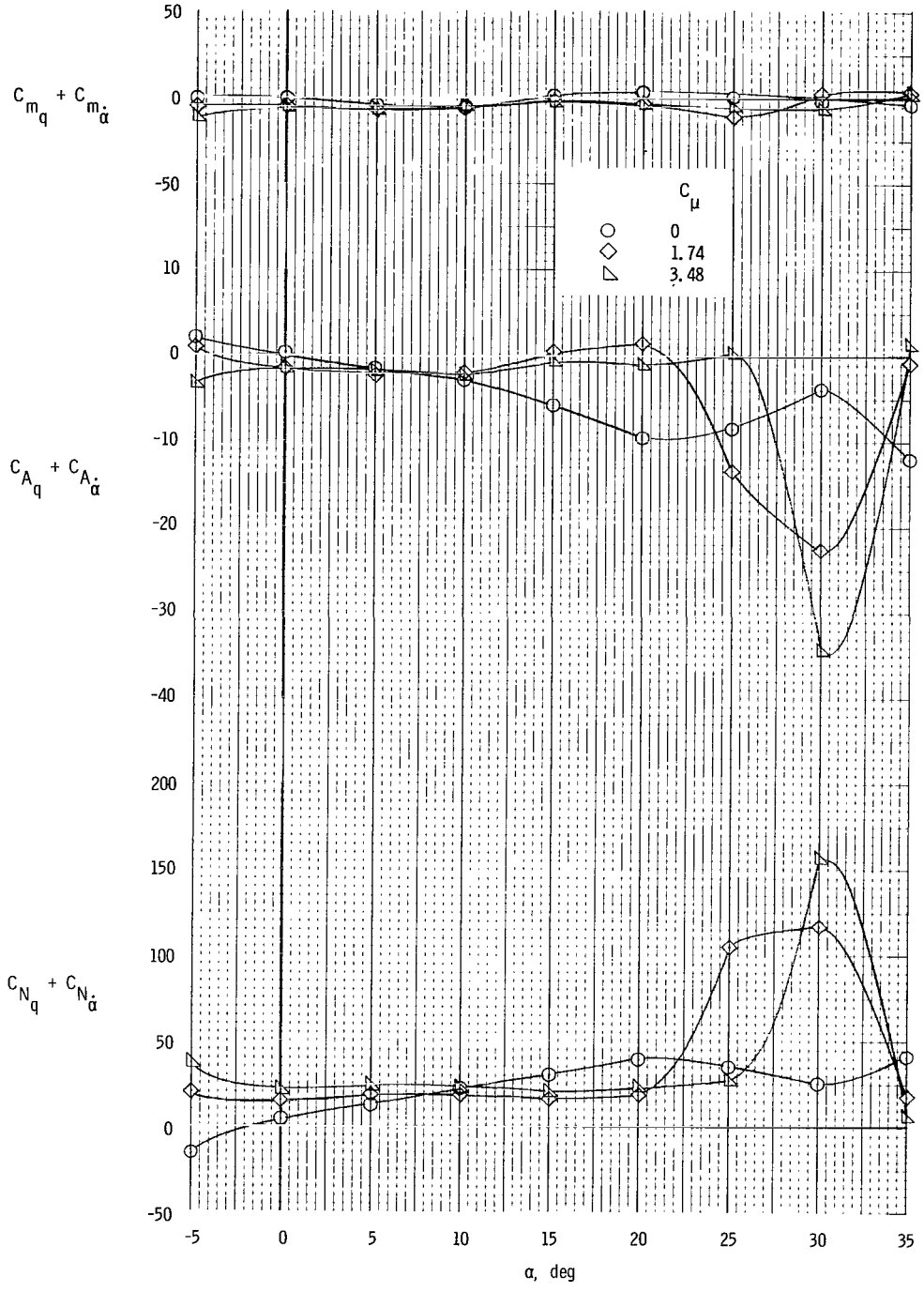

(a) $C_{\mu,le} = 0.024$.

Figure 13.- Oscillatory pitching derivatives of model with tails off and $\delta_f = 70^o$. k = 0.0734.

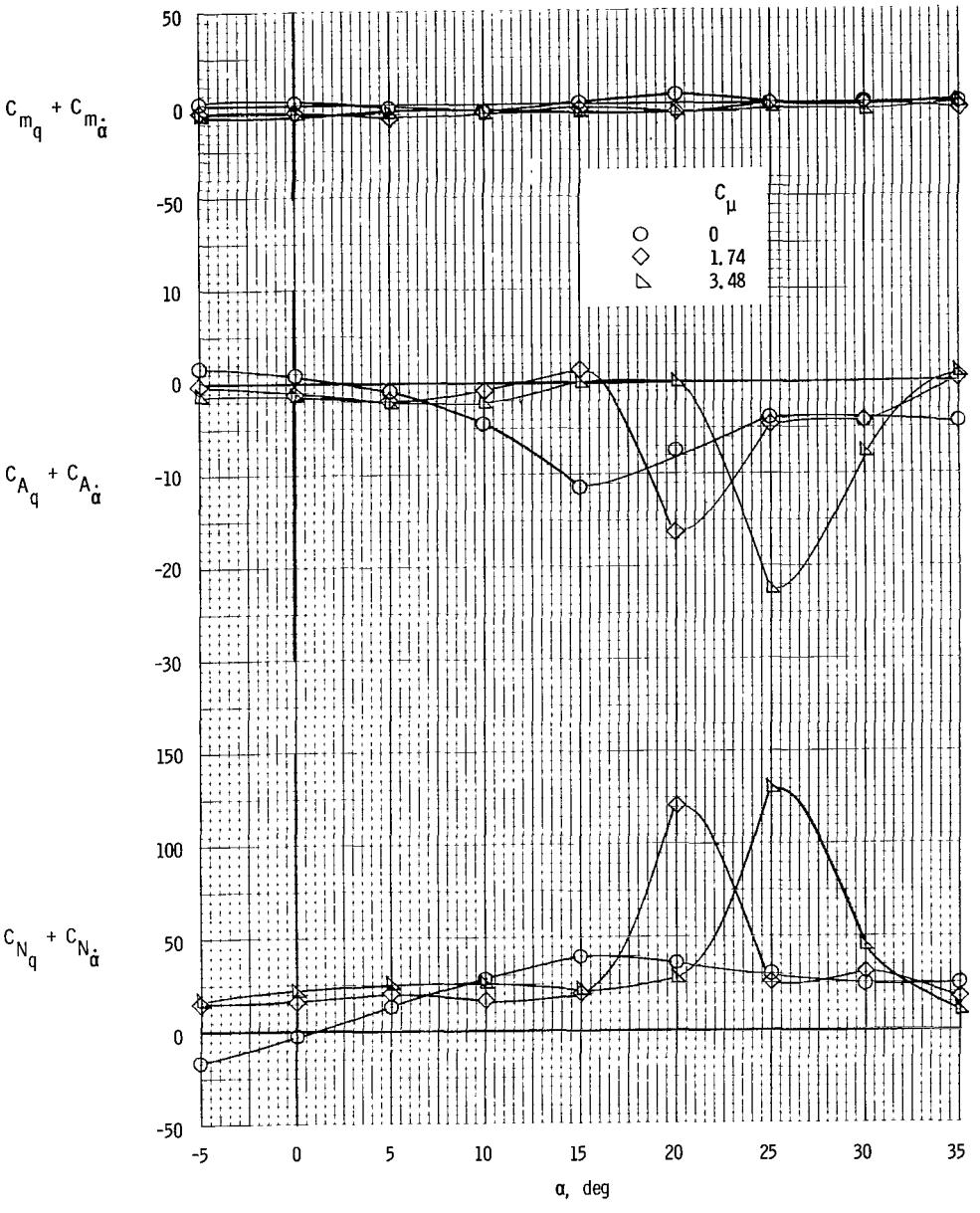

(b) $C_{\mu,le} = 0$.

Figure 13.- Concluded.

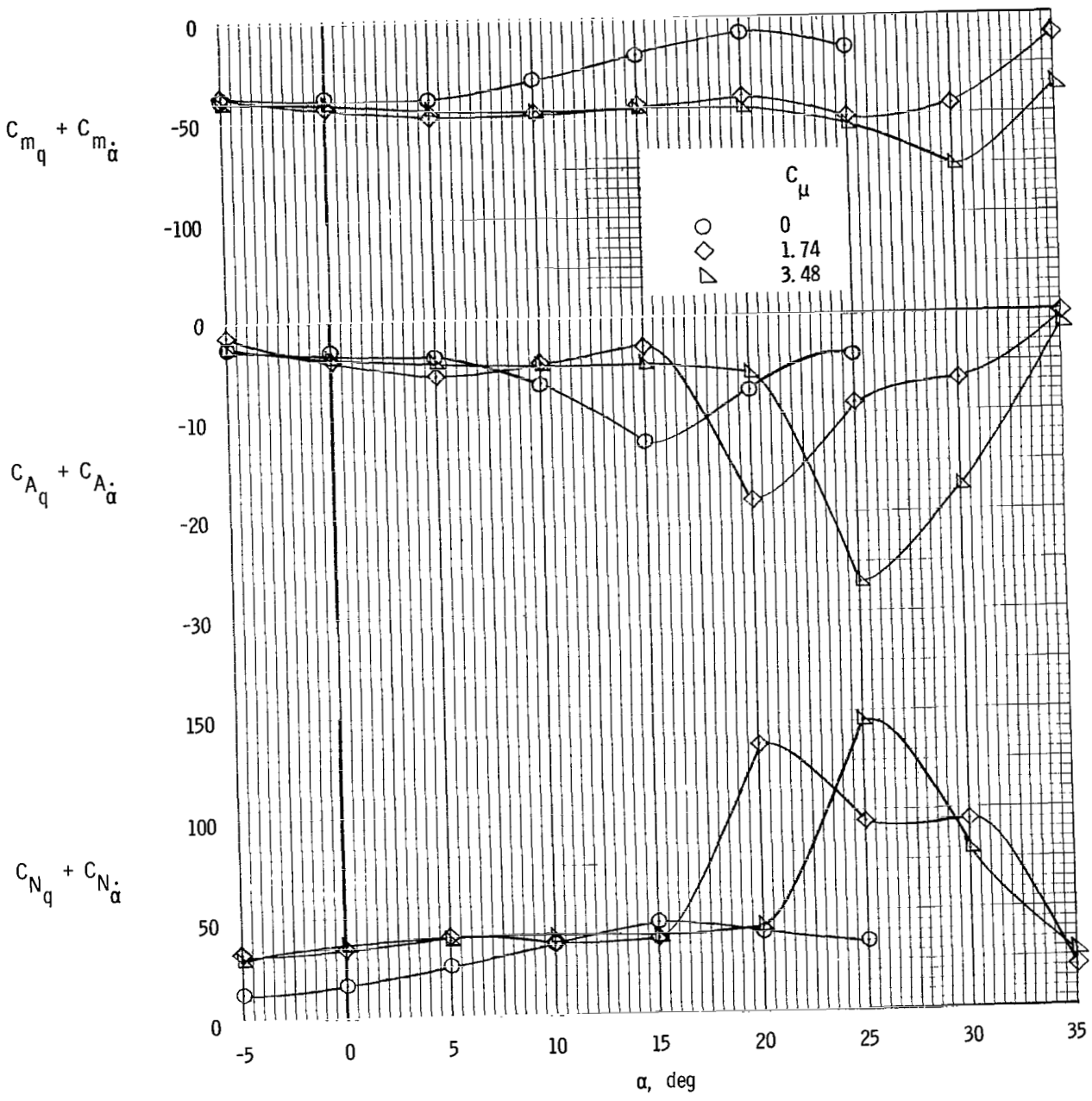

(a) k = 0.0734; $C_{\mu,le} = 0$.

Figure 14.- Oscillatory pitching derivatives of model with tails on and $\delta_f = 70^o$. $i_t = 0^o$; $\delta_e = -50^o$.

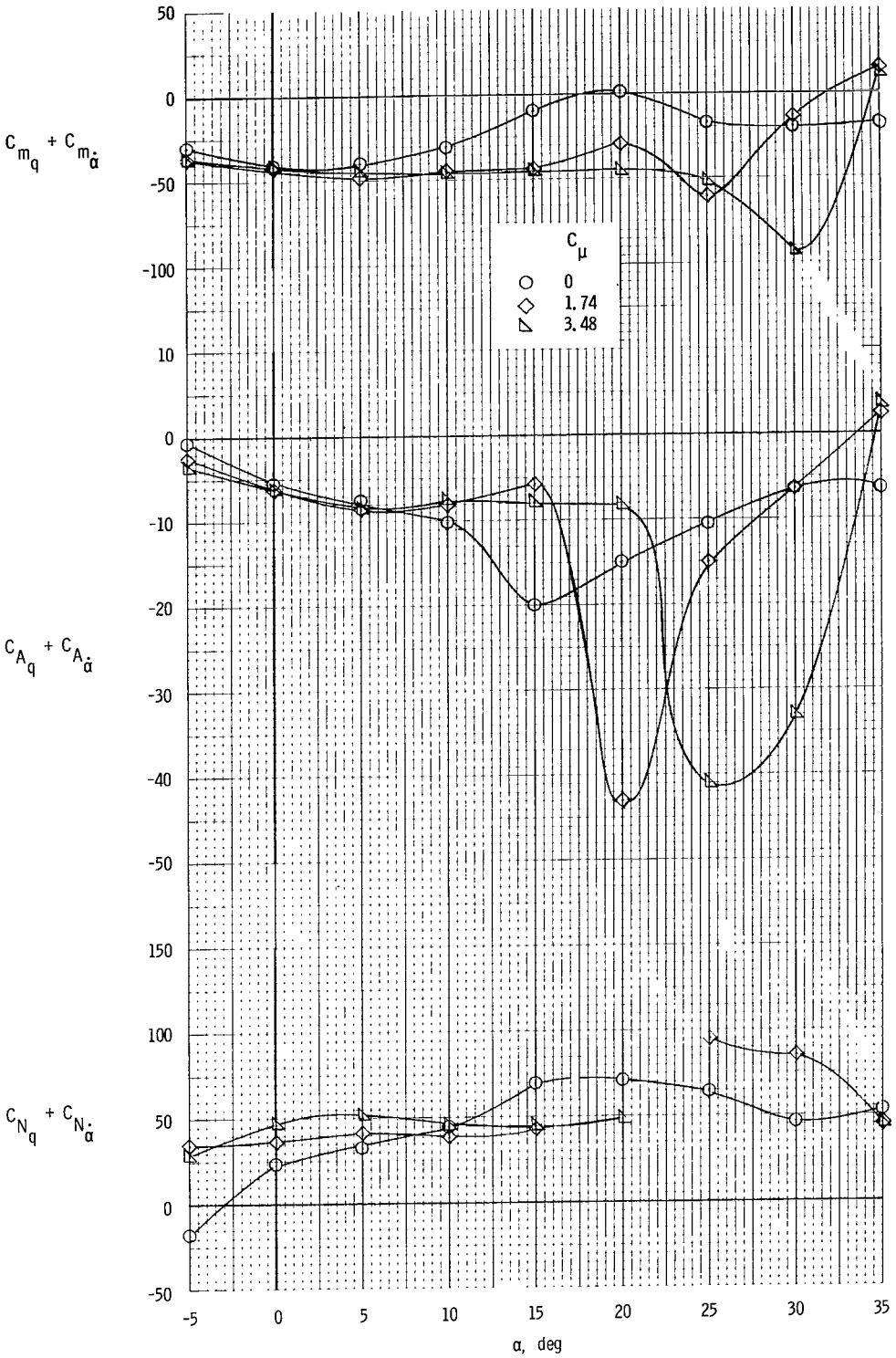

(b) k = 0.0367; $C_{\mu,le} = 0$.

Figure 14.- Continued.

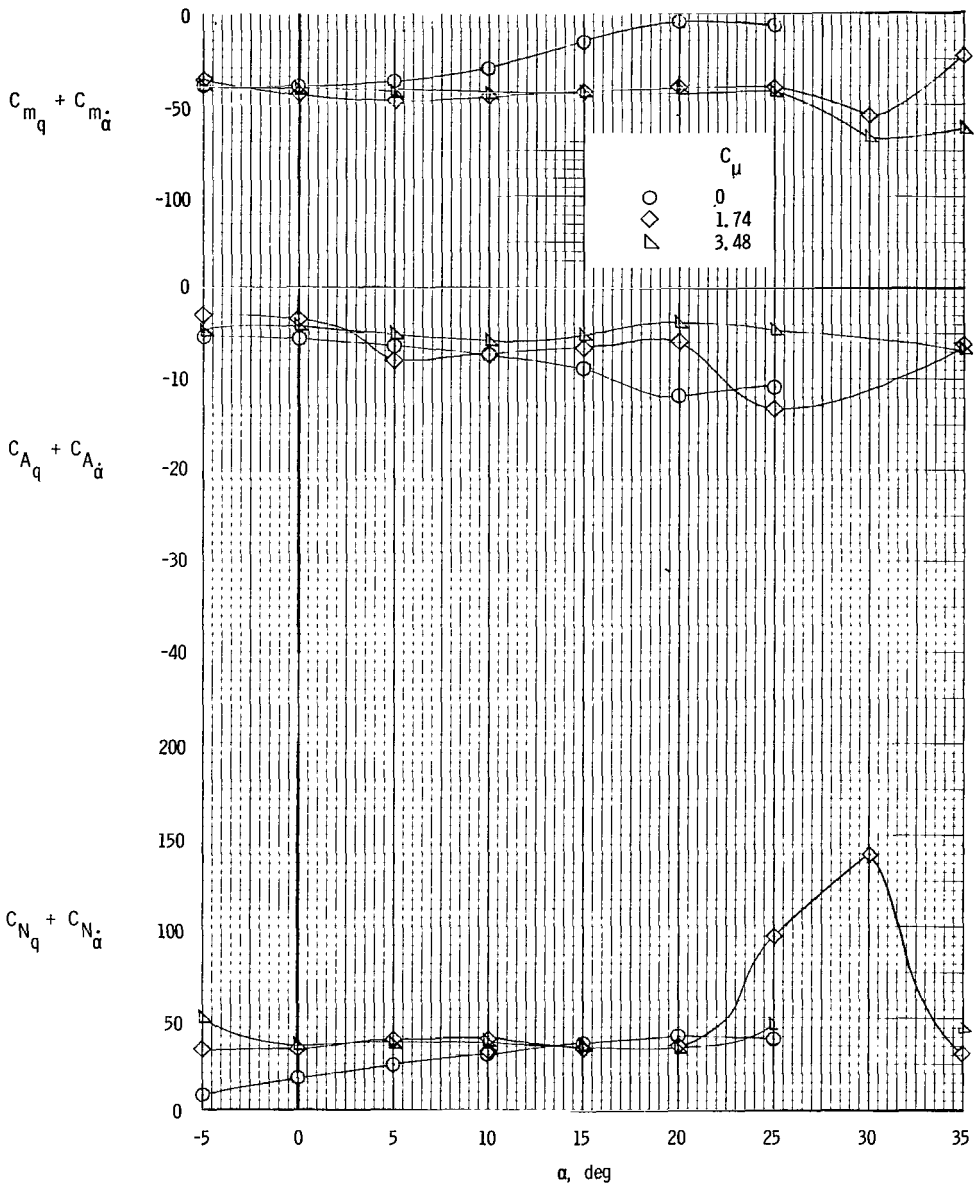

(c) k = 0.0734; $C_{\mu,le} = 0.024$.

Figure 14.- Concluded.

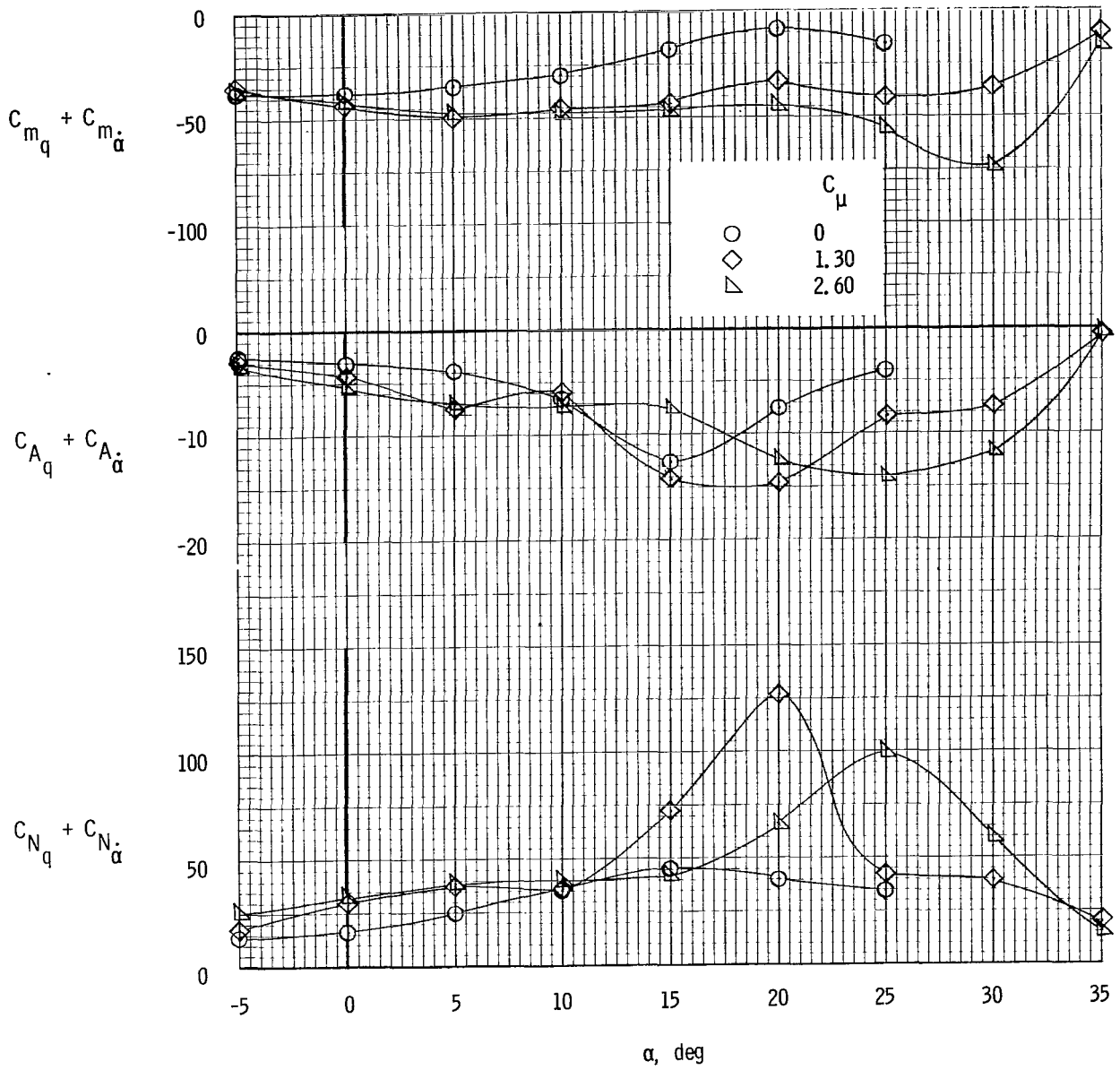

(a) Left outboard engine not operating; $C_{\mu,le} = 0$; $\delta_f = 70^o$.

Figure 15.- Engine-out oscillatory pitching derivatives. $i_t = 0^o$; $\delta_e = -50^o$; $k = 0.0734$.

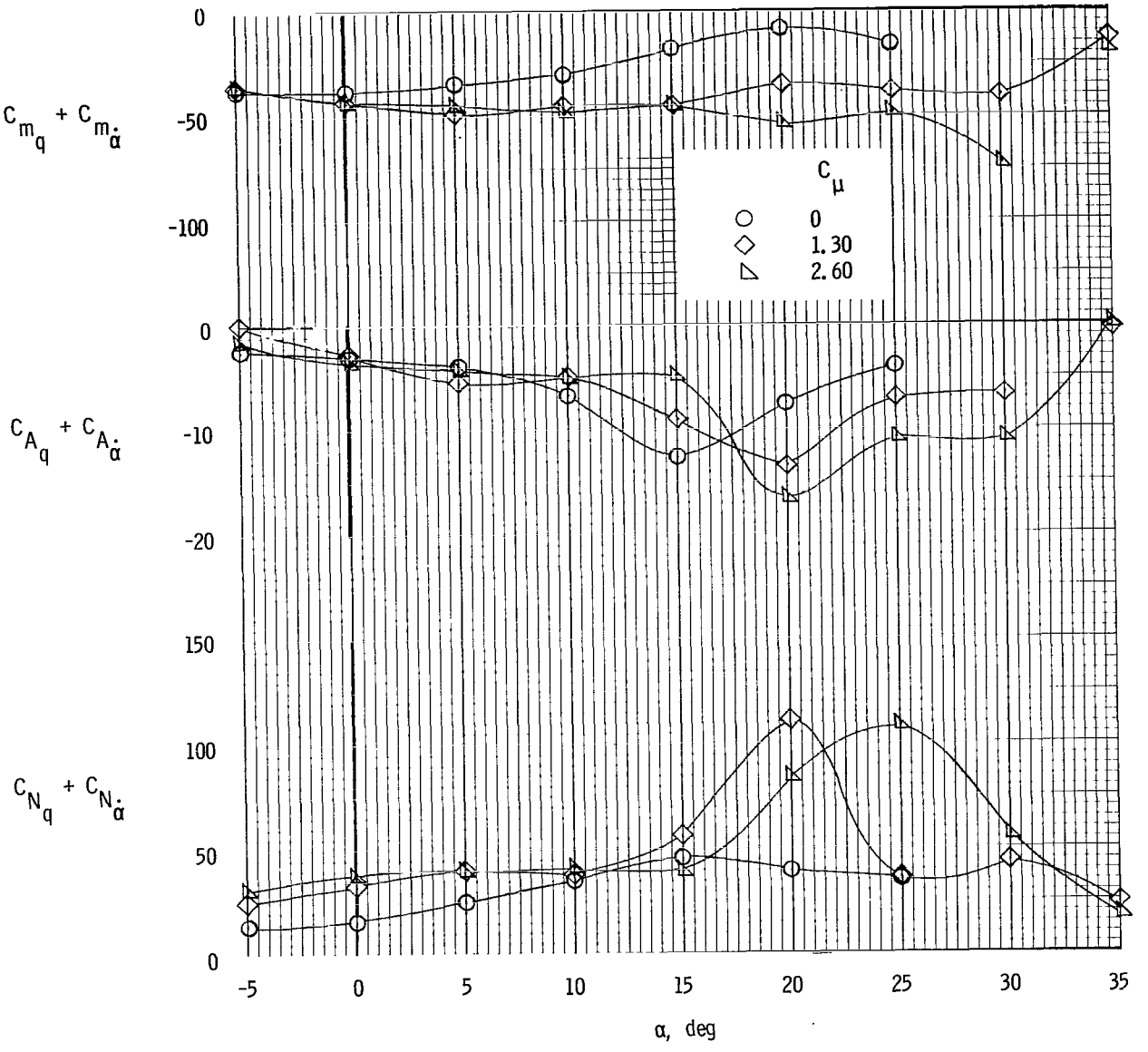

(b) Left inboard engine not operating; $C_{\mu,le} = 0$; $\delta_f = 70^o$.

Figure 15.- Continued.

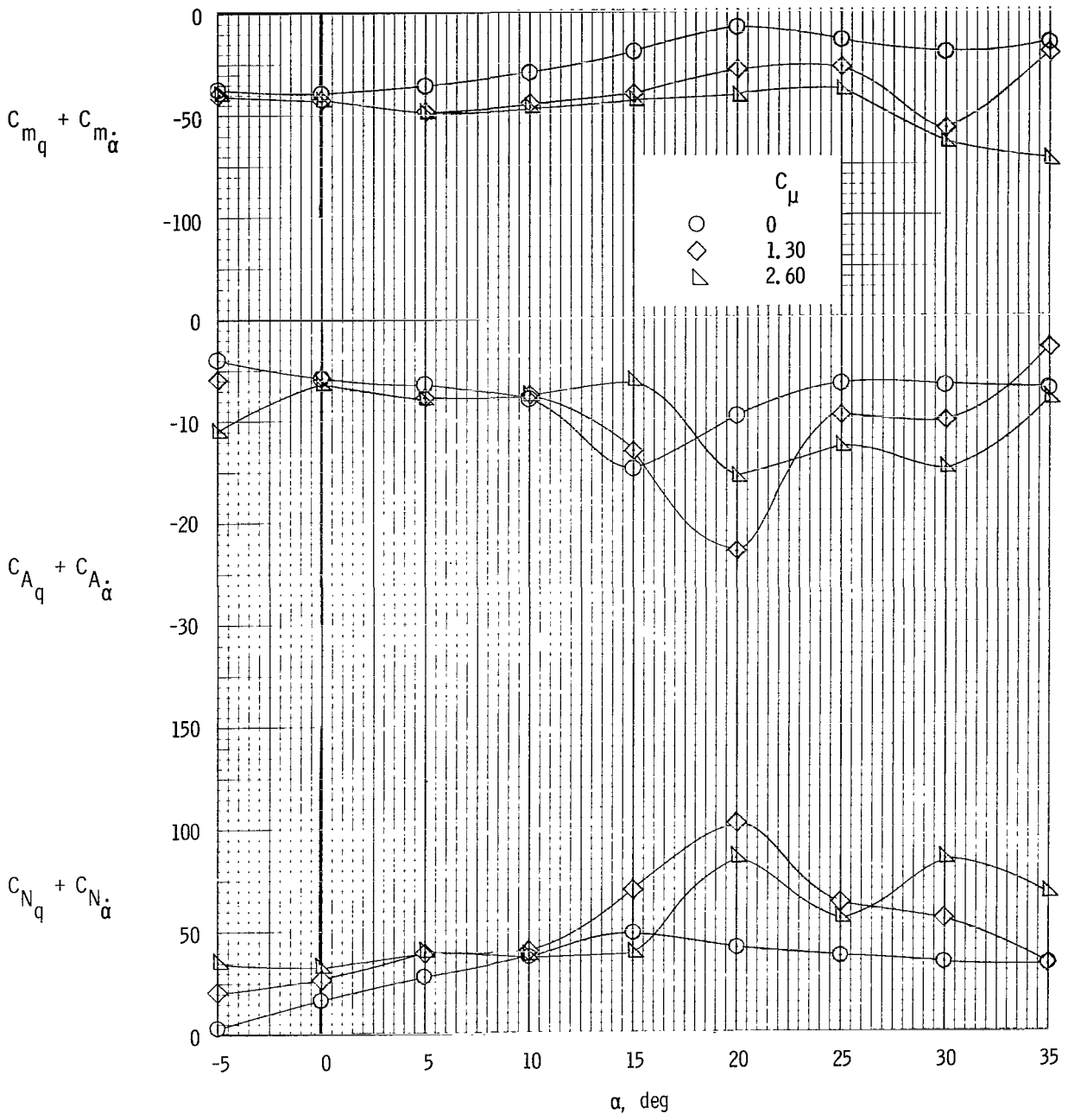

(c) Left outboard engine not operating; $C_{\mu,le} = 0$; $\delta_{f,L} = 70^o$, $\delta_{f,R} = 40^o$.

Figure 15.- Continued.

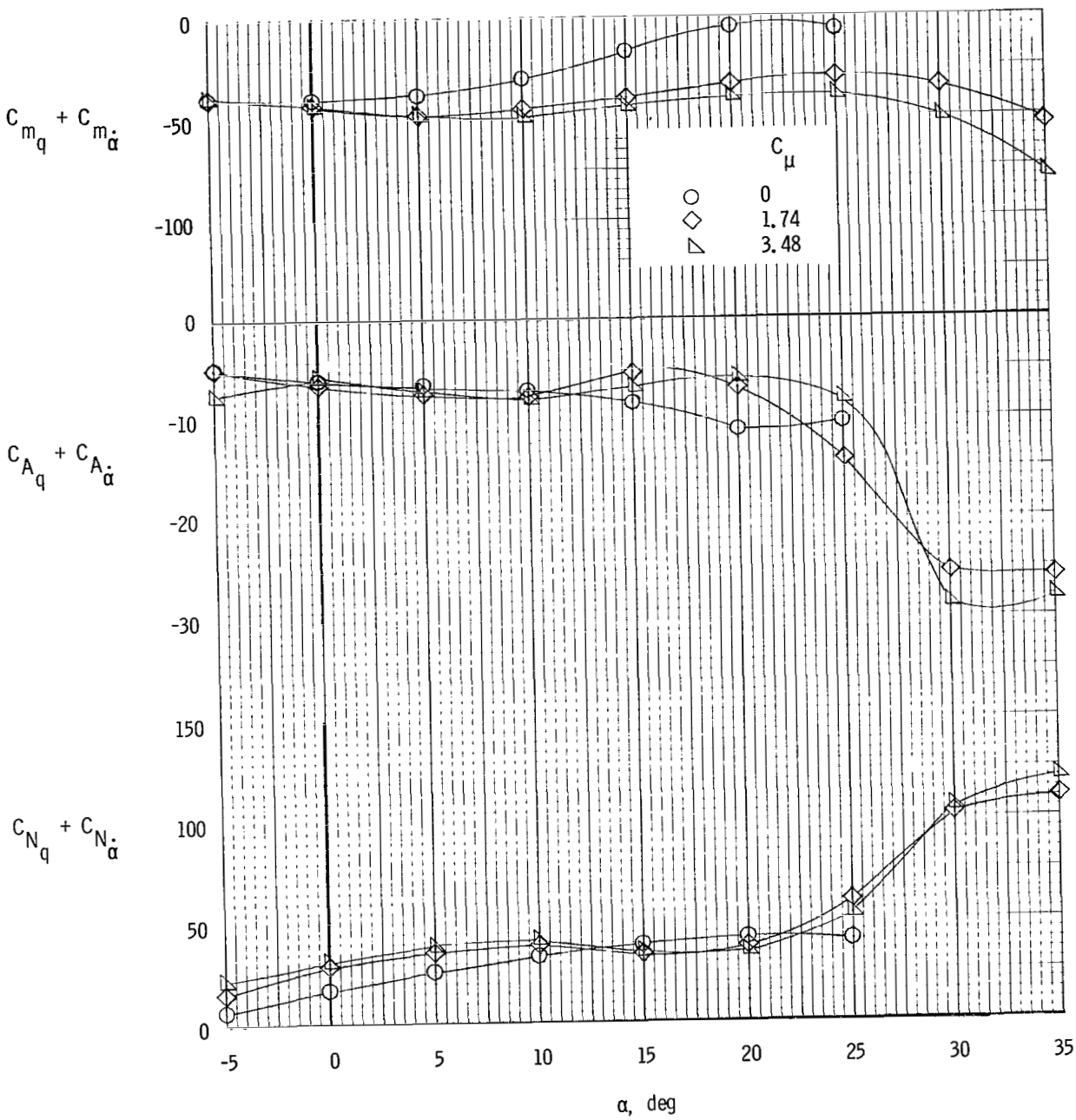

(d) Left outboard engine not operating; $C_{\mu,le} = 0.024$; $\delta_{f,L} = 70^{o}$, $\delta_{f,R} = 40^{o}$.

Figure 15.- Concluded.

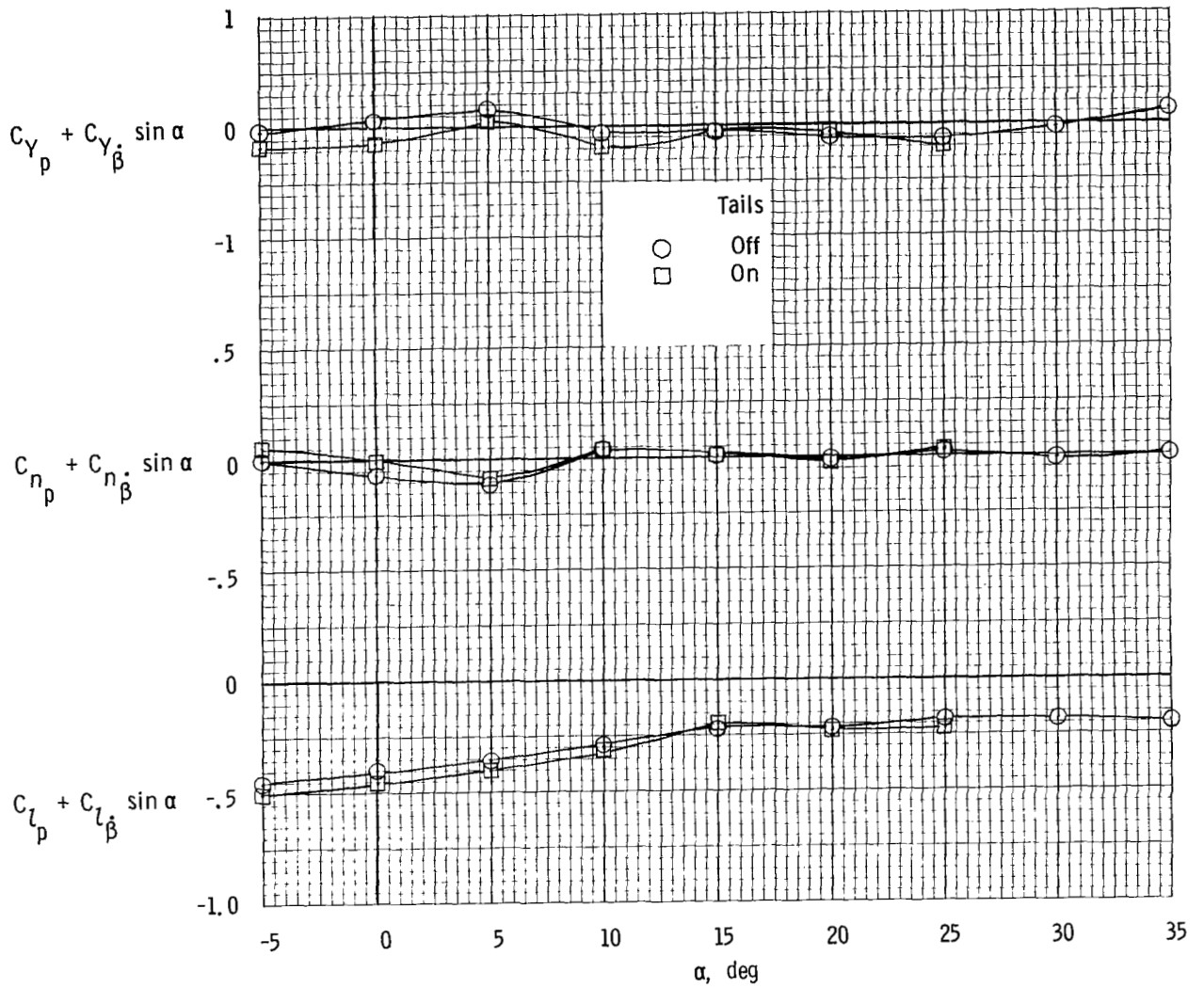

Figure 16.- Oscillatory rolling derivatives of clean configuration. $\delta_f = 0^o$; $k = 0.488$; $\delta_e = 0^o$; $i_t = 0^o$; $C_\mu = 0$.

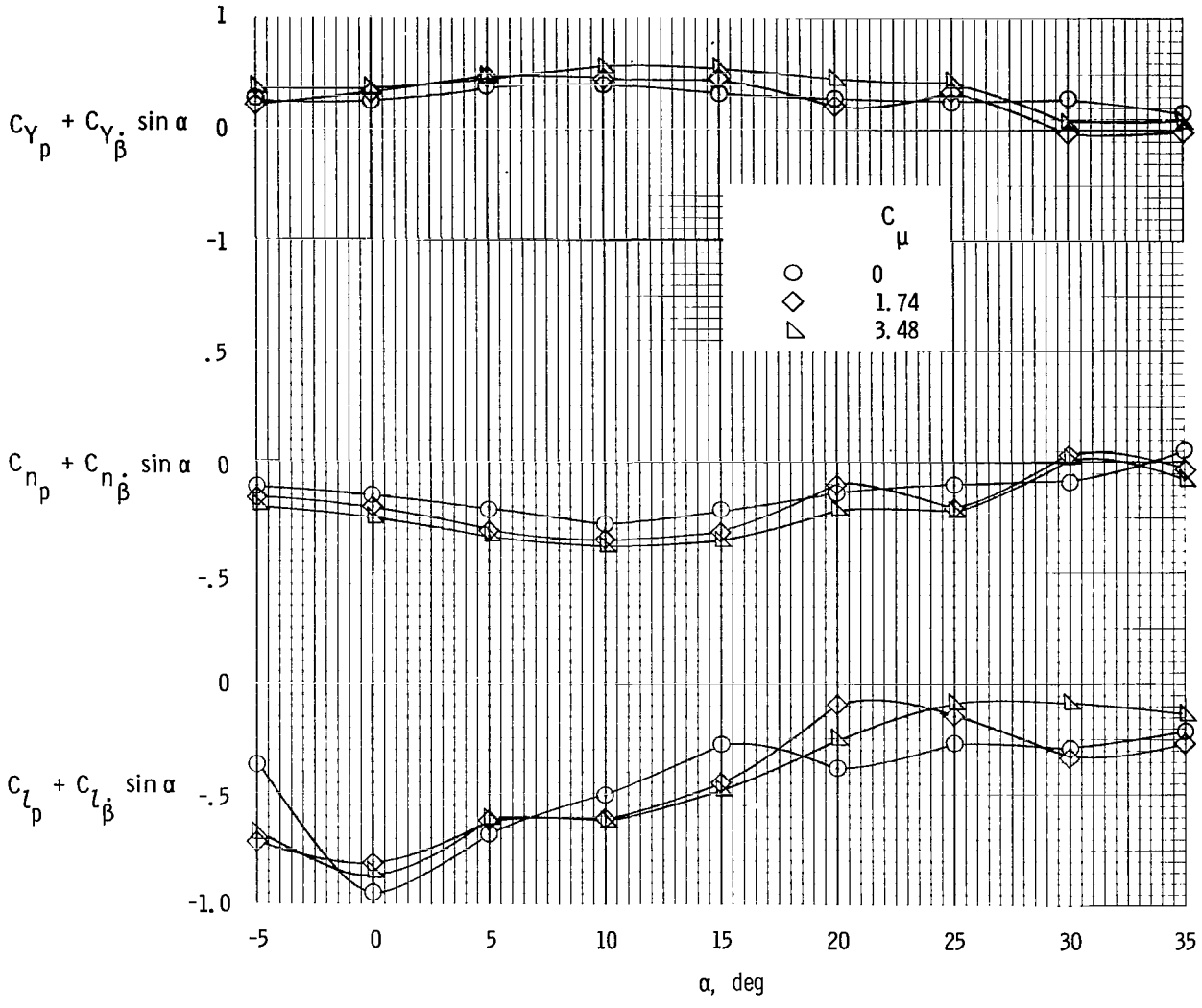

(a) Tails off.

Figure 17.- Oscillatory rolling derivatives of model with $\delta_f = 35^o$. $C_{\mu,le} = 0$; $k = 0.488$.

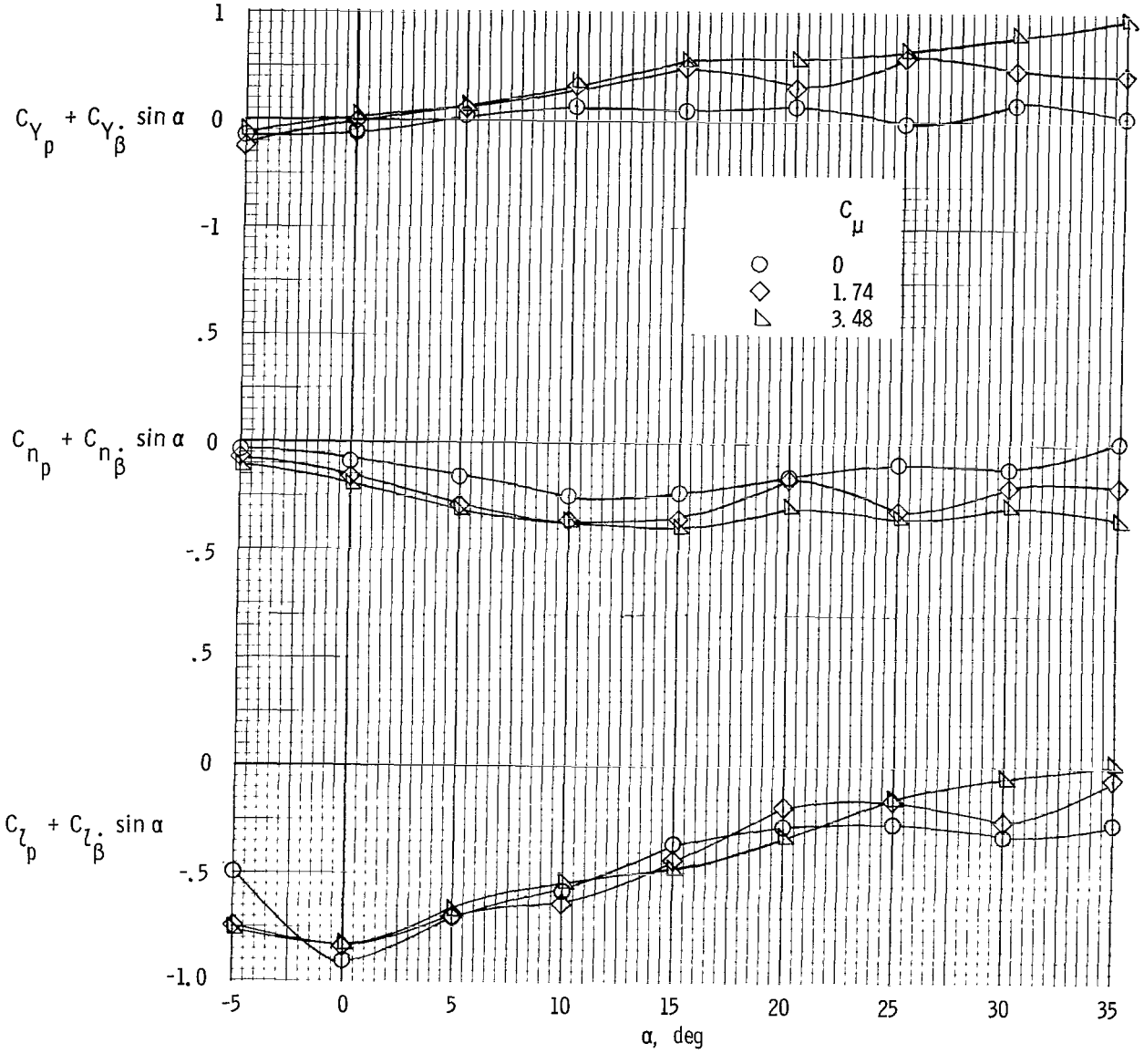

(b) Tails on; $\delta_e = -50^o$; $i_t = 0^o$.

Figure 17.- Concluded.

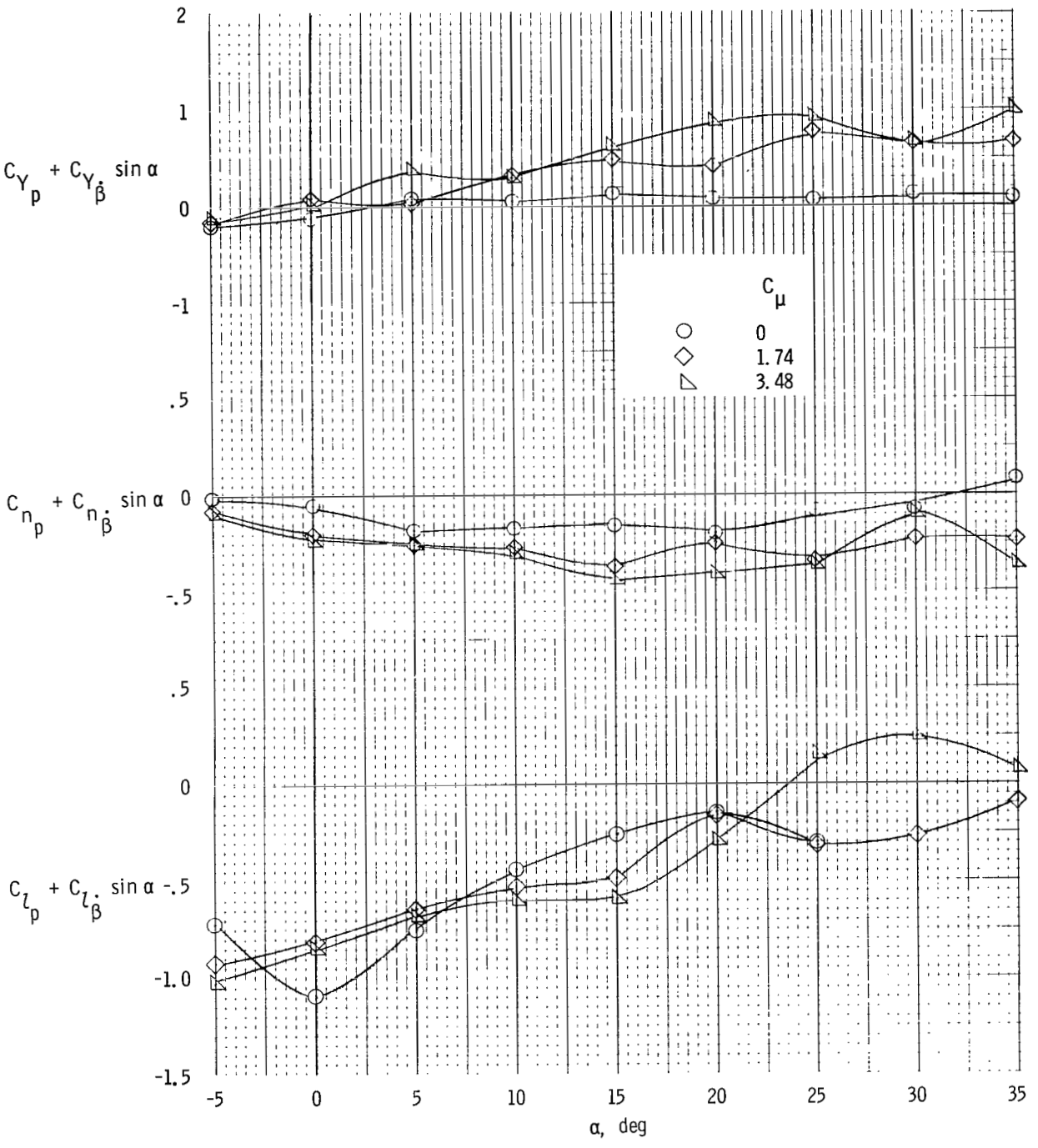

Figure 18.- Oscillatory rolling derivatives of model with $\delta_f = 50^o$. $C_{\mu,le} = 0$; $i_t = 0^o$; $\delta_e = -50^o$; $k = 0.488$.

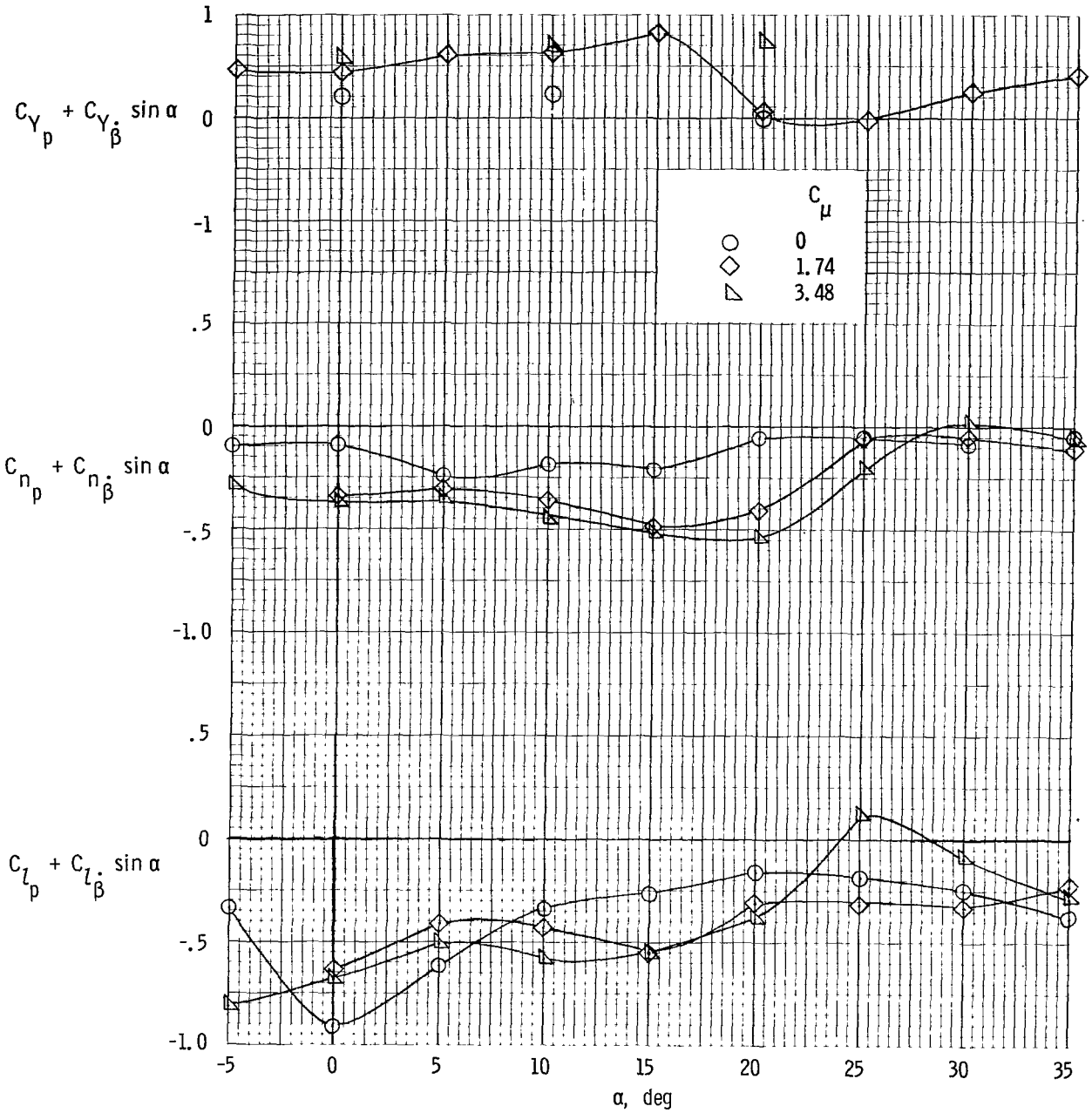

(a) $C_{\mu,le} = 0.$

Figure 19.- Oscillatory rolling derivatives of model with tails off and $\delta_f = 70^o$. k = 0.488.

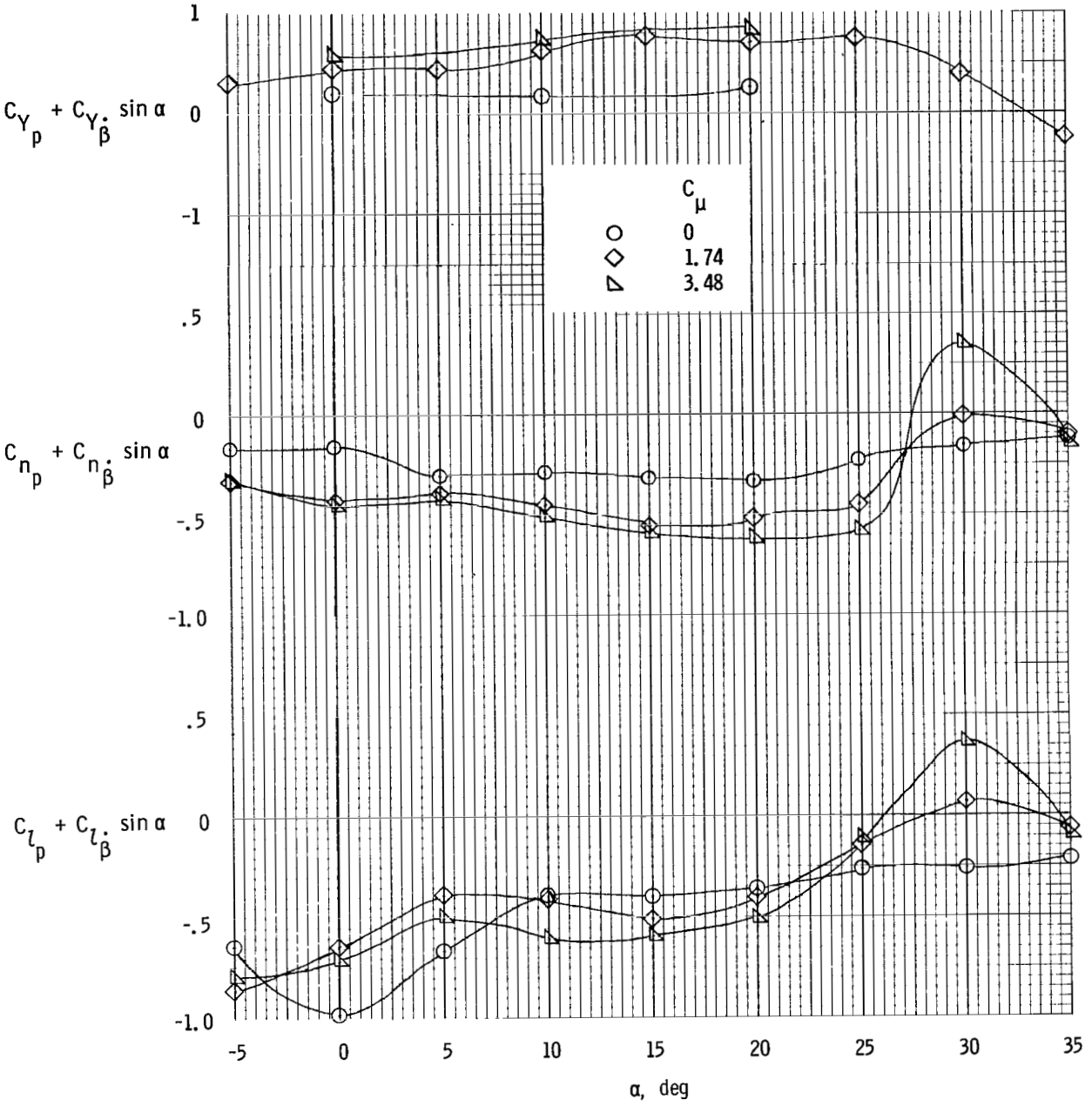

(b) $C_{\mu,le} = 0.024$.

Figure 19.- Concluded.

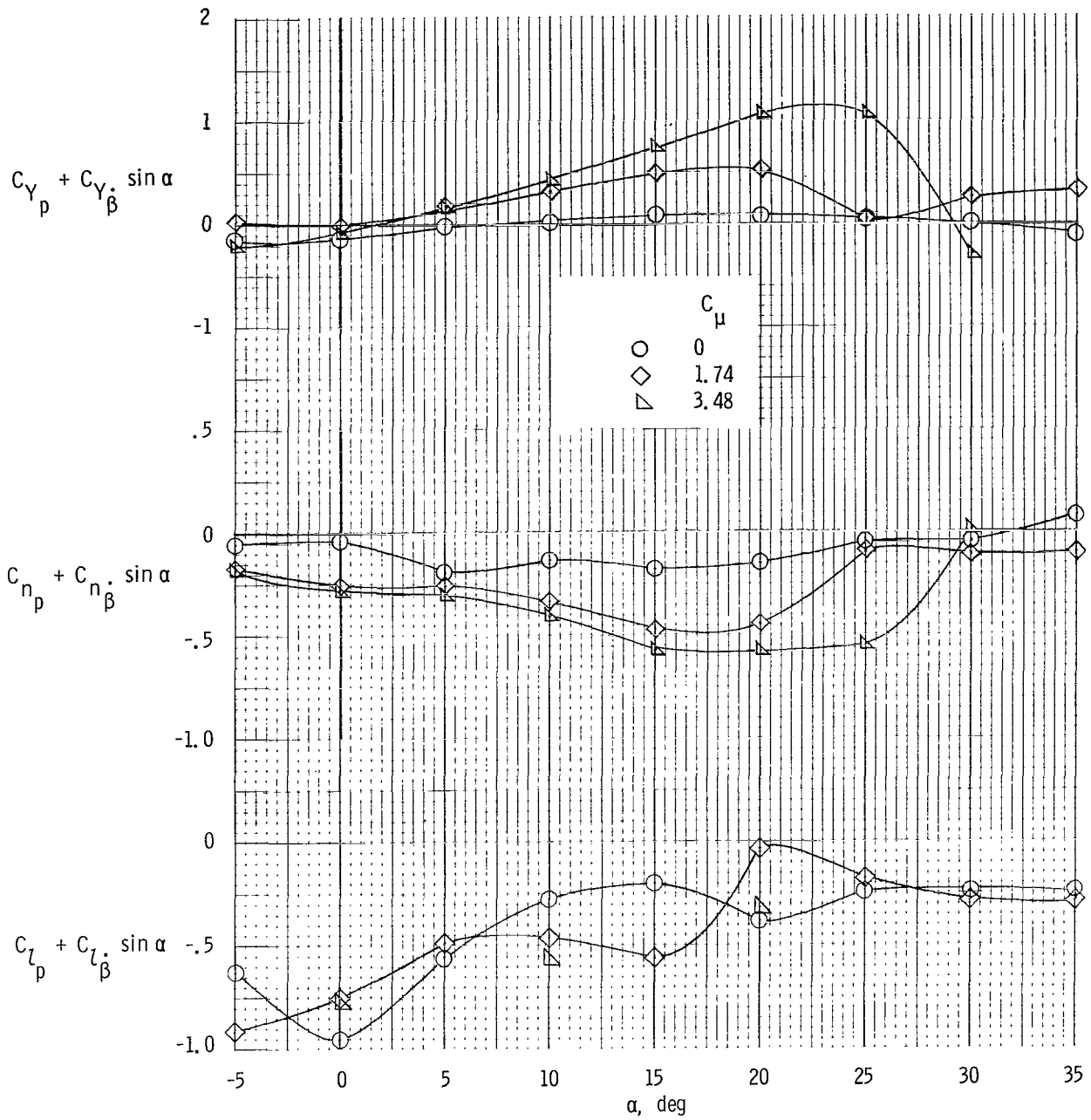

(a) k = 0.488; $C_{\mu,le} = 0$.

Figure 20.- Oscillatory rolling derivatives of model with tails on and $\delta_f = 70^o$. $i_t = 0^o$; $\delta_e = -50^o$.

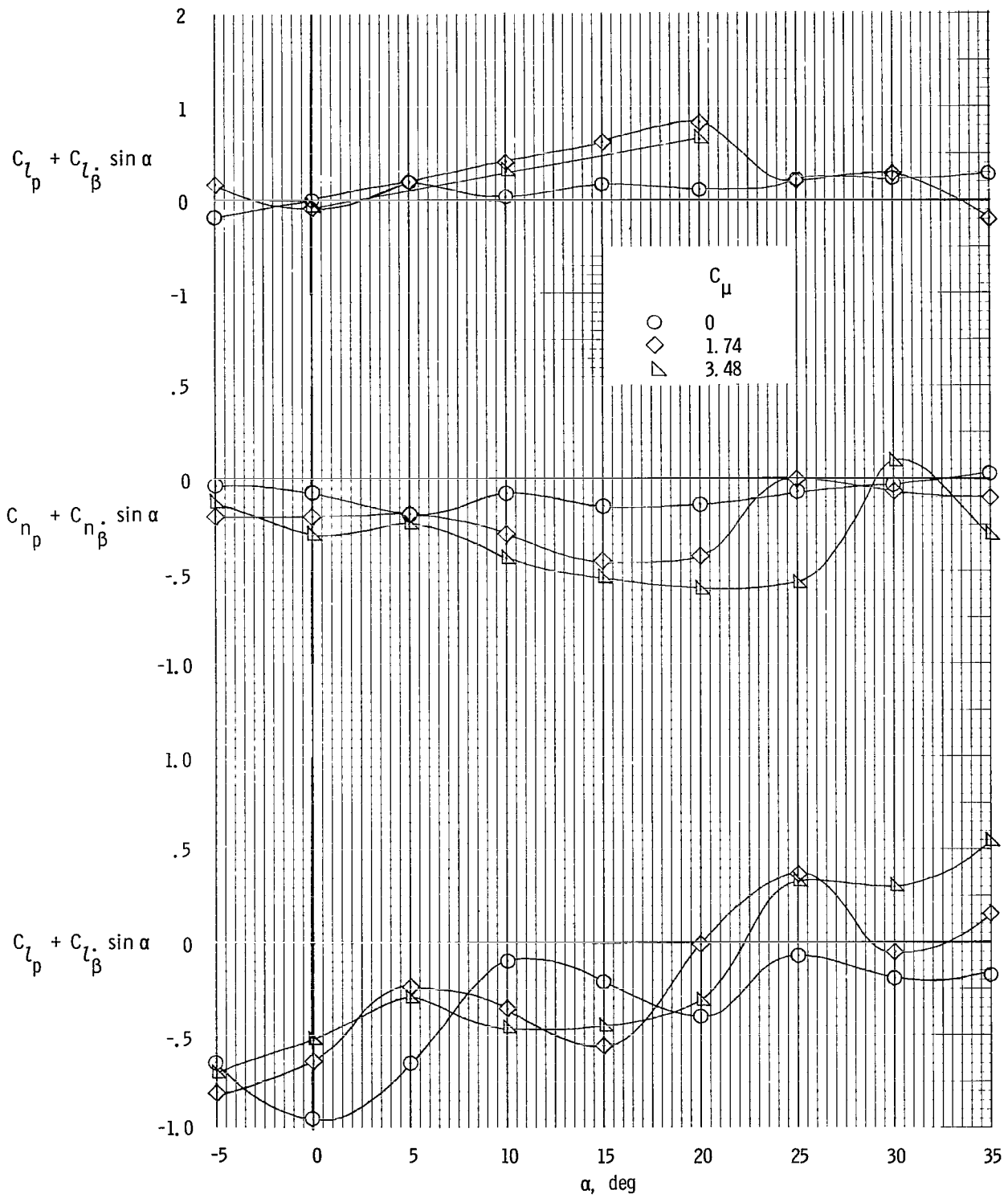

(b) k = 0.244; $C_{\mu,le} = 0$.

Figure 20.- Continued.

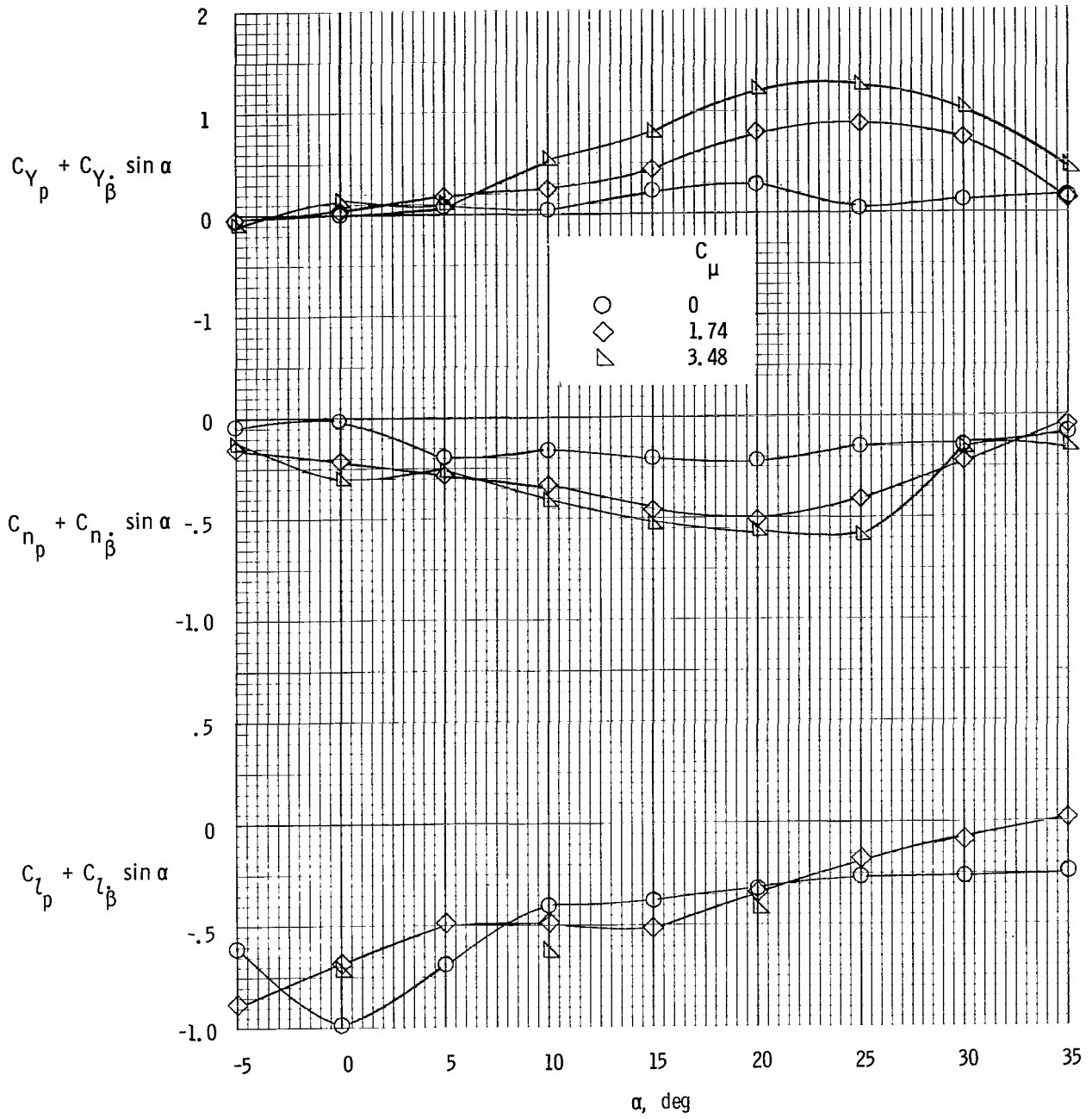

(c) k = 0.488; $C_{\mu,le} = 0.024$.

Figure 20.- Concluded.

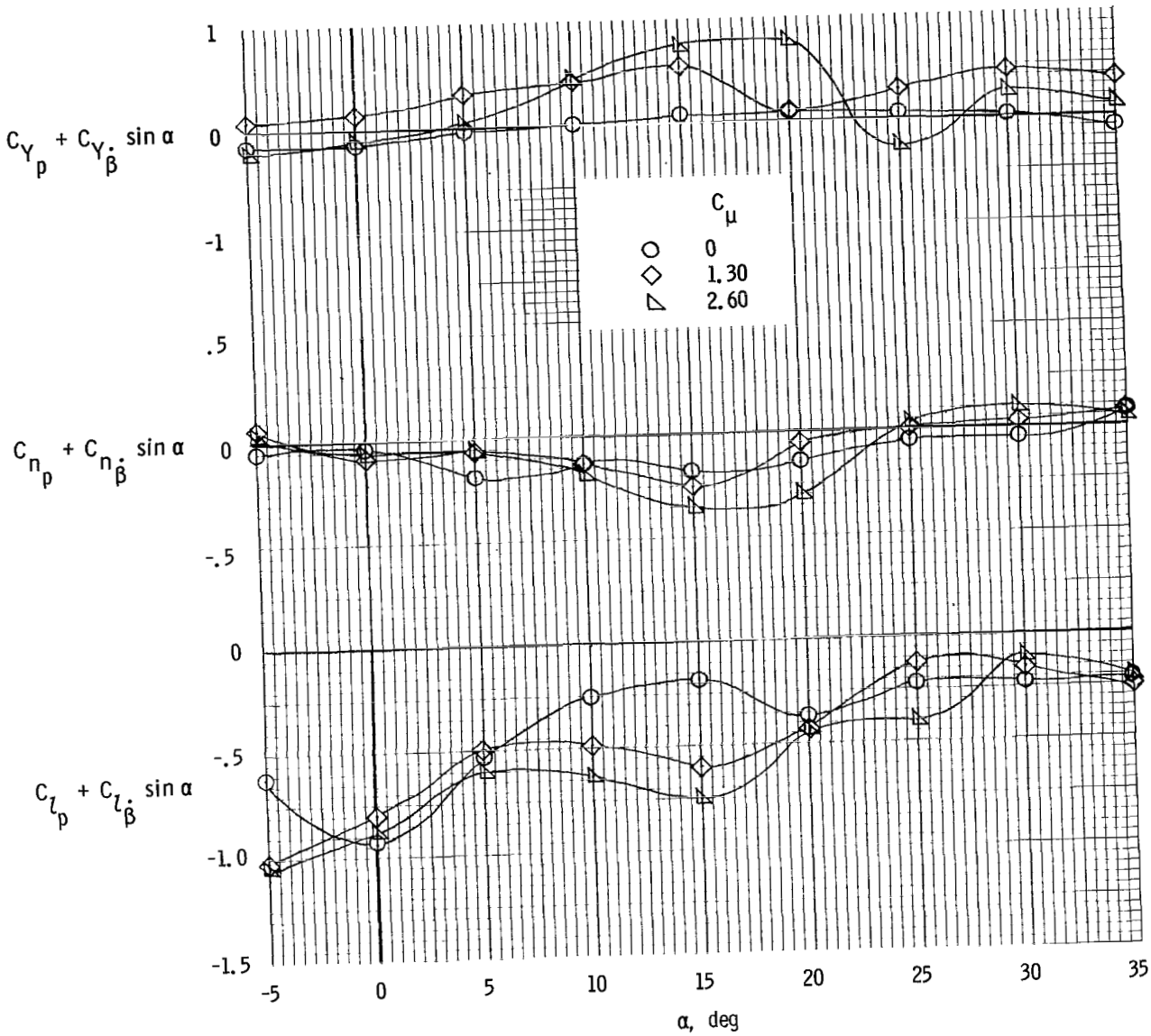

(a) Left outboard engine not operating; $C_{\mu,le} = 0$; $\delta_f = 70^o$.

Figure 21.- Engine-out oscillatory rolling derivatives. $i_t = 0^o$; $\delta_e = -50^o$; $k = 0.488$.

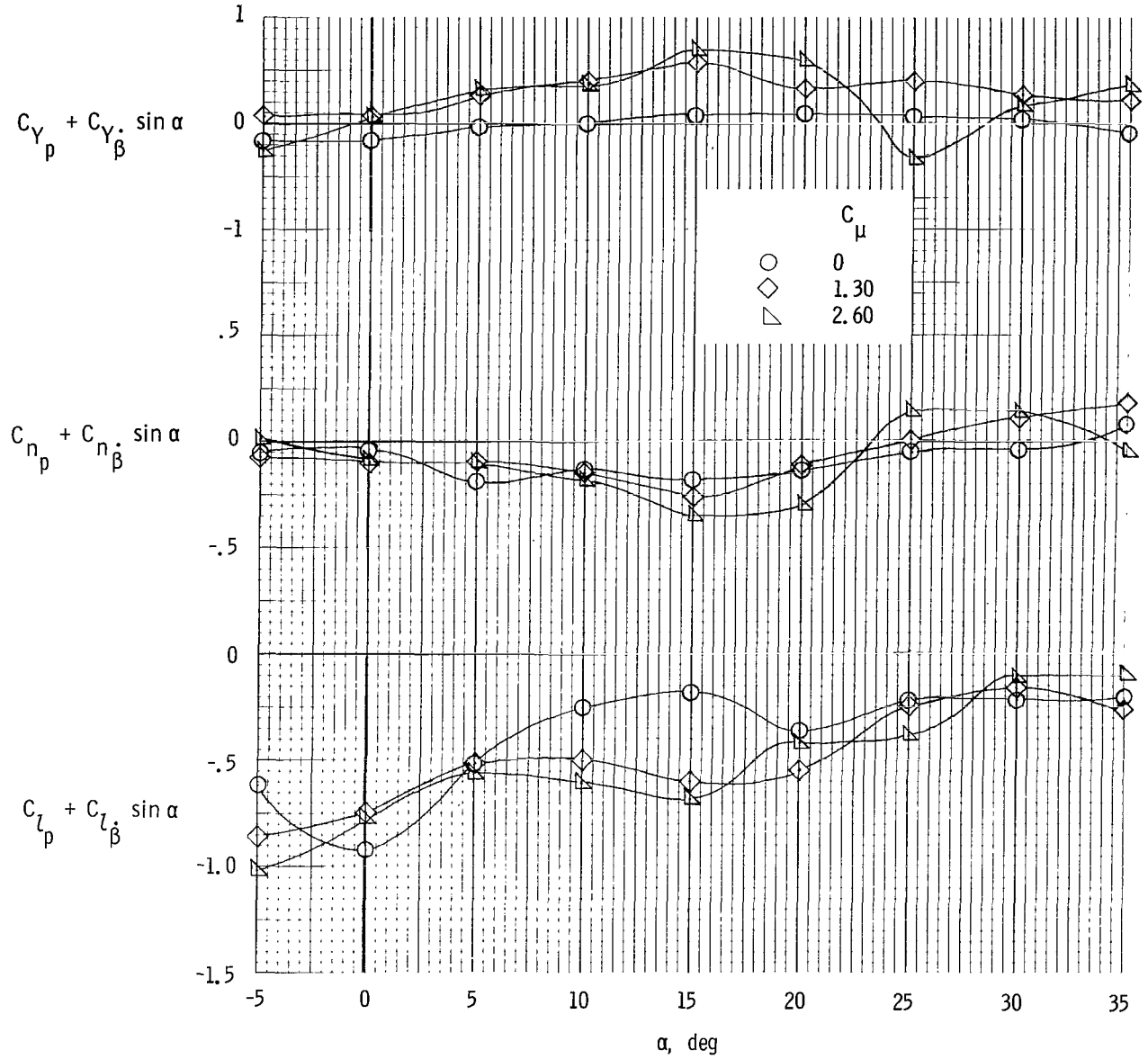

(b) Left inboard engine not operating; $C_{\mu,le} = 0$; $\delta_f = 70^o$.

Figure 21.- Continued.

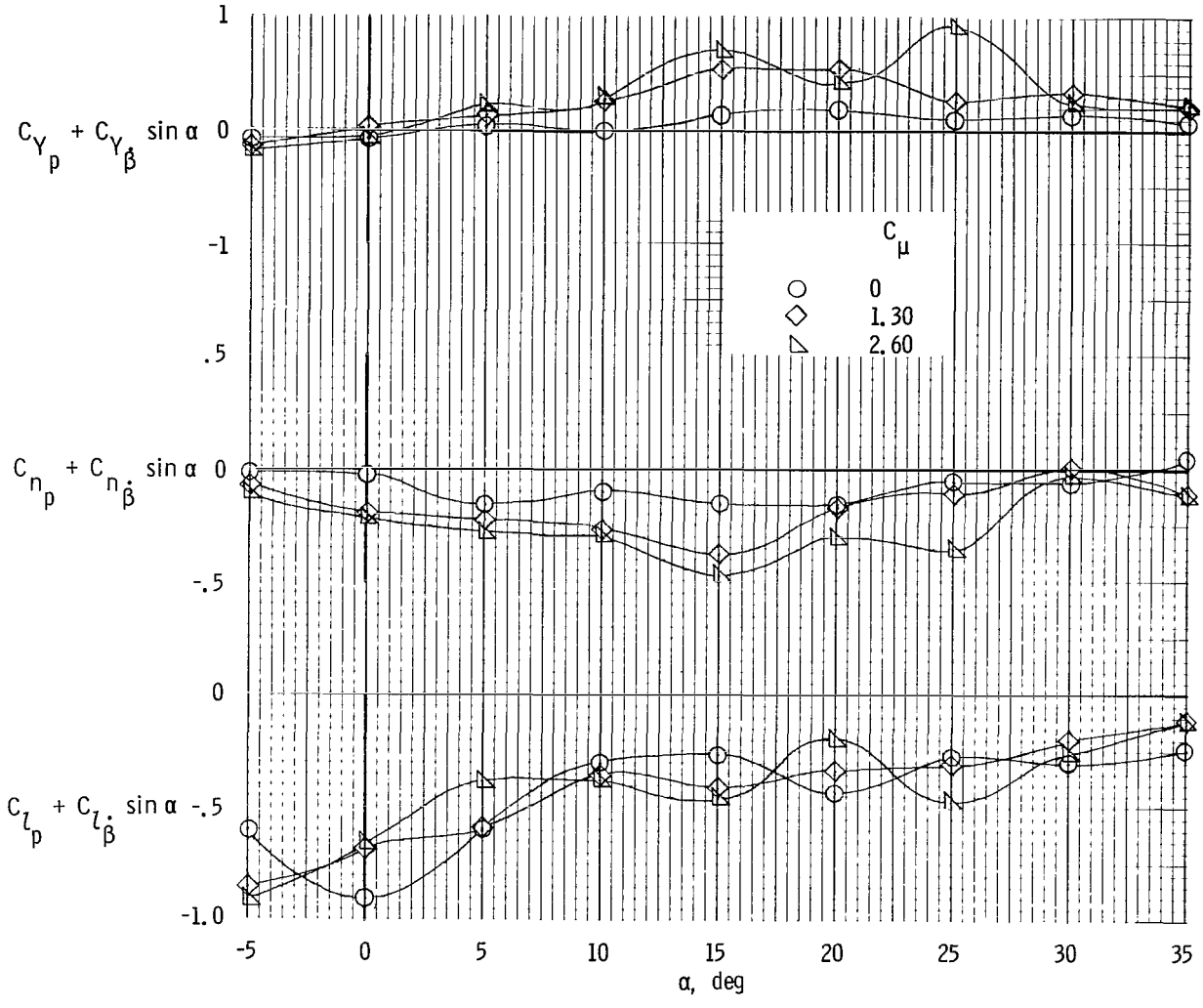

(c) Left outboard engine not operating; $C_{\mu,le} = 0$; $\delta_{f,L} = 70^o$, $\delta_{f,R} = 40^o$.

Figure 21.- Continued.

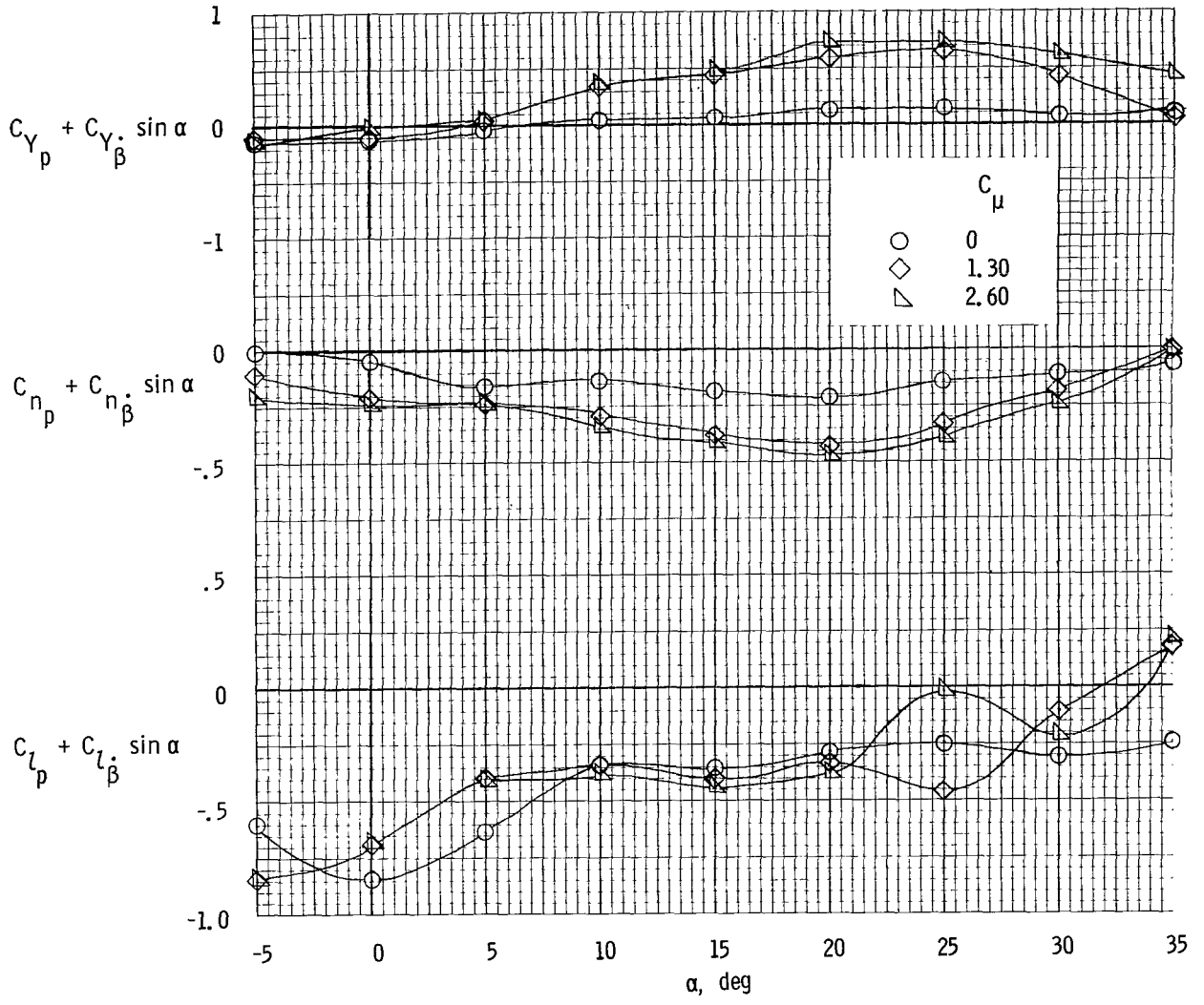

(d) Left outboard engine not operating; $C_{\mu,le} = 0.024$; $\delta_{f,L} = 70^o$, $\delta_{f,R} = 40^o$.

Figure 21.- Concluded.

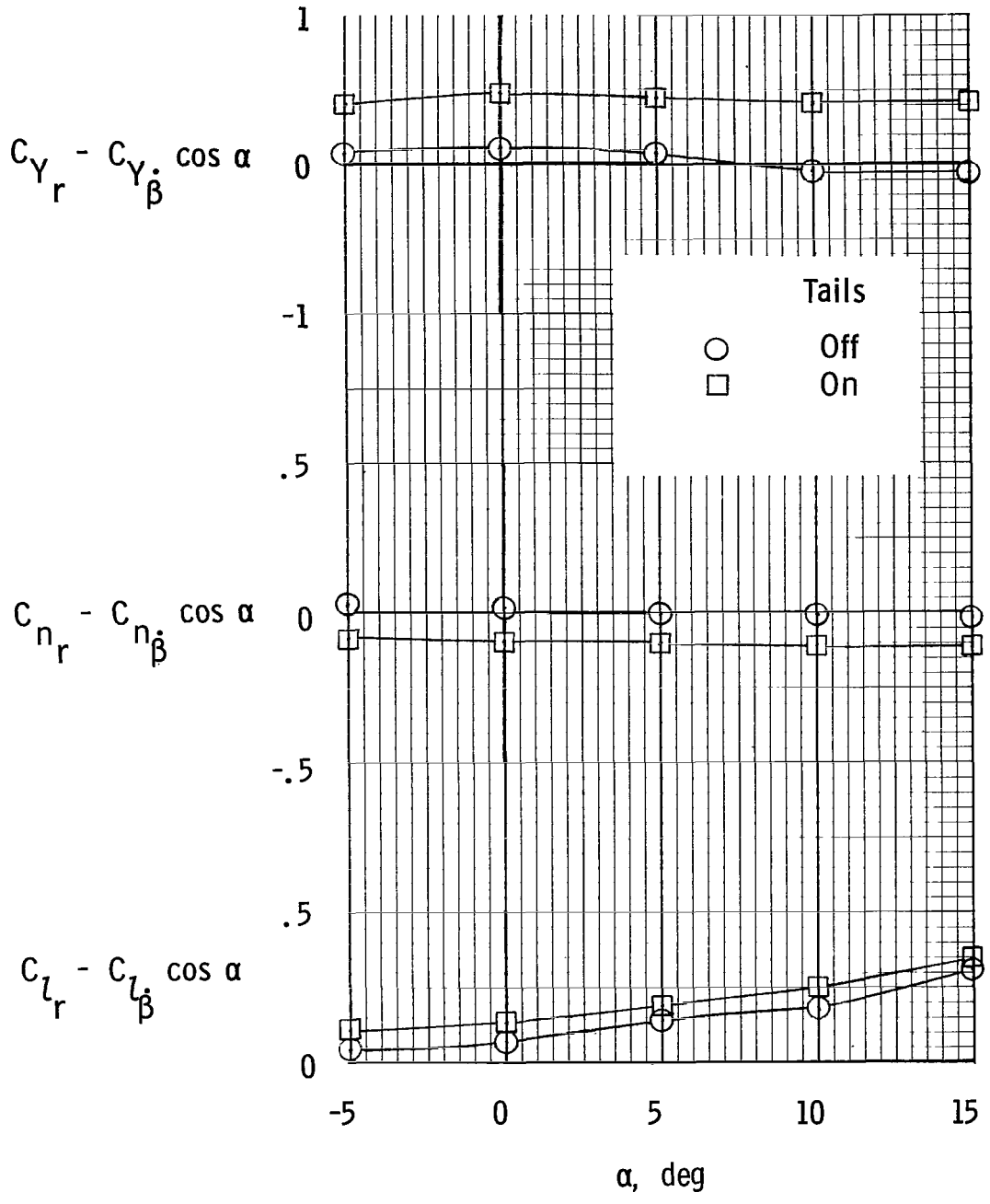

Figure 22.- Oscillatory yawing derivatives of clean configuration. $\delta_f = 0^o$; $i_t = 0^o$; $\delta_e = 0^o$; $k = 0.488$; $C_\mu = 0$.

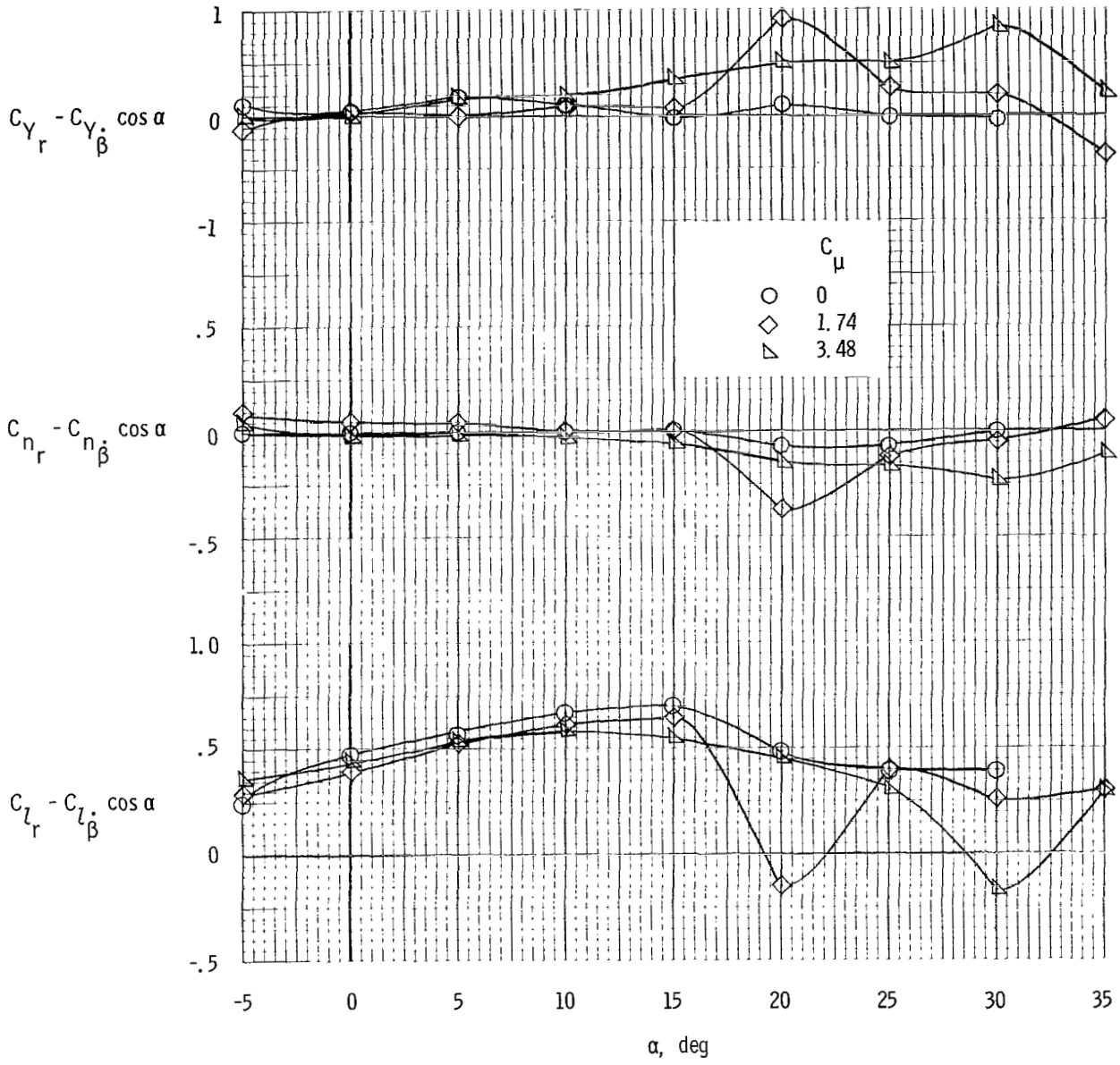

(a) $C_{\mu,le} = 0$.

Figure 23.- Oscillatory yawing derivatives of model with tails off and $\delta_f = 35^o$. k = 0.488.

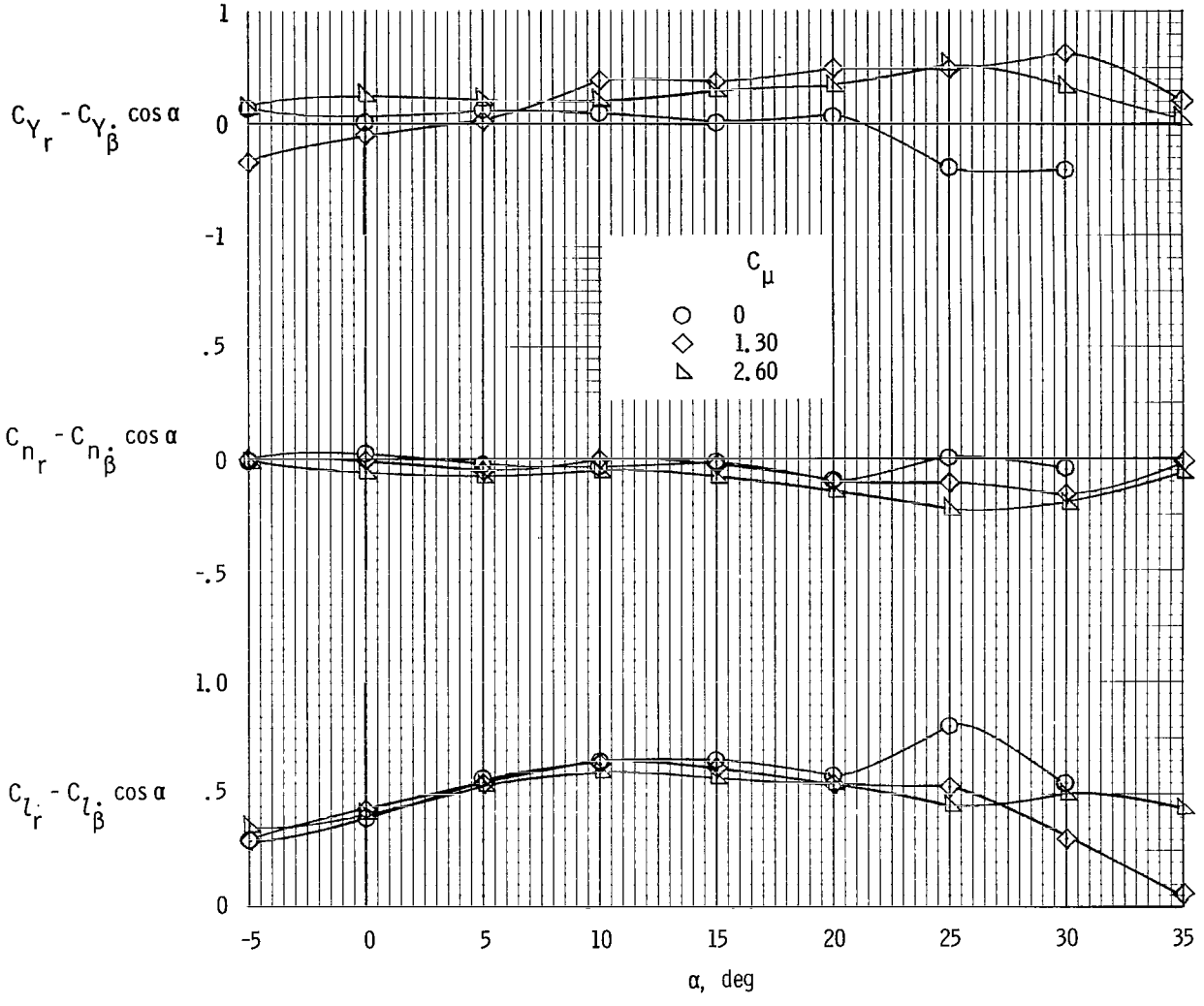

(b) $C_{\mu,le} = 0.024$.

Figure 23.- Concluded.

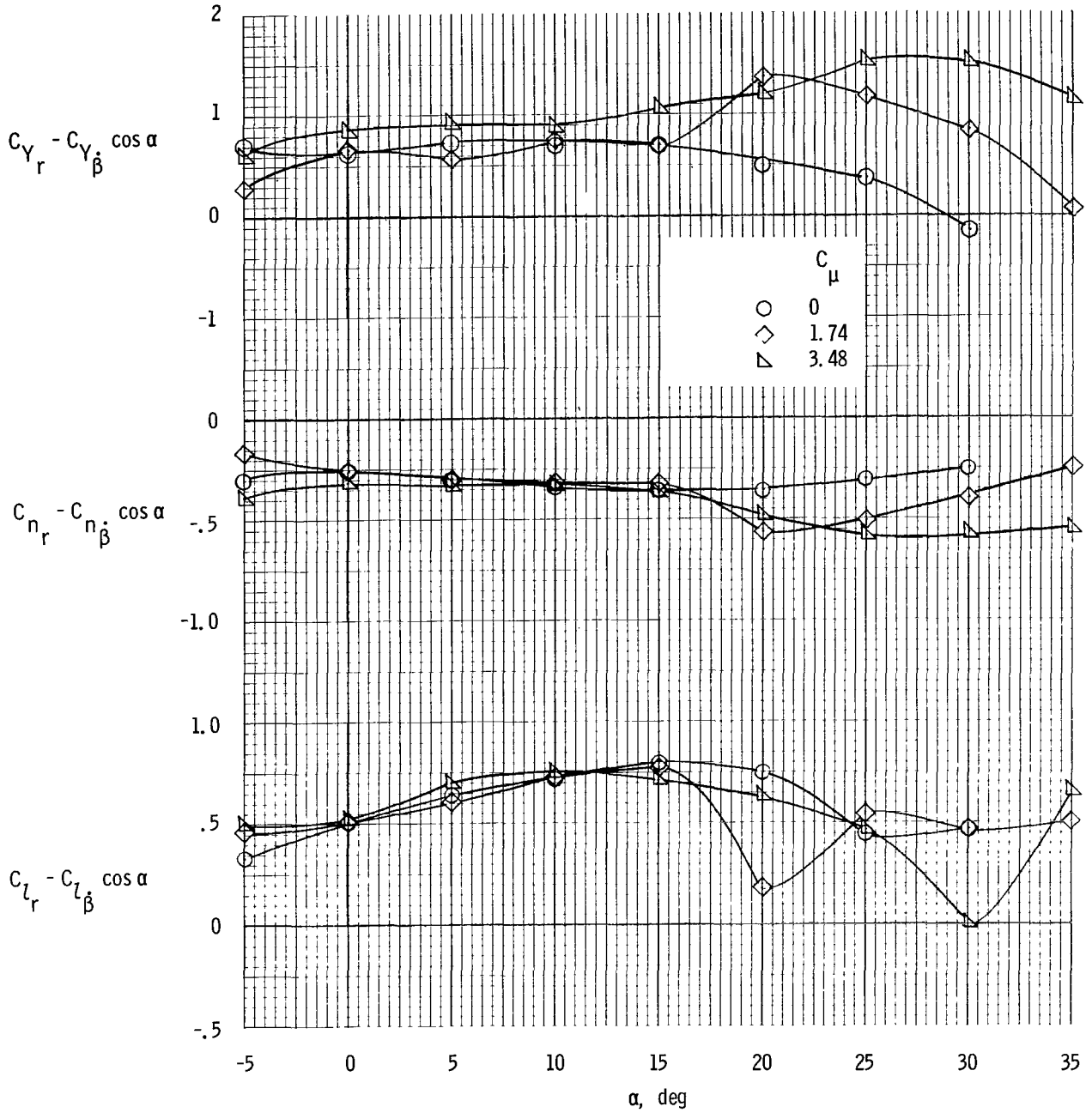

(a) k = 0.488; $C_{\mu,le} = 0$.

Figure 24.- Oscillatory yawing derivatives of model with tails on and $\delta_f = 35^o$. $i_t = 0^o$; $\delta_e = -50^o$.

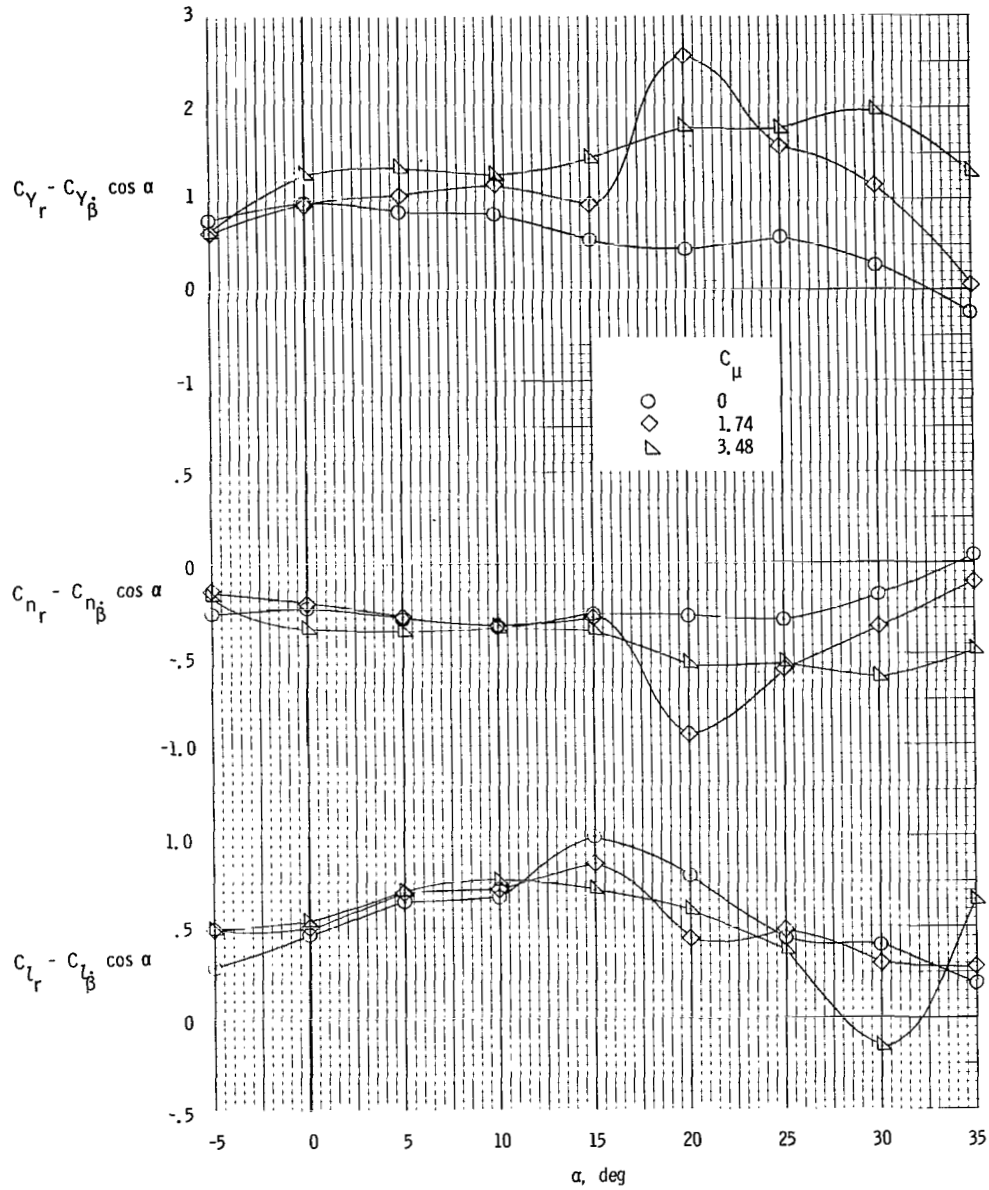

(b) $k = 0.244$; $C_{\mu,le} = 0$.

Figure 24.- Continued.

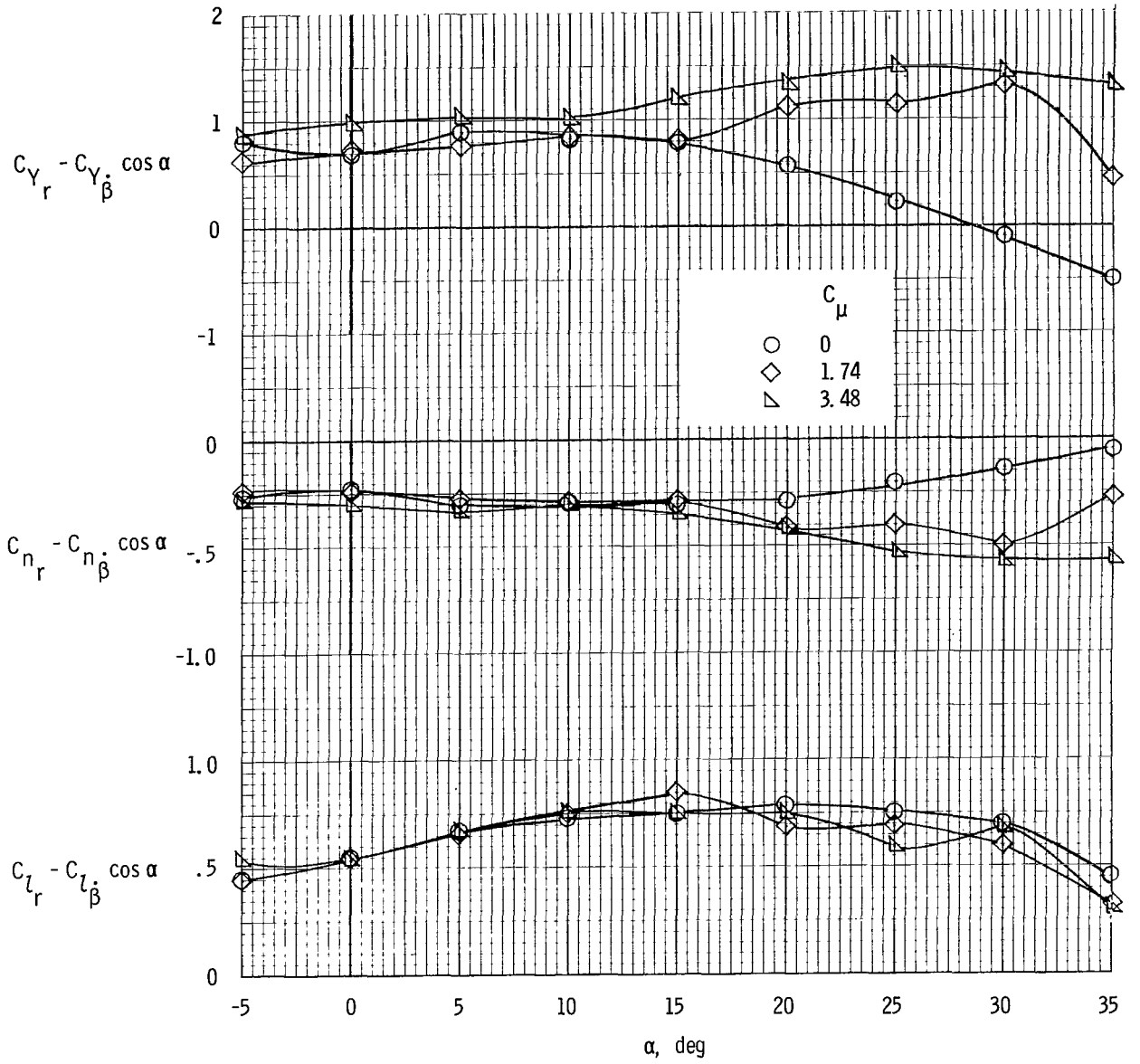

(c) k = 0.488; $C_{\mu,le} = 0.024$.

Figure 24.- Concluded.

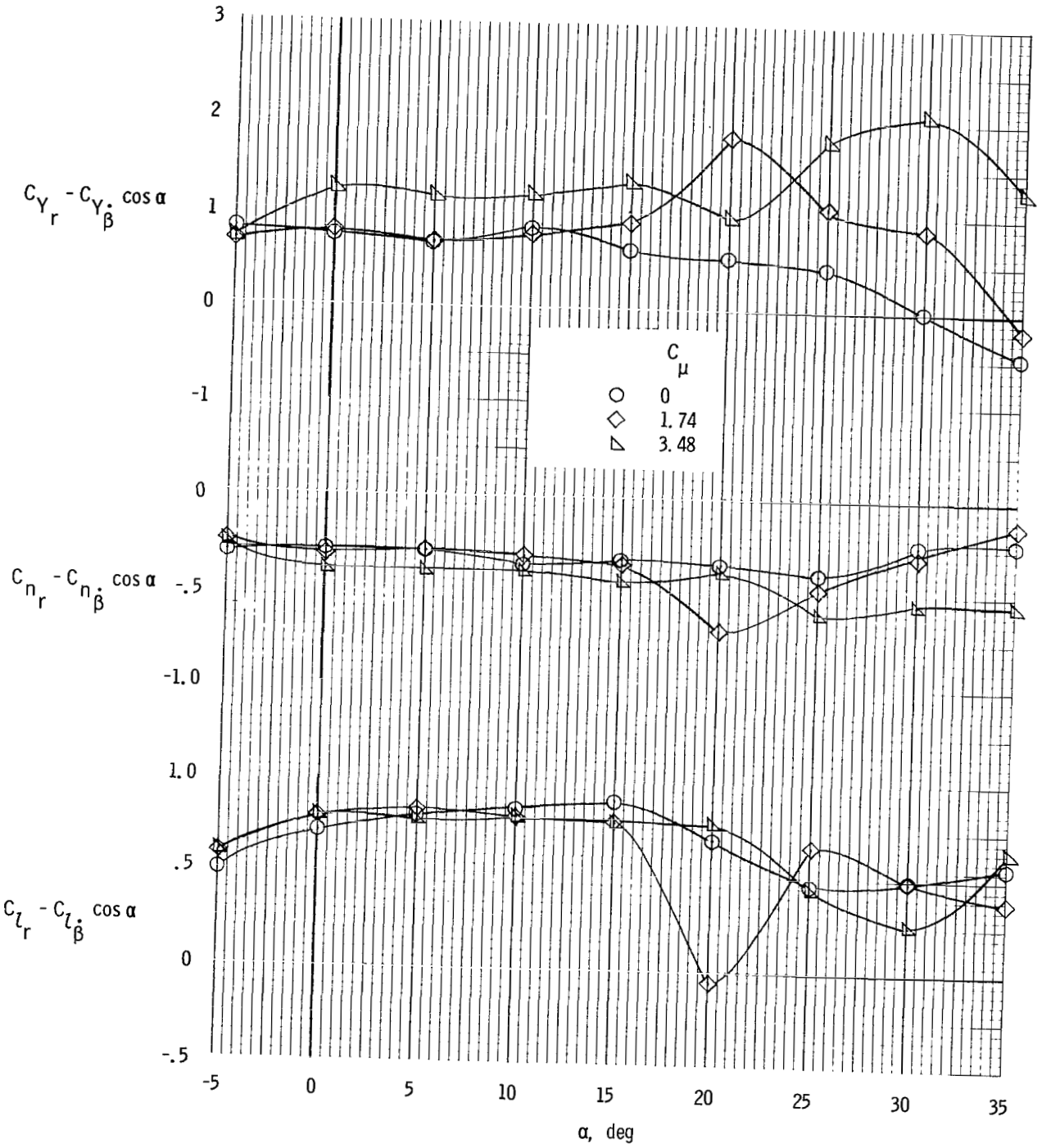

(a) k = 0.488.

Figure 25.- Oscillatory yawing derivatives of model with $\delta_f = 50^o$. $i_t = 0^o$; $\delta_e = -50^o$; $C_{\mu,le} = 0$.

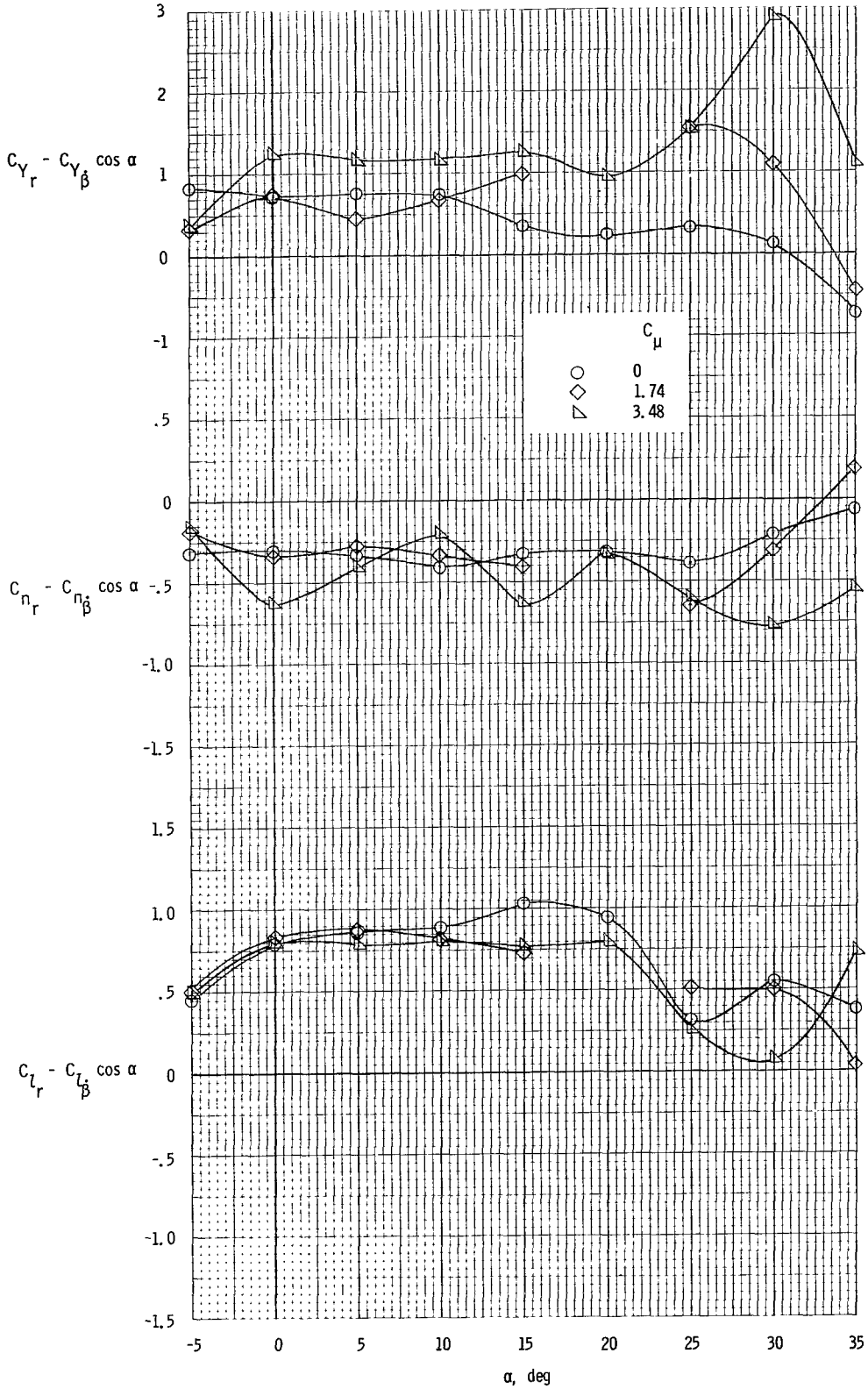

(b) k = 0.244.

Figure 25.- Concluded.

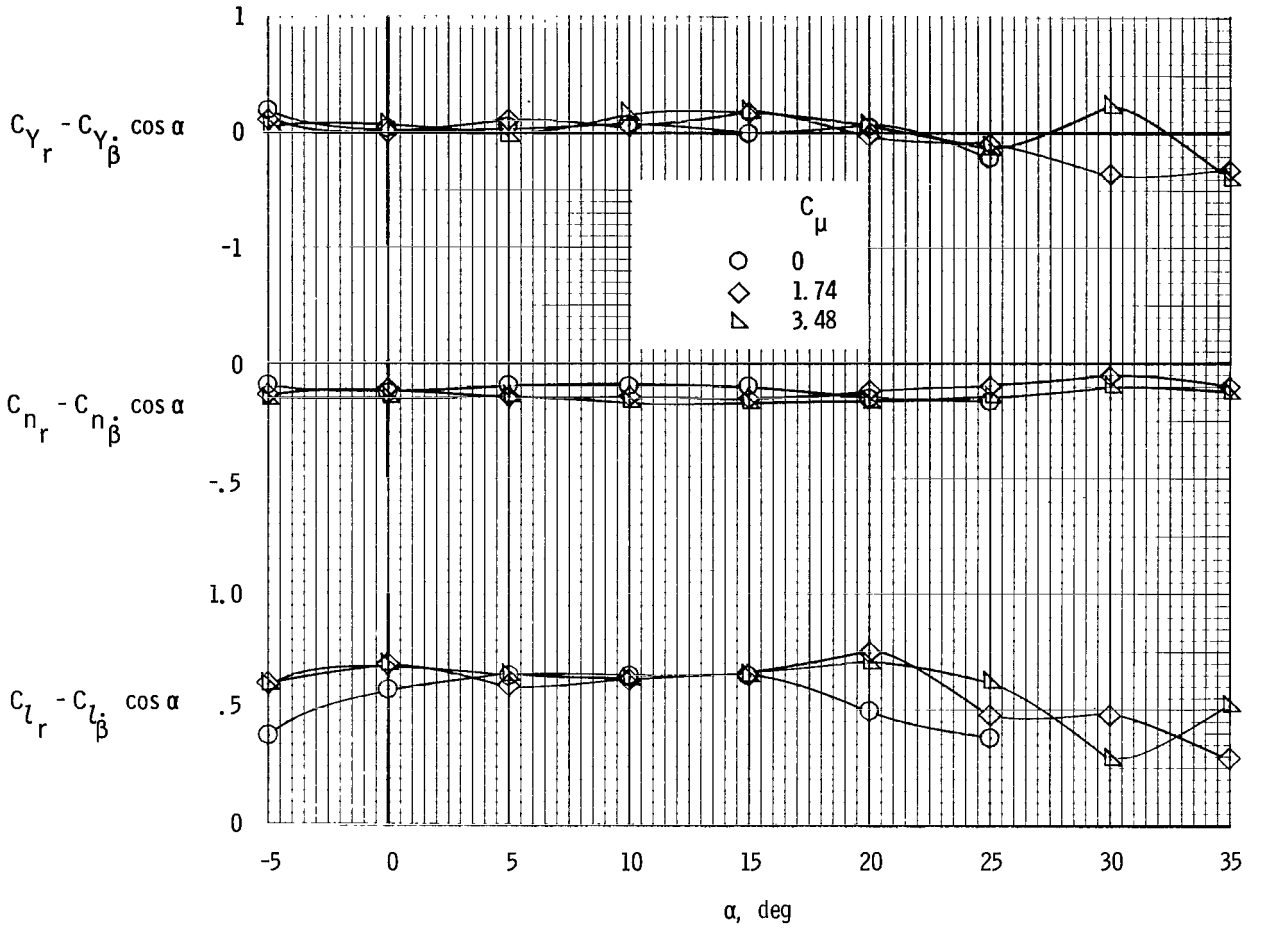

(a) $C_{\mu,le} = 0.$

Figure 26.- Oscillatory yawing derivatives of model with tails off and $\delta_f = 70^o$. k = 0.488.

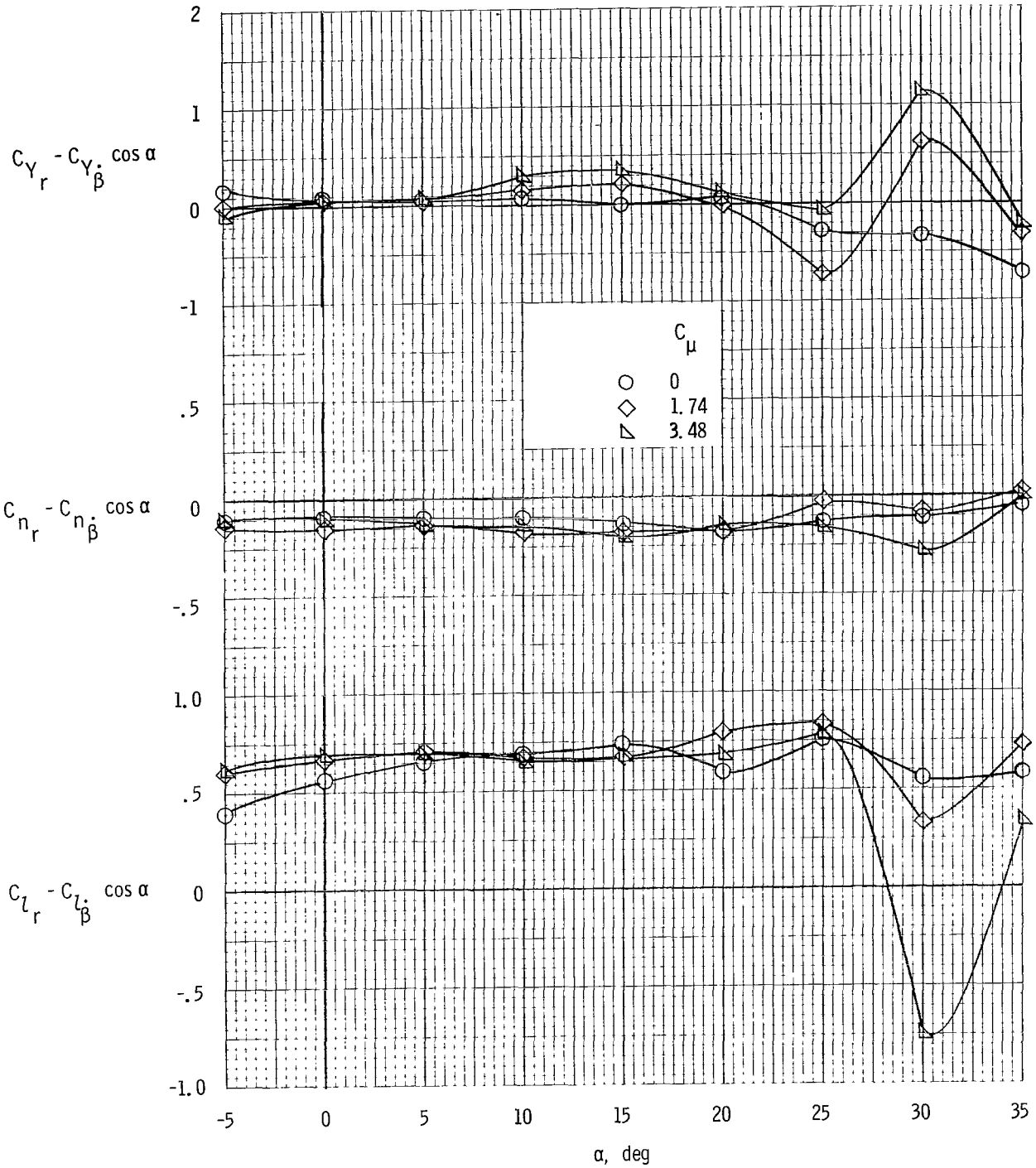

(b) $C_{\mu,le} = 0.024$.

Figure 26.- Concluded.

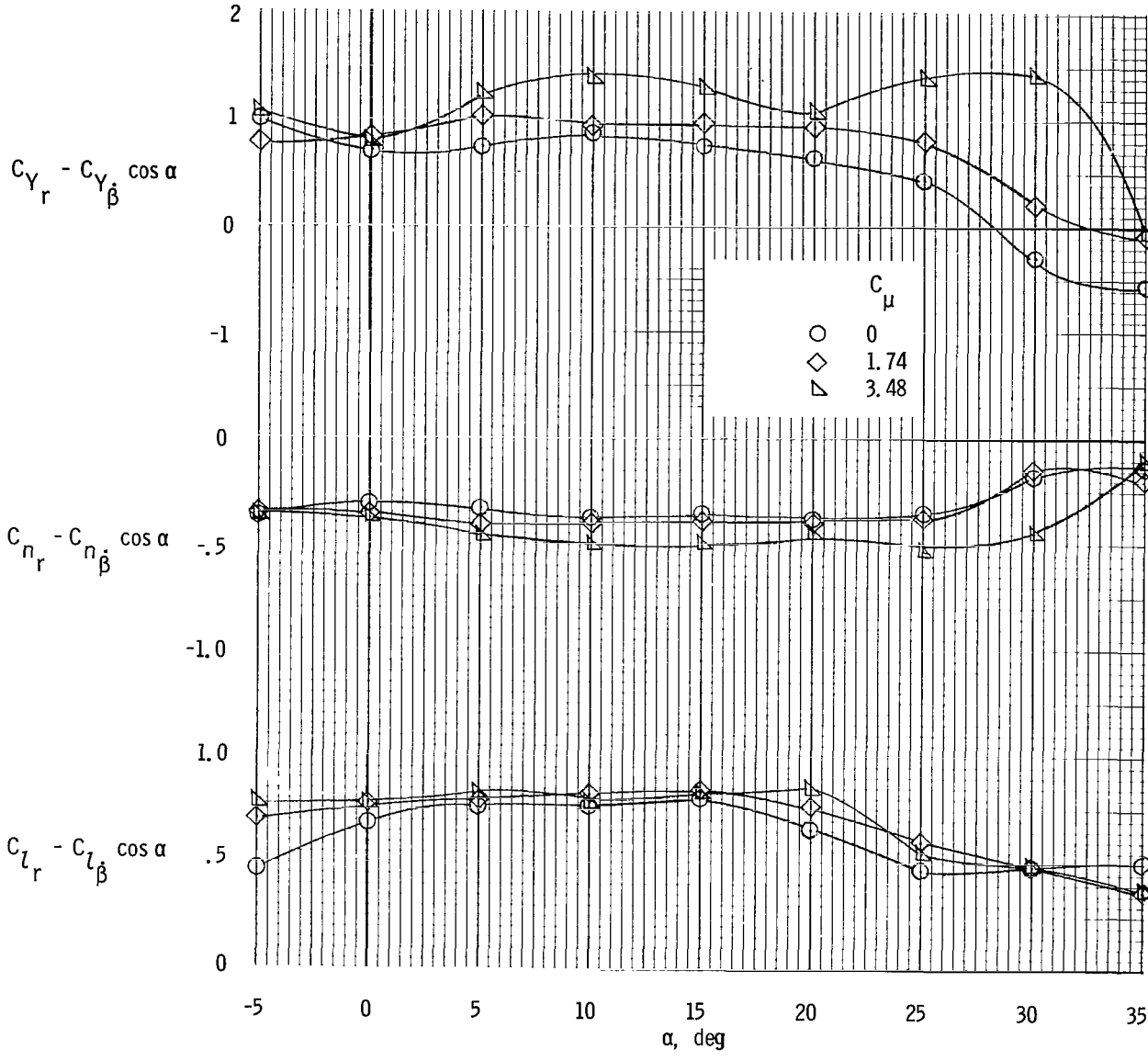

(a) k = 0.488; $C_{\mu,le} = 0$.

Figure 27.- Oscillatory yawing derivatives of model with tails on and $\delta_f = 70^o$. $i_t = 0^o$, $\delta_e = -50^o$.

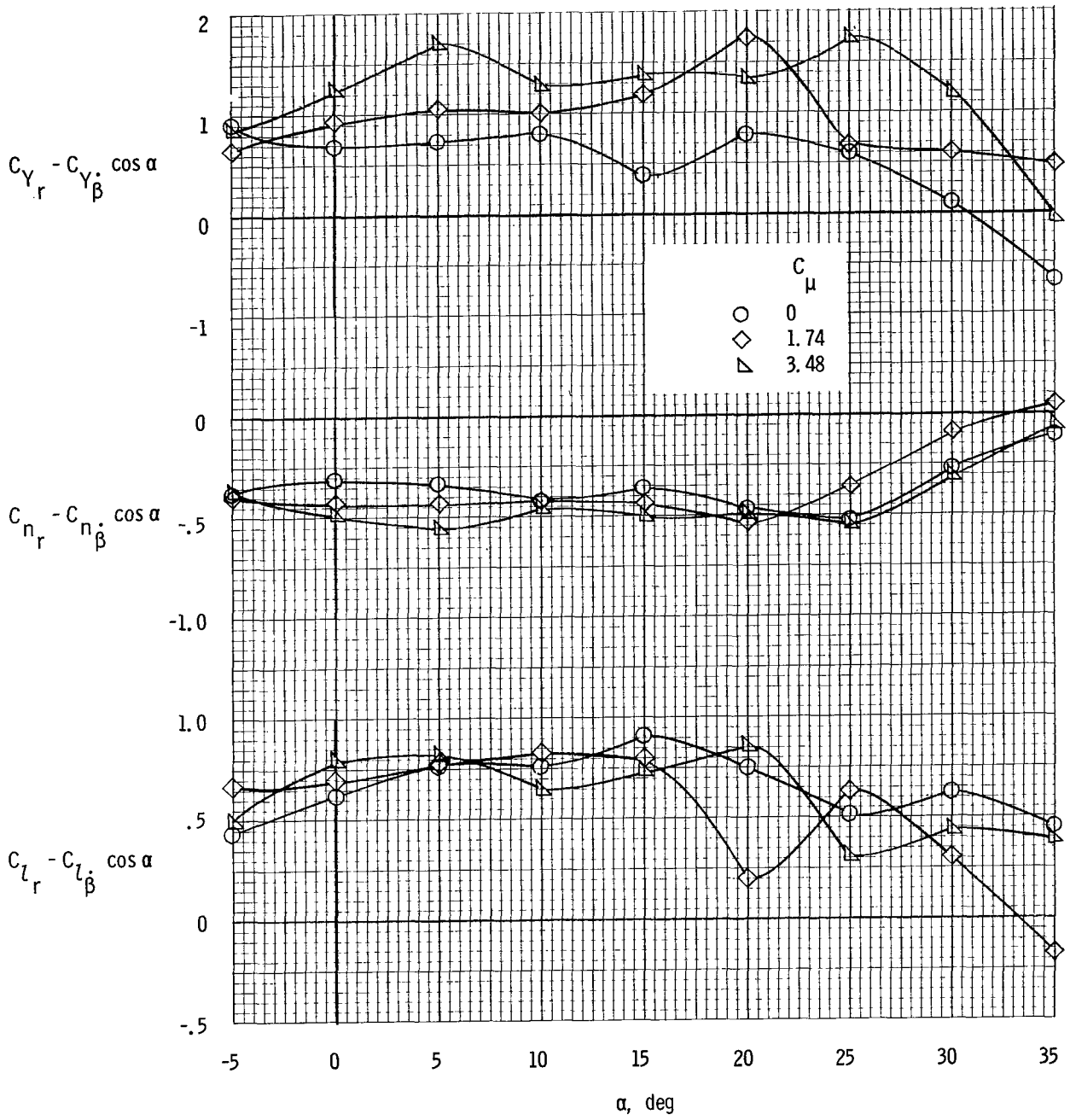

(b) k = 0.244; $C_{\mu,le} = 0.$

Figure 27.- Continued.

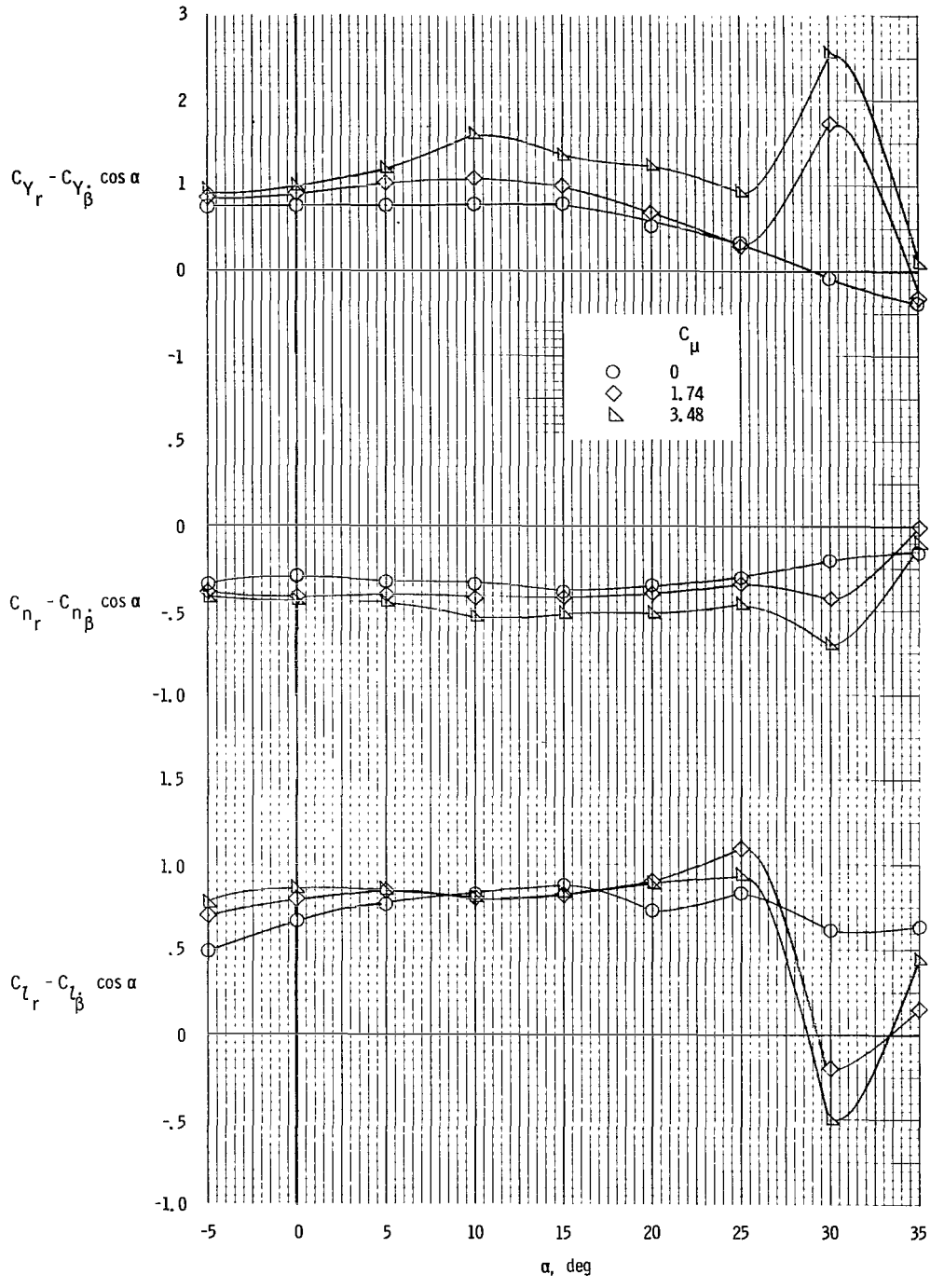

(c) k = 0.488; $C_{\mu,le} = 0.024$.

Figure 27.- Concluded.

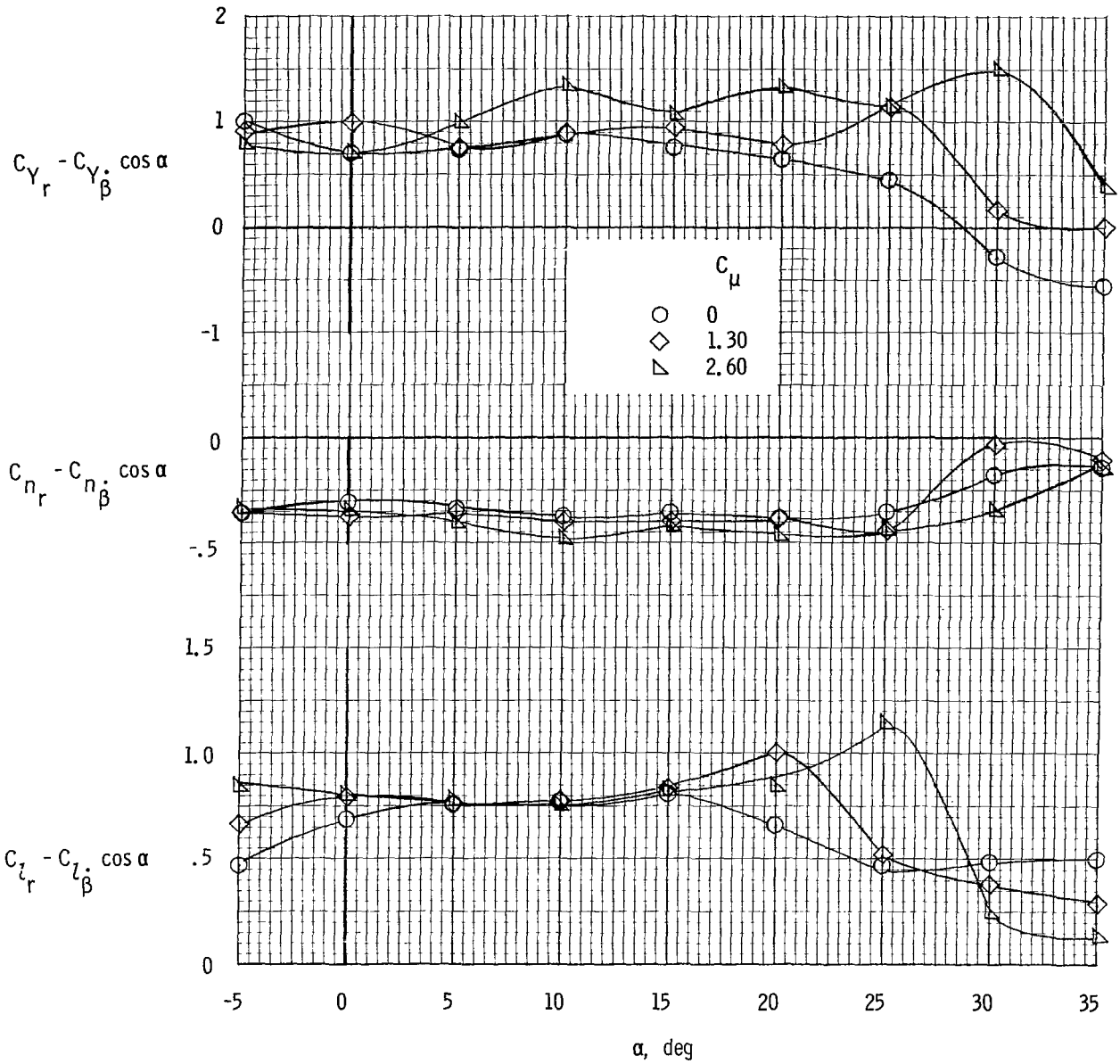

(a) Left outboard engine not operating; $C_{\mu,le} = 0$; $\delta_f = 70^o$.

Figure 28.- Engine-out oscillatory yawing derivatives. $i_t = 0^o$; $\delta_e = -50^o$; $k = 0.488$.

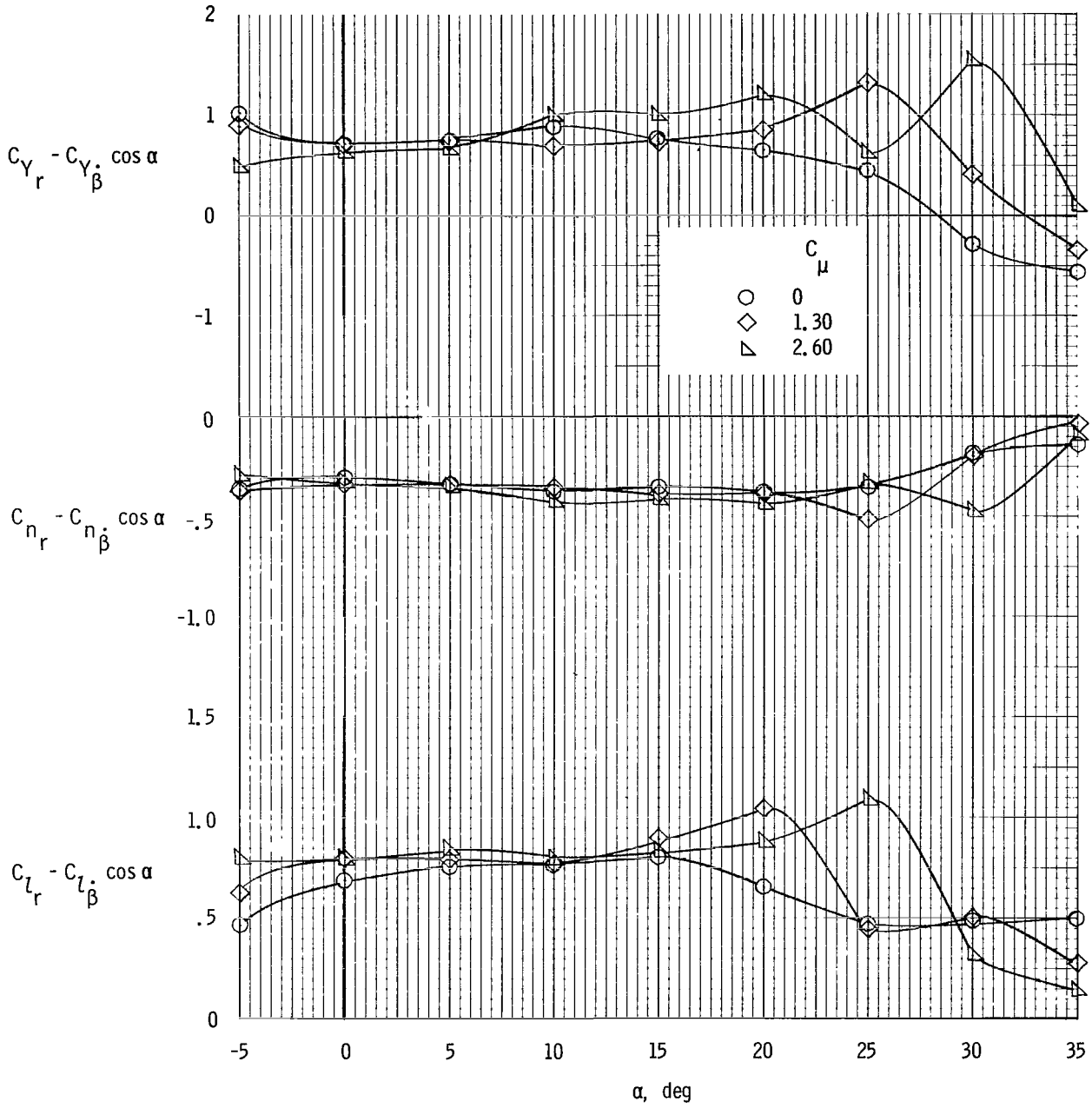

(b) Left inboard engine not operating; $C_{\mu,le} = 0$; $\delta_f = 70^o$.

Figure 28.- Continued.

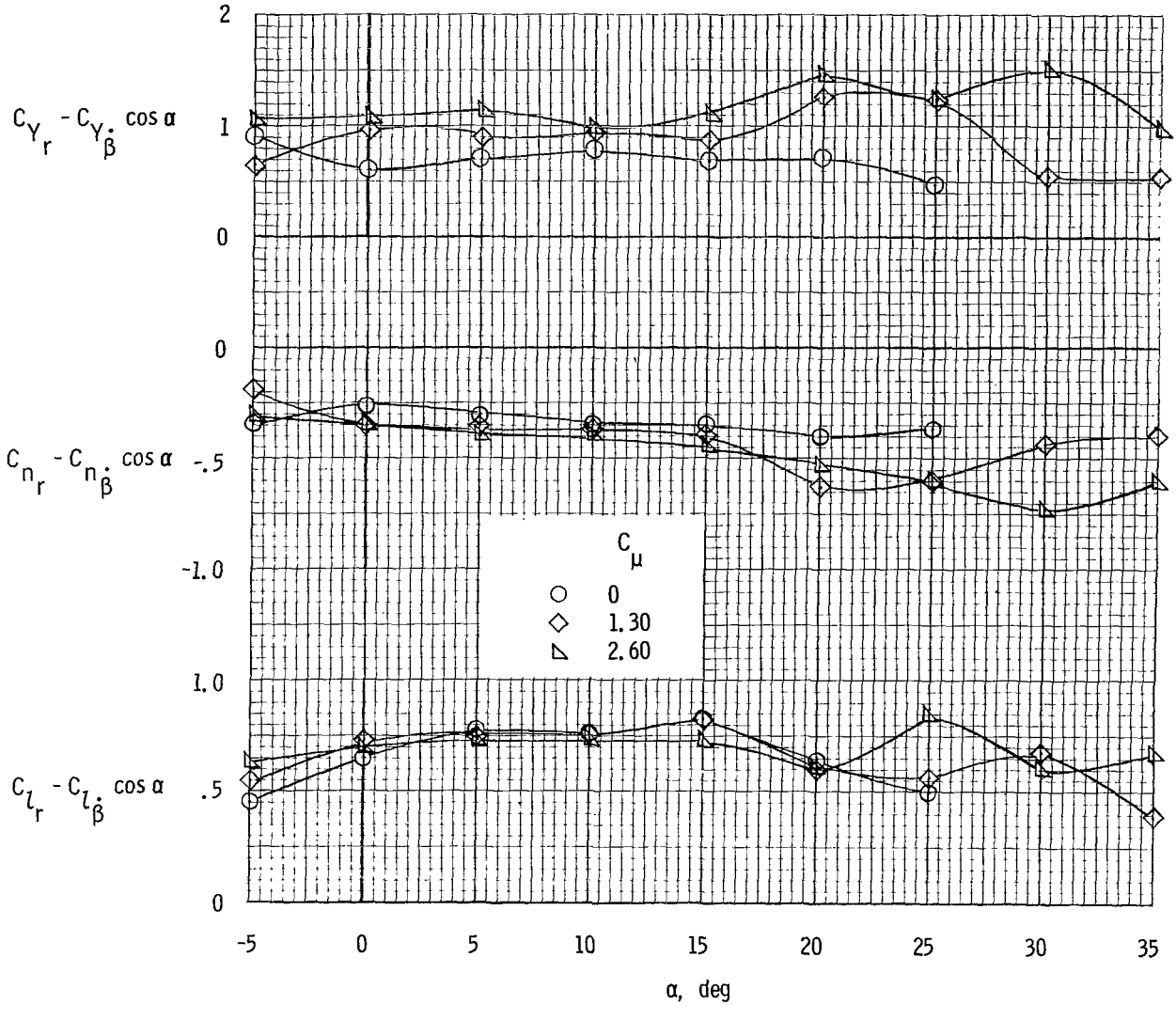

(c) Left outboard engine not operating; $C_{\mu,le} = 0$; $\delta_{f,L} = 70^o$, $\delta_{f,R} = 40^o$.

Figure 28.- Continued.

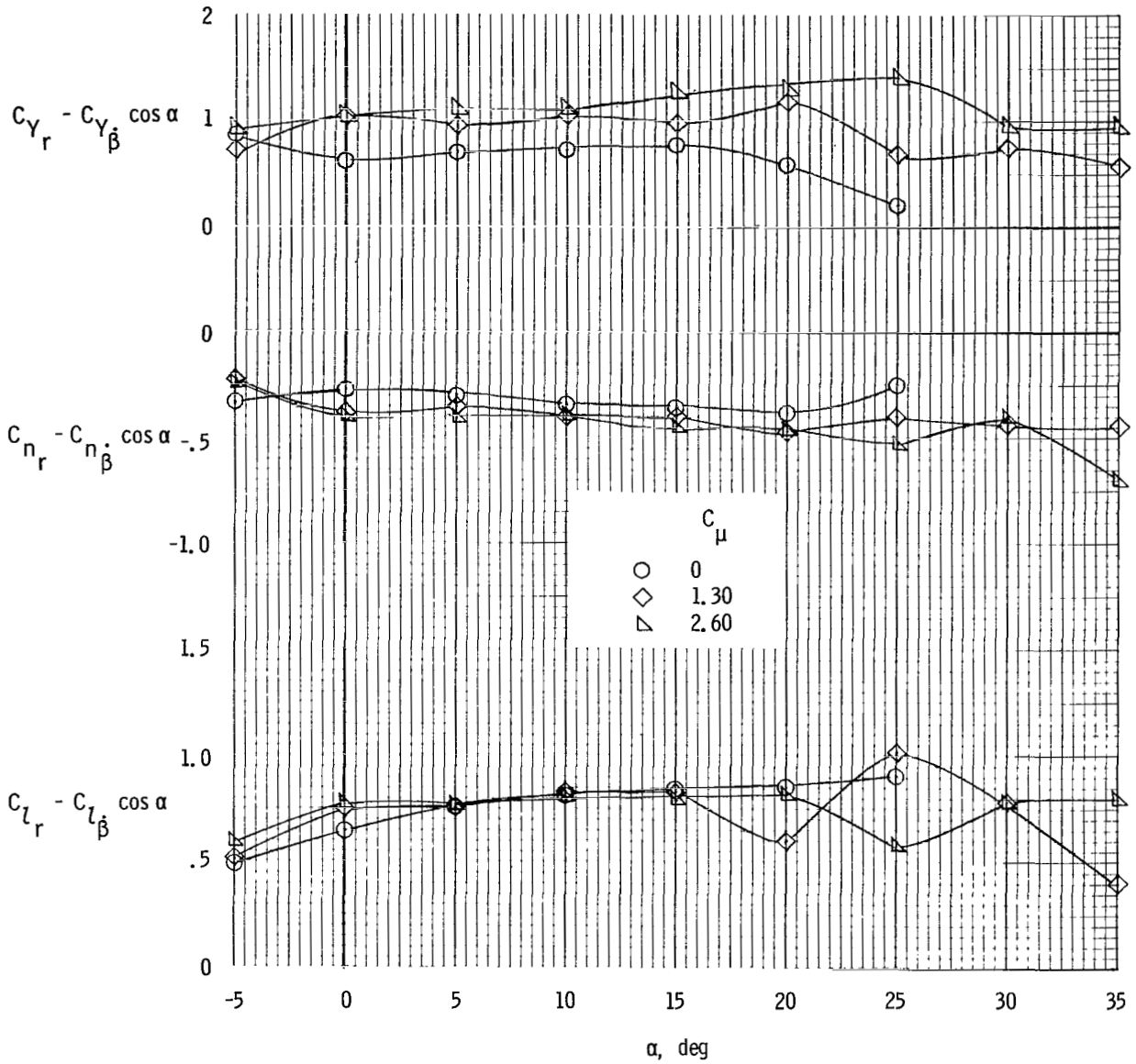

(d) Left outboard engine not operating; $C_{\mu,le} = 0.024$; $\delta_{f,L} = 70^o$, $\delta_{f,R} = 40^o$.

Figure 28.- Concluded.

"The aeronautical and space activities of the United States shall be conducted so as to contribute . . . to the expansion of human knowledge of phenomena in the atmosphere and space. The Administration shall provide for the widest practicable and appropriate dissemination of information concerning its activities and the results thereof."

—NATIONAL AERONAUTICS AND SPACE ACT OF 1958

NASA SCIENTIFIC AND TECHNICAL PUBLICATIONS

TECHNICAL REPORTS: Scientific and technical information considered important, complete, and a lasting contribution to existing knowledge.

TECHNICAL NOTES: Information less broad in scope but nevertheless of importance as a contribution to existing knowledge.

TECHNICAL MEMORANDUMS: Information receiving limited distribution because of preliminary data, security classification, or other reasons.

CONTRACTOR REPORTS: Scientific and technical information generated under a NASA contract or grant and considered an important contribution to existing knowledge.

TECHNICAL TRANSLATIONS: Information published in a foreign language considered to merit NASA distribution in English.

SPECIAL PUBLICATIONS: Information derived from or of value to NASA activities. Publications include conference proceedings, monographs, data compilations, handbooks, sourcebooks, and special bibliographies.

TECHNOLOGY UTILIZATION PUBLICATIONS: Information on technology used by NASA that may be of particular interest in commercial and other non-aerospace applications. Publications include Tech Briefs, Technology Utilization Reports and Technology Surveys.

Details on the availability of these publications may be obtained from:

SCIENTIFIC AND TECHNICAL INFORMATION OFFICE

NATIONAL AERONAUTICS AND SPACE ADMINISTRATION

Washington, D.C. 20546